An Interpretation of Observed Atmospheric Variations of CO_2 and CH_4

James Barlow

THE UNIVERSITY
of EDINBURGH

Thesis submitted in fulfilment of
the requirements for the degree of
Doctor of Philosophy
to the
University of Edinburgh — 2014

Declaration

I declare that this thesis has been composed solely by myself and that it has not been submitted, either in whole or in part, in any previous application for a degree. Except where otherwise acknowledged, the work presented is entirely my own.

James Barlow
September 2014

Abstract

The overarching theme of my thesis is understanding observed variations of northern hemisphere atmospheric carbon dioxide (CO_2) and methane (CH_4) concentrations. I focus my analysis on high-latitude observations of these gases, as there are large stores of carbon in boreal vegetation and tundra which are vulnerable to rapid warming in the Arctic. My thesis is split into two parts. First, I use the wavelet transform to spectrally decompose observed multi-decadal timeseries for CO_2 and CH_4. I perform a series of numerical experiments based on synthetic data in order to characterise the errors associated with the analysis. For CO_2, I analyse the phase and amplitude of the detrended seasonal cycle of CO_2 to infer changes about carbon uptake by northern vegetation. I do not find a long-term change in the length of the carbon uptake period despite significant changes in the spring and autumn phase. I do find an increase in the rate of peak uptake which coincides with the observed increase in seasonal amplitude. These results suggest that the carbon uptake period of boreal vegetation has become more intense but has not changed in length, which provides evidence for an increase in net uptake of CO_2 in the high latitudes. For CH_4, I test the hypothesis that an increase in Arctic wetland emissions could result in a decrease in the seasonal amplitude of CH_4 in the high latitudes. This hypothesis is based on the fact that the seasonal minima of CH_4 roughly coincides with the peak of high latitude wetland CH_4 emissions. I find that the CH_4 seasonal amplitude has significantly decreased at a number of high-latitude sites. However I also find that atmospheric transport appears to drive much of the variability in high-latitude CH_4 and that transport could also be responsible for the observed changes in amplitude. I show that an increase in wetland emissions is likely to have a more pronounced effect on the high-latitude CH_4 seasonal cycle in the future. In the second section of my thesis, I describe a series of experiments in collaboration with the UK Astronomy Technology Centre, in which I characterise a new instrument technology for satellite applications to observe changes in CO_2 from low-Earth orbit. The proof of concept experiments were performed with a bench top hyperspectral imager. I show that the instrument is able to capture clean spectra at the wavelengths required for CO_2 with low levels of scattered light between spectra.

Acknowledgements

There are several people to whom I owe my utmost gratitude and acknowledgement; as without them I would not have been able to complete this project. First and foremost, I'd like to thank my supervisor Paul Palmer. Paul, you have pushed me to be the best I can be, and have shown continuous support, patience, and understanding. I am sincerely grateful for your motivation, skill and guidance throughout this project. Thank you.

I have had the pleasure of meeting and working with many skilled scientists in the course of this project, who are paving the way in their fields, and from whom I have learnt so much. Thank you to Martyn Wells and David Lee from the UK Astronomy Technology Centre for their assistance with my work on the PERSIST project. My thanks goes to Lori Bruhwiler for her enthusiasm and continuous support for my work during my time at the National Oceanic and Atmospheric Administration in Boulder, Colorado. Alongside Pieter Tans and Ed Dlugokencky, you truly provided me with a wonderful opportunity and a hospitable welcome, and have continued to extend this support following my return to Edinburgh.

I'd like to thank my advisor Annemarie Fraser, and the other members of the Tropospheric Chemistry and Earth Observation Modelling Group in Edinburgh. I'd like to thank Hartmut Böesch for hosting me for a week at the University of Leicester and helping me to use their Radiative Transfer Model.

My mum and dad and two sisters have always provided endless support in everything that I do, thank you so much. I got there in the end! I'd like to thank my partner, Nadine, for her encouragement and helping me to get through the final stages of writing my PhD thesis. I'd also like to thank fellow students and good friends, Douglas Finch, Emma Knowland, Kathleen Allen, Robyn Butler, Abbie Clare, Emily Woollen, Richard Nair, Antony Bloom, and Silvia Caldararu. I could not have asked for a better group of office pals.

Finally, I am very grateful to the Centre for Earth Observation Instrumentation and the National Environmental Research Council (NERC) for funding my studentship, number NE/1528818/1.

Contents

List of Tables

List of Figures

List of Symbols

Quantities

permil - Parts per thousand
ppm - Parts per million
ppb - Parts per billion
Pg - Petagram (10^{15} grams)
Tg - Teragram (10^{12} grams)

Organisations

ATC - Astronomy Technology Centre
CEOI - Centre for Earth Observation Instrumentation
CGASN - Cooperative Global Air Sampling Network
CU - University of Colorado, Boulder
ECMWF - European Centre for Medium range Weather Forecasting
ESA - European Space Agency
ESRL - Earth System Research Laboratory
FAO - Food and Agriculture Organization of the United Nations
GMAO - NASA Global Monitoring and Assimilation Office
GMD - Global Monitoring Division
IMAU - Institute for Marine and Atmospheric Research Utrecht
INSTAAR - Institute of Arctic and Alpine Research
IPCC - Intergovernmental Panel on Climate Change
JAXA - Japanese Aerospace Exploration Agency
JRC - Joint Research Centre, Italy
KNMI - Royal Netherlands Meteorological Institute
NASA - National Aeronautic and Space Administration
NOAA - National Oceanic and Atmospheric Administration
NERC - National Environmental Research Council
NRCS - Natural Resources Conservation Service
SIO - Scripps Institute of Oceanography
UNESCO - United Nations Educational, Scientific and Cultural Organisation
USDA - United States Department of Agriculture
WMO - World Meteorological Institute

Atmospheric Constituents

O_2 - Oxygen
CO_2 - Carbon Dioxide
XCO_2 - Carbon Dioxide Column
$\delta^{13}C$ - Isotope ratio (applicable to CO_2 or CH_4)
CH_4 - Methane
OH - Hydroxyl Radical

Observation Sites

ALT - Alert, Nunavut (65.51°W, 82.45°N)
BRW - Barrow, Alaska (156.61°W, 71.32°N)
CBA - Cold Bay, Alaska (162.72°W, 55.21°N)
ICE - Iceland (20.29°W, 63.40°N)
MLO - Mauna Loa, Hawaii (155.57°W, 19.53°N)
SHM - Shemya Island, Alaska (174.13°E, 52.71°N)
STM - Ocean Station M, Norway (02.00°E, 66.00°N)
ZEP - Ny-Alesund, Svalbard (11.89°E, 78.91°N)

TransCom Regions

NABor - Boreal North America
NATmp - Temperate North America
ASBor - Boreal Asia
ASTmp - Temperate Asia
Europe - Europe

Acronyms

ACTM - Atmospheric Chemistry Transport Model
AF - Airborne Fraction
AIRS - Atmospheric Infrared Sounder
ASCENDS - Active Sensing of CO_2 Emissions over Nights, Days and Seasons
CUP - Carbon Uptake Period calculated from CO_2 concentration
CUP_Δ - CUP calculated from CO_2 first time derivative
$\Delta_t CO_2$ - First time derivative of CO_2 concentration
DIAL - DIfferential Absorption Lidar
DJF - December, January, February (northern hemisphere winter)
DZCP - Downward Zero Crossing Point
EDGAR - Emissions Database for Global Atmospheric Research
ENSO - El Niño Southern Oscillation
EO - Earth Observation
FF - Fossil Fuel

FTS - Fourier Transform Spectrometer
FWHM - Full Width Half Maximum
GEOS - Goddard Earth Observing System
GFED - Global Fire Emissions Database
GMST - Global Mean Surface Temperature
GOSAT - Greenhouse Gases Observing Satellite
GPP - Gross Primary Productivity
GR - Growth Rate
GWP - Global Warming Potential
IFS - Integral Field Spectrometer
IFU - Integral Field Unit
JJA - June, July, August (northern hemisphere summer)
LUC - Land Use Change
MAM - March, April, May (northern hemisphere spring)
MCS - Monte Carlo Simulation
MERRA - Modern Era-Retrospective Analysis for Research and Applications
MBL - Marine Boundary Layer
NAS - North Air Sector
NBP - Net Biome Productivity
NEP - Net Ecosystem Production
NH - Northern Hemisphere
OCO - Orbiting Carbon Observatory
OSSE - Observing System Simulation Experiment
PERSIST - Prototype Earth obseRving System using Image Slicer Technology
PNH - Polar Northern Hemisphere
PR - Peak Release
PU - Peak Uptake
R_a - Autotrophic Respiration
RF - Radiative Forcing
R_h - Heterotrophic Respiration
RMA - Reduced Major Axis Regression
RMSE - Root Mean Square Error
SAS - South Air Sector
SCIAMACHY - SCanning Imaging Absorption SpectroMeter for Atmospheric CartograpHY
SH - Southern Hemisphere
SND - South-North Difference
SON - September, October, November (northern hemisphere autumn)
SWIR - Short Wave Infra-Red
SZA - Solar Zenith Angle
TANSO - Thermal And Near infrared Sensor for carbon Observation
TGS - Thermal Growing Season
TGS_{BEG} - TGS beginning

TGS$_{END}$ - TGS end
TGS$_{LEN}$ - TGS length
TIR - Thermal Infra-Red
UZCP - Upward Zero Crossing Point
WL - Wavelet
ZCP - Zero Crossing Point

Chapter 1

Introduction

It was nearly 200 years ago in the 1820s when Joseph Fourier, a French mathematician and physicist, discovered that Earth should be much colder than it is given its proximity to the Sun. One of the explanations he provided, was that the atmosphere was acting as an insulator, trapping some of the heat from incoming solar radiation. Today, his theory is widely recognised as the first proposal of the "greenhouse effect".

Roughly 35 years later, the physicist John Tyndall developed this theory, explaining the additional heat in the Earth's atmosphere in terms of the capacities of various greenhouse gases to absorb radiant heat or infrared radiation. He not only determined the relative radiative forcing of different greenhouse gases, but also suggested that slight changes in the atmospheric concentration of these gases, whether man made or natural, could bring about variations in the Earth's climate. In 1896, Svante Arrhenius was the first scientist to attempt to calculate how changing levels of atmospheric carbon dioxide (CO_2) could alter global surface temperatures via the greenhouse effect. His focus was on CO_2, as although water vapour (H_2O) was far more abundant in the atmosphere, it fluctuated daily.

In contrast, the level of CO_2 was considered to change over geological timescales due to volcanic emissions and uptake by the oceans, and act as a “control knob” for the amount of atmospheric water vapour. Although Arrhenius was primarily interested in finding the necessary decrease of CO_2 to bring about an ice age, he also recognised that CO_2 in the atmosphere could increase as a result of burning coal. He calculated that a doubling of atmospheric CO_2 would bring about roughly 5-6°C of global warming, although it was thought at the time that it would take several thousand years to burn this quantity of coal. This numerical calculation was done by pencil over several laborious months, and as such left out many of the complexities of Earth's climate system.

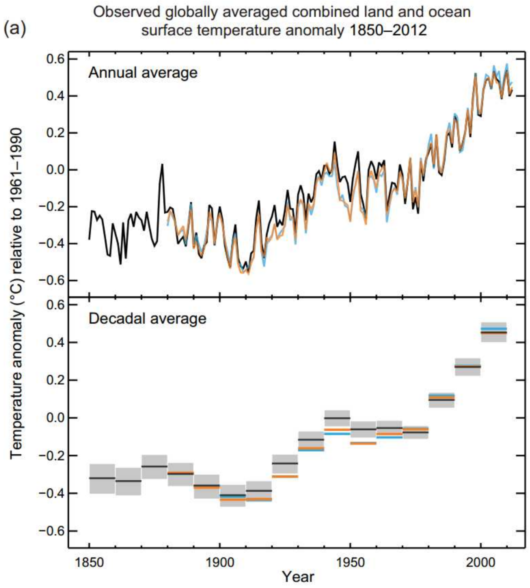

Figure 1.1: Observed global mean (combined land and ocean) surface temperature time series from 1850 to 2012 from three seperate datasets (above) and decadal mean temperatures (black) with uncertainty values for the dataset (shaded grey) (below) (Stocker *et al.*, 2013).

Well over a century has now passed since the initial studies of the relationship between CO_2 and the climate, and the Earth's human population has grown from just over one billion people in 1820 to more than 7 billion people in the present day. Since the industrial revolution began in 1760, industrial output and the burning of fossil fuels have grown to match the demands of the increasing global population, with the associated rate of anthropogenic emissions of CO_2 far exceeding anything imagined by Arrhenius. Atmospheric CO_2 has risen from a relatively stable pre-industrial concentration of ~280 ppm to over 400 ppm in the present day. Atmospheric CH_4, the second most important greenhouse gas has risen from 700 ppb to over 1600 ppb over the same time period. These levels are far higher than anything inferred from proxy data in the past 800,000 years. Alongside these increases in greenhouse gases, we have also observed an increase in the global mean surface temperature (GMST) of ~0.85°C between 1880-2012 (see Figure 1.1) and much larger regional changes in temperature, particularly in the Arctic. Gaining a better understanding of future greenhouse gas concentrations is essential to reduce uncertainties on projections of climate change.

Charles Keeling set up the first continuous measurement of atmospheric CO_2 using infrared instrumentation in 1958, which after a few years showed a rise in CO_2 as a result of human activity. He selected his first site, based at Mauna Loa in Hawaii, as it was situated far away from strong local sources such that measurements were representative of the global atmospheric concentration. As well as the year-to-year rise in CO_2, Keeling's measurements also showed the presence of a seasonal cycle representing the imprint of the natural carbon cycle. This seasonal cycle was later associated with terrestrial vegetation, which removes CO_2 from the atmosphere during its growing phase, and releases CO_2 during the autumn and winter months. Indeed, the natural carbon cycle consists of many sources and sinks of carbon which control the amount of anthropogenic emissions that remain in the atmosphere. The rate of CO_2 accumulation in the atmosphere is smaller than expected, and it is hypothesised that this is due to changes in the sinks of the natural carbon cycle. The increase of CH_4 in the atmosphere has not been as persistent as the rise in CO_2, as the atmospheric growth rate reached near equilibrium before increasing again following 2007. The reason for this remains highly uncertain. We can move forward and reduce these uncertainties by improving the methods that we use to monitor the carbon cycle.

While the presence of CO_2 in our atmosphere is essential for life on Earth, the recent and rapid rate of increase in its atmospheric concentration as a result of human activity is unsustainable and could lead to disastrous consequences. There are currently huge efforts in the scientific community in many different disciplines to improve observations of the climate and our atmosphere, each aiming to to provide a better understanding of the many underlying drivers and mechanisms of the climate and how they interact. It is hoped that this information will help to influence policy decisions linked to managing the causes and mitigating the effects of anthropogenic climate change. Two examples of mitigation are the reduction of anthropogenic CO_2 emissions by converting from fossil fuel to renewable energy sources, and the maintenance of ecosystems that act as a net sink of CO_2.

In this thesis, I attempt to address some of the uncertainties in the carbon cycle by analysing time series of CO_2 and CH_4 surface mole fraction data. In particular I am interested in high-latitude observations, as there are large stores of carbon in boreal vegetation and tundra which are vulnerable to rapid warming in the Arctic. In Chapter 2 I focus on observations of the CO_2 mole fraction. I use a wavelet transform to separate the long-term trend and the seasonal cycle in CO_2 time series. The long-term trend provides information about the growth rates of CO_2 in the atmosphere, while the seasonal cycle is used to look at changes in the carbon uptake period. I associate changes in these metrics with changes in carbon uptake in high-latitude boreal vegetation. In Chapter 3, I focus on observations of the CH_4 mole fraction. I use hourly in situ measurements of CH_4 from the Alaska North Slope to estimate summertime CH_4 anomalies which are associated with changes in local wetland emissions. I analyse high-latitude CH_4 flask measurements to look for evidence of large-scale increases in Arctic wetland emissions, and use an atmospheric transport model to interpret the results. A key focus throughout these studies is the detectability of trends associated with high-latitude surface fluxes when using observations from the current observing network. In Chapter 4, I present a proof of concept study of a novel satellite instrument for observing CO_2 and CH_4 from space. Finally, in Chapter 5, I summarise the results of my work, and suggest potential avenues to explore in future studies.

In this first chapter I will describe the basic relationship between the greenhouse gases CO_2 and CH_4 and the climate, and why further study of these areas and particularly the carbon cycle is essential for maintaining a sustainable future for Earth's inhabitants. I will also look at recent changes in atmospheric concentrations of CO_2 and CH_4 and the ways in which we measure changes in the carbon cycle. Finally I will present an outline of my thesis.

1.1 Greenhouse Gases and Climate Change

1.1.1 Planetary Radiation Balance

The basic science behind the effect of greenhouse gases on surface temperature is relatively simple, and starts with the planetary radiation balance. The amount of incoming short wave radiation received by the Earth is determined by the solar constant, S ($= 1370\text{Wm}^{-2}$) given Earth's distance from the Sun, minus the proportion of radiation that is reflected into space, dependent on the planetary albedo, α_p, multiplied by the area of the Earth facing the Sun (πr^2). We assume that the emission from the Earth is equal to a blackbody flux at temperature, T_e. As a black body emitter, the energy is radiated isotropically (independent of direction) and thus the amount of outgoing longwave radiation is the equivalent blackbody flux (σT_e^4) multiplied by the surface area of the Earth ($4\pi r^2$). We can therefore write the following to express Earth's radiative energy balance under conditions of radiative equilibrium:

$$S\left(1-\alpha_p\right)\pi r^2 = \sigma T_e^4 4\pi r^2, \tag{1.1}$$

where r is the radius of Earth, σ is the Stefan-Boltzmann constant and $S\pi r^2$ is the amount of solar radiation intercepted by Earth given conditions of no reflection ($\alpha_p = 0$). Rearranging equation 1.1 for the black body temperature of Earth:

$$T_e = \left(\frac{S\left(1-\alpha_p\right)}{4\sigma}\right)^{1/4}. \tag{1.2}$$

The temperature T_e is simply the blackbody emission temperature required to balance the incoming solar radiation. Assuming an albedo of $\alpha_p = 0.30$ (Goode *et al.*, 2001), we obtain from equation 1.2 a value of $T_e = 255$K (or -18°C). Note that this temperature is significantly lower than the global mean surface temperature that is actually observed on Earth, $T_0 = 288$K (15°C). The observation of this difference led to speculation and theory on the greenhouse effect and is indeed a result of emission of thermal radiation from atmospheric gases and water vapour.

1.1.2 The Greenhouse Effect

When shortwave radiation from the Sun penetrates to the surface of the planet, it is absorbed at the Earth's surface and re-radiated outwards as energy of a longer wavelength as a result of the cooler temperature of Earth. Constituents of the atmosphere, such as water vapour, carbon dioxide and methane, which are relatively transparent to inbound shortwave radiation, absorb and trap a proportion of the outgoing longwave radiation, which leads to a warming of the Earth's surface and lower atmosphere. The amount of outgoing radiation absorbed by individual gases depends on their concentration and spectral properties.

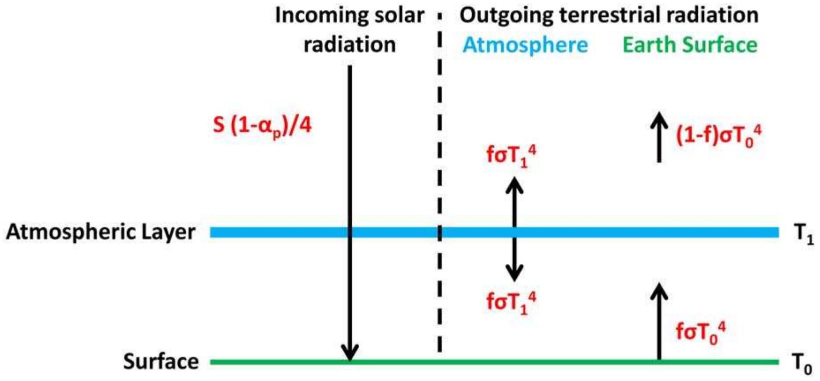

Figure 1.2: Schematic showing the different components of the planetary radiation balance, inclusive of an atmospheric layer which simulates the greenhouse effect. f is the fraction of outgoing radiation absorbed by the atmospheric layer, σ is the Stefan-Boltzmann constant, T_0 is Earth's surface temperature and S is the solar constant.

The simple model in the previous section can be extended to include the greenhouse effect and is shown by the schematic in Figure 1.2. We begin by introducing an atmosphere and assume that it is an isothermal layer (constant temperature) at some arbitrary distance above Earth's surface. This layer is transparent to incoming shortwave radiation from the sun, but absorbs a fraction, f, of outgoing terrestrial radiation due to the presence of greenhouse gases. The temperature of the Earth's surface is T_0, while the temperature of the atmosphere is T_1. The amount of outgoing radiation absorbed by the atmosphere is equal to $f\sigma T_0^4$, while the radiation emitted by each surface (top and bottom) of the atmosphere is $f\sigma T_1^4$. The energy balance of the new system, inclusive of an atmospheric layer, can be written:

$$\frac{S\left(1-\alpha_p\right)}{4}=\left(1-f\right)\sigma T_0^4+f\sigma T_1^4 \tag{1.3}$$

where the left and right hand sides of the equation are incoming and outgoing radiation respectively. We write a separate energy balance equation for the atmospheric layer, taking into account our assumption of isotropy:

$$f\sigma T_0^4=2f\sigma T_1^4 \tag{1.4}$$

Inserting equation 1.4 into equation 1.3 and solving for T_0 yields:

$$T_0=\left[\frac{S\left(1-\alpha_p\right)}{4\sigma\left(1-\frac{f}{2}\right)}\right]^{\frac{1}{4}} \tag{1.5}$$

Using this equation with $T_0 = 288\mathrm{K}$, $\alpha_p = 0.30$ (Goode *et al.*, 2001), $S = 1370\mathrm{Wm}^{-2}$ and $\sigma = 5.67{\times}10^{-8}\mathrm{Wm}^{-1}\mathrm{K}^{-4}$, indicates that the atmosphere must be absorbing approximately $f = 0.77$, or 77% of Earth's outgoing radiation. From the simple model shown in equation 1.5, it is easy to see than an increase in greenhouse gases, and the associated increase in the absorption efficiency, f, would result in an increase in T_0, the surface temperature.

1.1.3 Radiative Forcing

Radiative forcing (RF) is a common measure to describe the effect of an individual greenhouse gas on Earth's temperature. RF is defined as the difference between the radiant energy received by Earth, and the energy that is radiated back into space. For example, an increase in a greenhouse gas such as carbon dioxide would introduce a positive forcing effect, and subsequently warm the system. In climate science, radiative forcing is typically used as a measure of how important a factor is in terms of global warming potential, described in the following section. In practice it is also used to estimate changes in the equilibrium surface temperature ($\Delta \mathrm{T}_s$) resulting from some change in the radiative forcing. The following equation describes this relationship:

$$\Delta T_s = \lambda \Delta F \tag{1.6}$$

where λ is known as the climate sensitivity and ΔF is the radiative forcing.

1.1.4 Global Warming Potential

The Global Warming Potential (GWP) goes a step further than RF, and provides information about the contribution of a greenhouse gas to temperature change (or added energy to the climate system) over a given timeframe, dependent on the temporal evolution of its radiative forcing and atmospheric concentration, and given as an index relative to a reference gas, in this case CO_2. The IPCC define it as “the time-integrated RF due to a pulse emission of a given atmospheric constituent, relative to a pulse emission of CO_2 of equal mass” (Stocker *et al.*, 2013). It is dependent on both the radiative properties of the gas and its lifetime within the atmosphere.

$$GWP(x) = \frac{\int_0^H a_x \cdot [x(t)]dt}{\int_0^H a_r \cdot [r(t)]dt} \tag{1.7}$$

The GWP given by equation 1.7, is calculated by integrating the RF due to a pulse of a particular emission over a time horizon (given by H), typically 20, 100 or 500 years. In equation 1.7 a_x is the radiative forcing due to an increase in the atmospheric abundance of a given gas, while [x(t)] is the time-dependent decay of the substance determined by its atmospheric lifetime between t=0 and the time horizon t=H. In the denominator, a_r and [r(t)] are the equivalent for the reference gas, CO_2.

Gas	**Lifetime**	**Concentration**		**dC/dt**	**Rad. Forc.**	**GWP**	
	(yrs)	**1750**	**2011**	(2005-2011)	**(Wm^{-2})**	20-year	100-year
CO_2	Variable	278 ppm	390 ppm	1.94 ppm/yr	1.82±0.19	1	1
CH_4	12.4	722 ppb	1803 ppb	4.77 ppb/yr	0.48±0.05	84	28

Table 1.1: This table contains information about the two greenhouse gases which are the top contributors to radiative forcing. The lifetimes are the perturbation lifetimes used to estimate global warming potential. The pre-industrial concentrations are calculated from air extracted from ice cores. The 2011 concentrations and annual mean growth rates between 2005-2011 are taken from the National Oceanic and Atmospheric Administration Global Greenhouse Gas Reference Network. Uncertainties are 90% confidence intervals. Climate-carbon feedbacks are included for CO_2 GWP, but not for the other gases. Data table is reproduced from Stocker *et al.* (2013).

Values of RF and GWP for the three single largest contributors are given by Table 1.1. This table excludes water vapour, which while being the strongest greenhouse gas (Kiehl and Trenberth, 1997), is a function of temperature and responds to climate as a feedback (Held and Soden, 2000; Soden *et al.*, 2005). The table instead shows the three strongest greenhouse gases which are directly added to the atmosphere by human activity. It can be seen that CH_4 is 84 times more absorptive than CO_2 over 20 years. This means that one kg of CH_4,

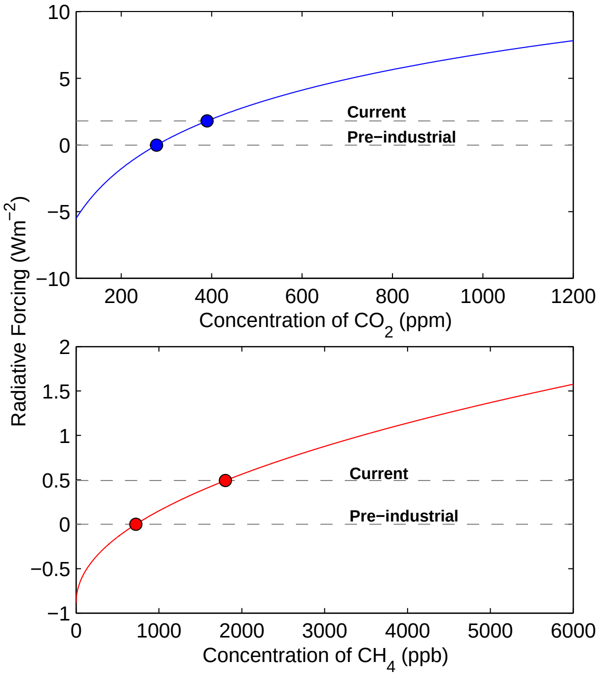

Figure 1.3: Radiative forcing of CO_2 and CH_4 as a function of their atmospheric concentration *relative* to pre-industrial levels (1780 values in Figure 1.1). It is reproduced from the simplified equations and updated constants from Myhre *et al.* (1998). Note the difference in scales for both axes.

produces 84 times the radiative forcing of a kilogram of CO_2 over 20 years. After 100 years the GWP of CH_4 is significantly reduced to 28 due to its relatively short lifetime of 12.4 years. Although CH_4 is the most absorptive of these gases, CO_2 is currently the most problematic greenhouse gas due to its sheer quantity in the atmosphere, present in 1000× higher atmospheric concentration. Despite this, CH_4 is of particular concern, primarily due to the abundant stores in high-latitude regions where there are large quantities stored in frozen soils which are vulnerable to increases in temperature. In addition to this, as the abundance of CO_2 and CH_4 increases in the atmosphere, their contribution to radiative forcing does not increase linearly. For example, as the ppm concentration of CO_2 increases, the additional radiative forcing it adds to the atmosphere becomes less and less - this is because the thermal absorption frequency of CO_2 becomes saturated. Other gases, such as CH_4 have thermal absorption frequencies that are far from saturated, and thus increases in their concentration could have far more significance for climate change in the future. This non-linear relationship is highlighted in Figure 1.3.

1.1.5 Recent Changes in a Historical Context

In order to understand recent increases in greenhouse gases, it is useful to have an understanding of how they have varied historically and what the primary drivers of these changes were. Time series of historical CO_2 and CH_4 concentrations have been determined by measuring the composition of trapped air in ice cores deep in the Antarctic ice sheet (Lüthi *et al.*, 2008; Loulergue *et al.*, 2008; MacFarling Meure *et al.*, 2006), while records of isotopic deuterium from ice cores are used as a proxy for temperature change (Jouzel *et al.*, 2007). Ice cores that are taken from progressively deeper ice typically contain older air bubbles. However deeper ice is also significantly more compressed, resulting in a coarser time step as we look further into the past. Despite this, these methods have allowed time series that extend as far back as 800,000 years.

Figure 1.4 shows time series of temperature, CO_2 and CH_4 over the past 800 thousand years. It shows cyclic behaviour and that in the past 800 thousand years the atmospheric concentration of CO_2 has varied regularly from about 180 ppm during deep glaciations to 280 ppm during interglacial periods (Lüthi *et al.*, 2008). The temporal pattern of CH_4 variations are very similar, ranging from 350 ppb to 800 ppb in glacial and interglacial periods respectively (Loulergue *et al.*, 2008). Finally temperature variations over this time period show the same cyclic behaviour with a range in the temperature anomaly of 15°C. This highlights the magnitude of climatic variability before the influence of human activity, but also

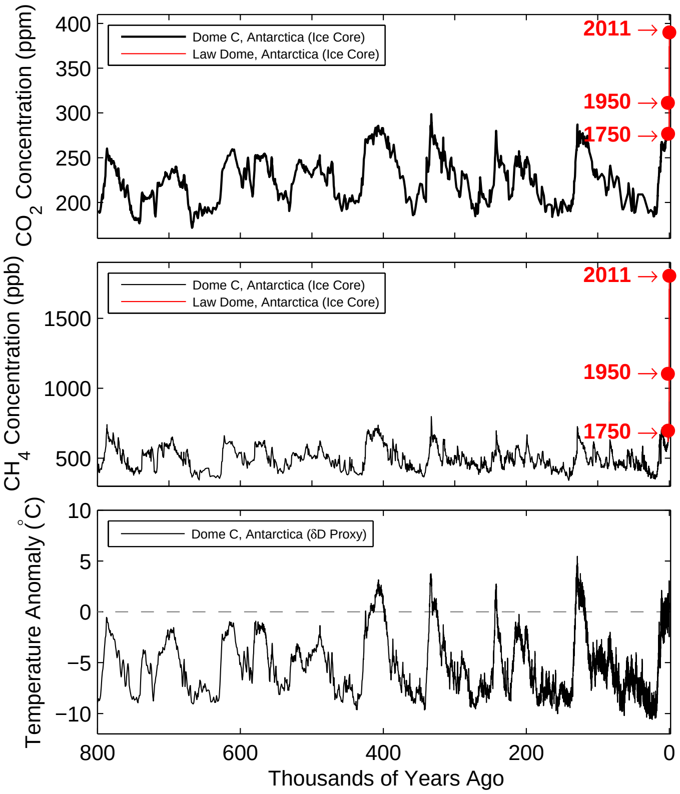

Figure 1.4: Black lines are 800 thousand year historical records of CO_2 (Lüthi *et al.*, 2008), CH_4 (Loulergue *et al.*, 2008) and temperature (Jouzel *et al.*, 2007), red lines show records over the past 2000 years for CO_2 and CH_4 (MacFarling Meure *et al.*, 2006). Red markers indicate values of CO_2 and CH_4 concentrations in 1750, 1950 and the 2011 values taken from table 1.1.

the relationship between temperature and greenhouse gases. The climate is affected by a large number of factors, such as solar variability, volcanic activity and natural changes in atmospheric composition. However the huge shifts in climate between glacial and interglacial periods seen in Figure 1.4 are thought to be triggered by periodic changes in the Earth's orbit, termed Milankovitch cycles, which alter the distance of the Earth from the Sun and subsequently the total solar irradiance on Earth's surface. However, these orbital shifts alone are not considered sufficient to drive the huge changes in temperature and atmospheric composition observed in the historical time series. Instead, a number of feedback processes are involved. These processes are described by Shakun *et al.* (2012) who studied 80 proxy records (for example proxies from tree ring data) to build up a picture of global temperature changes as opposed to Antarctica ice core records alone which are only representative of local variations in temperature. It is suggested from this analysis that the shift in orbit resulting from the Milankovich cycles trigger the initial warming, which results in huge quantities of fresh water from melting Arctic ice being mixed into the ocean. This disrupts the Atlantic meridional overturning circulation, which causes a warming of the Southern Ocean, which in turn releases significant quantities of CO_2 into the atmosphere. The majority of the rise in temperature subsequently *follows* the rise in atmospheric CO_2.

The natural variations of CO_2 and CH_4 observed over the past 800 thousand years puts into context the recent changes in their atmospheric concentration, also shown in Figure 1.4, which have risen well above any concentration observed in "recent" geological history. The more recent historical record over the past 2000 years (MacFarling Meure *et al.*, 2006) also shows that CO_2 sources and sinks were in relative equilibrium (resulting in a negligible growth rate) until approximately 200 years ago. In fact, the rapid rise in CO_2 and CH_4 coincides with the onset of the industrial revolution, and there is significant additional evidence other than looking at historical human activities that this rise is caused by anthropogenic emissions (see Figure 1.5)

1.1.6 Recent Human Influence

There are numerous lines of evidence to show that the recent rise in atmospheric CO_2 is caused by human activity. The combustion of fossil fuel for example, uses O_2 from the atmosphere to produce CO_2 molecules. O_2 has been observed to decrease along with the increase in CO_2 (Keeling and Shertz, 1992; Sirignano *et al.*, 2010). If increasing CO_2 was due to natural sources it would most likely be from the ocean. However the pH of the oceans is decreasing as a result of increased absorption of CO_2 by the ocean resulting in ocean acidification (Feely *et al.*, 2009). Analysis of carbon isotopes has also been used to attribute recent increases in CO_2 with anthropogenic emissions. There are three primary carbon isotopes, where ^{12}C is the most common, ^{13}C makes up around 1% and ^{14}C accounts for just 1 in 1 trillion carbon atoms. CO_2 produced from fossil fuel combustion or forest fires have a different isotopic composition from CO_2 in the atmosphere. This is because plants prefer to take up lighter carbon isotopes (^{12}C over ^{13}C). Fossil fuels, which are formed from ancient plants, have approximately the same $^{13}C/^{12}C$ ratio as current plants. As the isotope ratio of plants and fossil fuels is smaller than that of the atmosphere, the combustion of those materials results in a decrease of the atmospheric isotopic ratio. ^{14}C is known as radiocarbon due to its radioactivity. The radiocarbon in fossil fuels extracted from the ground has mostly decayed. The addition of carbon to the atmosphere from fossil fuel combustion therefore causes a decrease in $\Delta^{14}C$ as most other CO_2 in the atmosphere is from relatively young sources. Although there are other sources of CO_2 that alter $\Delta^{14}C$ in the atmosphere, they have a much smaller effect than that of fossil fuel CO_2, making it a useful measurement to determine the fraction of anthropogenic CO_2 in the atmosphere (Levin and Hesshaimer, 2000).

There is also strong evidence to suggest that recent changes in warming are due to the rapid increases in greenhouse gas concentrations, with the largest contribution from atmospheric CO_2. In fact, recent results published in the AR5 IPCC report (Stocker *et al.*, 2013) indicate that there is now more certainty than ever that human activity is responsible for the recent rise in greenhouse gases, and that this increase is responsible for contemporary climate warming. The report states

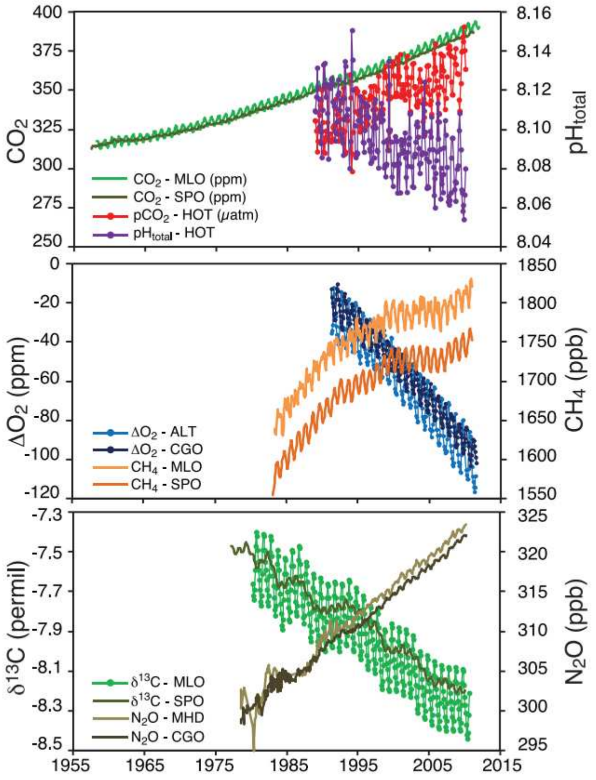

Figure 1.5: Atmospheric concentrations of CO_2, O_2, $^{13}C/^{12}C$ stable isotope ratio in CO_2, CH_4, N_2O and ocean surface observations of CO_2 partial pressure (pCO_2) and pH recorded at 4 representative sites in the northern and southern hemispheres (Stocker *et al.*, 2013).

that "it is *extremely likely* ($p<0.01$) that human activities caused more than half of the observed increase in global average surface temperatures from 1951 to 2010". Figure 1.6 shows recent observed temperature changes and modelled temperature variations driven by natural and greenhouse gas forcing and natural forcing only. In recent years, the observed anomalies of GMST relative to the 1880-1919 mean lie well outside the range of GMST anomalies from model simulations which do not include greenhouse gas forcing. In contrast, including greenhouse gas forcing in model simulations produces an ensemble mean trend in model GMST that closely follows observed GMST. Although this is not evidence in itself of human-induced warming, it shows that recent natural variations in climate forcing cannot account for the observed warming, while greenhouse gas forcing can.

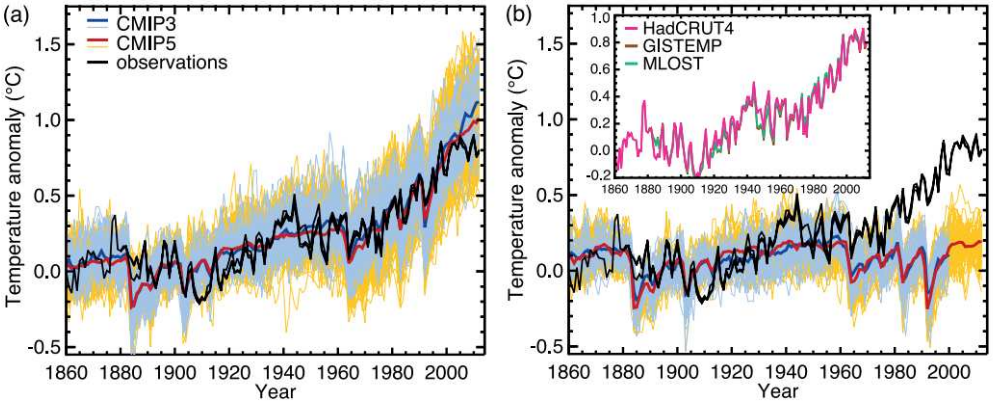

Figure 1.6: Three observational estimates of global mean surface temperature (black lines) from the Hadley Centre/Climatic Research Unit gridded surface temperature (HadCRUT4), Goddard Institute for Space Studies Surface Temperature Analysis (GISTEMP) and Merged Land-Ocean Surface Temperature Analysis (MLOST), compared with model simulations (CMIP3 Model - blue lines, CMIP5 Model - yellow lines) with (a) anthropogenic and natural forcings and (b) natural forcings only (Stocker *et al.*, 2013).

So far, we have shown a simple model which highlights the ability of greenhouse gases present in the atmosphere to cause warming at the Earth's surface. We have seen that by sheer quantity, CO_2 currently adds the most radiative forcing to the Earth's surface and that this is followed by CH_4. We have seen that historical records of CO_2 and CH_4 are closely coupled with temperature, and that a number of processes, namely Milankovich cycles in conjunction with internal feedback processes have caused the Earth to cycle in and out of glacial and interglacial periods over hundreds of thousands of years. We have shown that recent increases in CO_2 and CH_4 are unprecedented in recent geological history and that these increases are a result of human activity. Finally, we have shown that the recent increases in greenhouse gases are very likely to be strongly linked with recently observed increases in global temperature. All of this information is useful, but a number of important questions remain:

- How is the climate going to change in the near and distant future?
- What consequences will these climatic changes have on human civilisation?
- How can we mitigate climate change?

Our ability to answer these questions strongly depends on our ability to determine the amount of carbon in the atmosphere, and we must therefore improve our knowledge of the carbon cycle.

1.2 The Global Carbon Cycle

The global carbon cycle is a huge and complex system which determines the amount of carbon stored within Earth's atmosphere. It is made up of carbon reservoirs - uniquely defined pools of carbon, and fluxes - which define the rates of movement of carbon from one reservoir to another. Carbon in Earth's atmosphere primarily exists in the form of CO_2 and CH_4. The largest fluxes of CO_2 are cycled between the atmosphere, ocean and terrestrial biosphere. There are also geological stores with which carbon is exchanged over very long time scales (Archer *et al.*, 2009), although the extraction and burning of fossil fuels is an exception. CH_4 has many sources that are unique from CO_2 but only has one primary sink. The primary sink of CH_4 is its destruction by the chemical reaction with the hydroxyl radical (OH) in the atmosphere. There are several other minor sinks of CH_4 which are described briefly below. An imbalance between the source and sink terms can result in a positive or negative net flux to the atmosphere which leads to an increase or decrease in their atmospheric abundance respectively. At present, there still remains great uncertainty in the location and distribution of many of the sources and sinks of CO_2 and CH_4 and how they vary from year to year, and this prevents us from being able to make long term predictions of the natural carbon cycle response to changing atmospheric composition and climate change. It is vital that we improve our understanding and reduce these uncertainties in order to predict future changes in climate.

1.2.1 CO_2 Sources and Sinks

The CO_2 budget is divided up into the following major reservoirs, where Table 1.2 gives an indication of the approximate size of each reservoir:

- Atmosphere
- Terrestrial Biosphere - this includes soils and plants
- Oceans - including sediments, and dissolved inorganic carbon and living/non-living marine biota in the surface and deep layer
- Lithosphere - this is mostly inert carbon, although it can be released through metamorphosis of carbonate rocks, volcanic eruptions and by the burning of extracted fossil fuels.

CO_2 is regularly exchanged between the atmosphere, ocean, and terrestrial biosphere, over a range of spatial and temporal scales. The terrestrial biosphere stores organic carbon in the form of land-based organisms, soils and micro-organisms such as bacteria and fungi. On a global scale, plants and soils are the largest carbon stores of the terrestrial biosphere, containing approximately 560 PgC and 1500 PgC respectively. The net carbon flux between a biome-scale

Earth's Carbon Reservoirs	
Reservoir	**Size (PgC)**
Atmosphere	750
Terrestrial Biosphere	
Forests	560
Soils	1500
Ocean	
Surface Ocean	900
Deep Ocean	37100
Ocean Sediments	1750
Lithosphere	
Carbonates	100×10^6
Fossil Fuels	4000

Table 1.2: Size of various carbon reservoirs (PgC) (Global Carbon Project).

terrestrial ecosystem and the atmosphere is known as Net Biome Productivity (NBP):

$$NBP = NEP - L_d \tag{1.8}$$

where NEP is the Net Ecosystem Production and L_d is carbon which is lost through major disturbances such as forest fires, deforestation and land use change. The NEP is the net carbon flux resulting from the balance between photosynthesis and respiration:

$$NEP = GPP - R_h - R_a \tag{1.9}$$

where GPP is the Gross Primary Productivity, R_h is heterotrophic respiration, R_a is autotrophic respiration. The GPP is a measure of the amount of atmospheric carbon used by plants to form new plant tissues in the process of photosynthesis. R_h is the metabolism of organic matter by bacteria, fungi and animals, while R_a is the metabolism of organic matter by plants, both of which result in loss of carbon to the atmosphere. To a large extent, these processes are dependent on biotic factors which means that in many cases they follow a diurnal and seasonal cycle.

This dependence on biotic factors also means that they are sensitive to changes in climate and atmospheric composition resulting in changes to the balance between photosynthesis and respiration. Carbon from dead plant matter is typically incorporated into soils where it can be stored for years, decades or centuries before it is broken down by soil microbes are re-released into the atmosphere. Forest fires are a further mechanism by which plant and soil carbon can be rapidly released into the atmosphere.

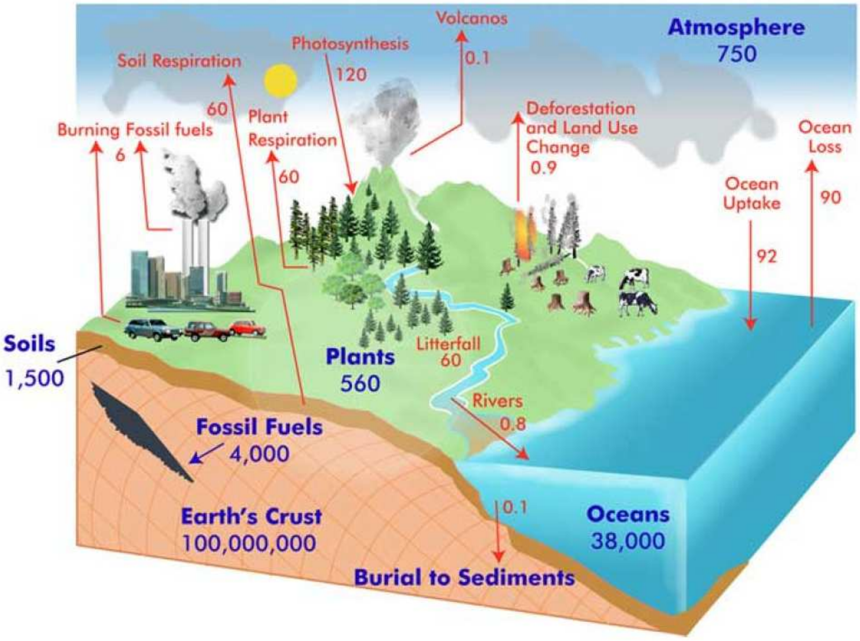

Figure 1.7: Simplified diagram of the global carbon cycle. Pool sizes are given in blue, whereas fluxes between the pools are given in red. Units are petagrams (Pg) of carbon and Pg per year (Pg/yr) respectively. Source: Global Carbon Project - www.globe.gov/projects/carbon.

Oceans contain the largest amount of actively cycled carbon (~38000 PgC), however the majority of this, ~37100 PgC, is stored as dissolved inorganic carbon in the deep layer of the ocean. The surface layer contains ~900 PgC, most of which is dissolved organic carbon that is exchanged rapidly with the atmosphere. The oceans currently act as a net sink for CO_2, and this is driven by two primary mechanisms: the solubility pump and the biological pump (Raven and Falkowski, 1999).

The *biological pump* is the smallest of the two processes and begins in the euphotic zone, where there is sufficient sunlight for phytoplankton to photosynthesize. The phytoplankton convert dissolved inorganic carbon into organic biomass, either soft, or hard tissues. In the case of hard tissues, calcium (Ca) and dissolved carbonic acid and bicarbonate are combined to form a calcium carbonate ($CaCO_3$) shell. Eventually the phytoplankton die, and a proportion of them ($\sim$25%) sink to the ocean floor. A further proportion of the dead phytoplankton are sequestered into the surface sediment on the ocean floor where they can remain for thousands of years. The *solubility pump* occurs as the result of two processes in the ocean:

- The solubility of CO_2 is inversely related to sea water temperature, where cooler temperatures are favourable for solubility.
- The thermohaline circulation is driven by deep water formation in the high latitudes where waters are lower in temperature.

Subsequently, CO_2 taken up by the oceans in the high latitudes is pumped into the ocean interior as dissolved inorganic carbon by the thermohaline circulation. The water which carries this dissolved inorganic carbon can later upwell in equatorial regions, where due to the reduced solubility of the warmer waters results in outgassing of CO_2 into the atmosphere.

The carbon budget of CO_2 can be summarised by the following equation:

$$\frac{dM}{dt} = F_{anthro} - (F_{land} + F_{ocean}) \tag{1.10}$$

where F_{land} is the net land flux, F_{ocean} is the net ocean flux, and the human-driven, or anthropogenic flux, F_{anthro}, is equal to:

$$F_{anthro} = F_{fossil} + F_{LUC} \tag{1.11}$$

a combination of fossil fuel emissions (F_{fossil}) and changes in carbon flux resulting from changes in land use (F_{LUC}) such as deforestation (Le Quéré *et al.*, 2014).

1.2.2 CH_4 Sources and Sinks

Although they share some common sources, the sources and sinks of CH_4 are different to CO_2. The primary sink of atmospheric CH_4, accounting for 90% of the global CH_4 sink, is oxidation by hydroxyl radicals (OH) in the upper troposphere. OH, which is produced photochemically, has a concentration which varies seasonally in conjunction with changes in UV. The reaction leading to the chemical destruction of CH_4 by OH occurs as follows:

$$OH + CH_4 \rightarrow H_2O + CH_3 \tag{1.12}$$

Its rate of destruction, $d[CH_4]/dt = -k_3(T)[OH][CH_4]$ depends on temperature, the abundance of OH, and the CH_4 burden. This reaction is the first in a chain of reactions eventually leading to the creation of CO and CO_2. The remaining CH_4 sinks are uptake of CH_4 by soils, destruction by reaction with Cl and O in the stratosphere, and reaction of CH_4 with Cl in the marine boundary layer. These sinks make up the final 10% of the global CH_4 sink.

There are a large number of CH_4 sources, both natural and anthropogenic. Sources of CH_4 can be grouped into three categories: biogenic, thermogenic and pyrogenic. Biogenic sources contain CH_4 generating microbes or methanogens, an example of which are anaerobic environments such as natural wetlands or rice paddies. Thermogenic CH_4 is formed over millions of years through geological processes into fossil fuels. Exploitation of fossil fuels subsequently results in its release into the atmosphere, although it can also vent through naturally occurring features. Pyrogenic CH_4 is produced by incomplete combustion of biomass and soil carbon. This occurs during natural fires (wild fires) as well as from the burning of biofuels and fossil fuels. Each of these sources has a unique isotopic signature which can help to differentiate between them.

The atmospheric methane reservoir was approximately 2007±50 $TgCH_4$ in the pre-industrial era and has grown by 2960±60 $TgCH_4$ from 1750-2009 (Kirschke, 2013). Kirschke (2013) provide estimates of mean annual CH_4 emissions throughout 2000-2009. The largest single source of CH_4 are wetlands, including bogs, swamps, marshes and peat lands to name a few, with a mean emission of $\sim$217 $TgCH_4/yr$. The majority of wetlands are located in tropical and subtropical humid regions. The high-latitude northern hemisphere is home to vast areas of wetlands accounting for approximately 44% of total wetland areas (OECD, 1996) and where permafrost limits emissions of CH_4. Warm temperatures during the high-latitude summer increases soil thaw, resulting in a summertime peak emission of wetland CH_4. Although wetlands only cover 6-7% of the Earth's surface (OECD, 1996), they account for a disproportionate share of the terrestrial carbon pool. The majority of wetland carbon is stored in northern boreal and sub-arctic regions in peat land soils. At present, low and mid-latitude wetlands represent a larger annual source of CH_4 to the atmosphere, but as CH_4 emission rates from high-latitude wetlands peak during periods of soil thaw, carbon stores in these regions are particularly vulnerable to rapid warming in the Arctic. Geological sources of CH_4 are ~54 $TgCH_4$/yr and emissions from CH_4 hydrates are currently very low (~6 $TgCH_4$/yr). The largest anthropogenic sources are from fossil fuels (~96 $TgCH_4$/yr), ruminants (~90 $TgCH_4$/yr), emissions from landfills and waste (~75 $TgCH_4$/yr) and rice paddies (~36 $TgCH_4$/yr). Destruction of CH_4 by tropospheric OH typically lies within 450-620 $TgCH_4$/yr (Kirschke, 2013).

1.2.3 Observing the Carbon Cycle

A large range of instruments and techniques have been developed to observe and improve our understanding of the carbon cycle. For example measurement campaigns of the soil-atmosphere CO_2 flux have taken place in hundreds of locations. However flux measurement sites are often short term resulting in temporal discontinuities and the fluxes they measure are representative of relatively small spatial scales. This type of measurement is particularly useful for understanding the underlying processes which determine carbon fluxes and their response to environmental variables. Flux measurements are typically up scaled using a process-based model. This approach to estimating large-scale carbon fluxes is known as a “bottom-up” estimate.

The “top down” approach is used to make estimates of carbon fluxes from concentrations of CO_2 and CH_4 in the atmosphere. As this is not a direct measurement of the carbon flux, the flux estimates are inferred indirectly. Up until recently, continental-scale flux estimates have typically been estimated by the assimilation of ground-based measurements of atmospheric CO_2 into an atmospheric chemistry transport model (ACTM). Such a model uses the existing best estimate (prior) surface emission fluxes with assimilated meteorological fields to simulate spatial and temporal variations in atmospheric concentrations of trace gases. By assimilating the most recent CO_2 or CH_4 measurements, the prior surface fluxes are then adjusted to find the best match between the model and input data, termed the posterior flux.

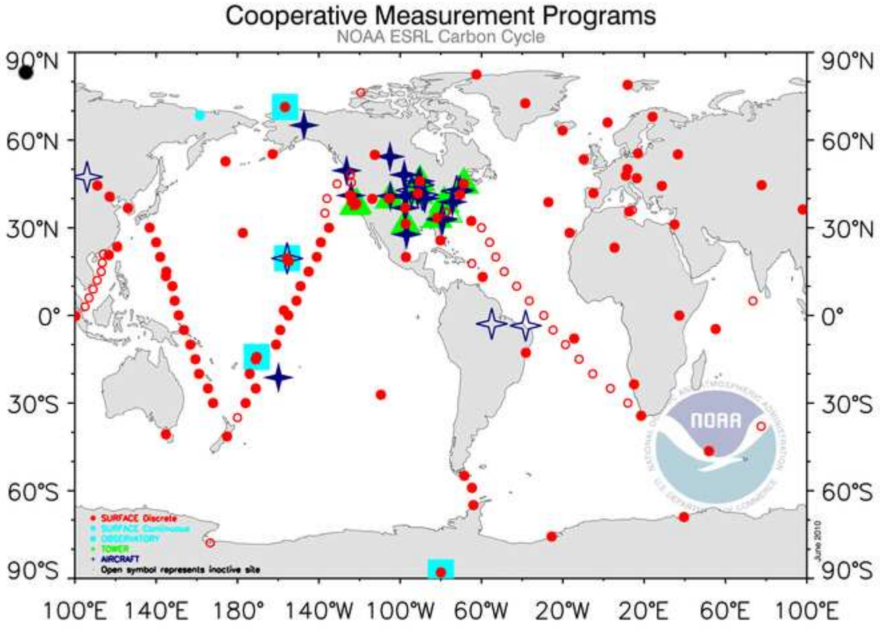

Figure 1.8: Global map of NOAA/ESRL GMD greenhouse gas monitoring sites showing discrete flask sites (red circles), observatories that collect semi-continuous measurements (blue squares), tower data (green triangle) and locations where aircraft campaigns have collected data (blue stars). Source: http://www.esrl.noaa.gov/gmd/ccgg/

Since 1958 when Keeling set up his CO_2 instrument at Mauna Loa, the global surface measurement network of CO_2 has grown, with more sites around the world measuring an increasing number of greenhouse gases. The largest measurement network is the Cooperative Global Air Sampling Network (CGASN), which is run by the National Ocean and Atmospheric Administration (NOAA)/Earth System Research Laboratory (ESRL) Global Monitoring Division (GMD) and has many sites located around the world. Figure 1.8 shows the extent of the NOAA/ESRL greenhouse gas monitoring network. Although one of the first direct observations of atmospheric CH_4 was made in 1978 Blake *et al.* (1982), the NOAA/ESRL network began to monitor CH_4 continuously in 1983 (Dlugokencky *et al.*, 1983-2013). CO_2 and CH_4 are now measured at many surface monitoring sites at a range of temporal resolutions by a number of different research communities. The advantage of such observations is that they can be representative of large scale surface fluxes if the location of the measurement is chosen carefully. However, such observations are affected by surface fluxes from a wide range of sources which have been transported from all of the world. ACTMs are required to interpret the transport component of the data. Although ground based observations are very precise, their global spatial distribution is sparse and unevenly distributed for surface flux estimates at smaller spatial scales. From Figure 1.8, it can be seen that boreal and tropical regions have a relatively low number of sampling sites, where these areas are some of the largest contributors to terrestrial carbon fluxes. Aircraft flight campaigns also provide useful observations of CO_2 in that they can provide vertical profiles of CO_2, however they have a limited range and are only available on a campaign basis. This limits their spatial coverage and the time period over which measurements can be taken. The low number of sampling sites in boreal and tropical regions means that they are poorly represented in flux inversions, and high uncertainties persist in the carbon flux estimates.

Space-based observations of the atmosphere represent a possible solution to the relatively sparse surface network. They have the potential to provide high resolution observations with frequent global coverage including observations over regions that are, at present, poorly characterised by ground-based measurements. It has been shown that space-borne observations of CO_2 have the potential to be very useful for constraining CO_2 surface fluxes at regional scales in comparison to using the existing ground-based network alone (Rayner and O'Brien, 2001).

There are a number of operational instruments that take measurements of XCO_2 and XCH_4 from space, where XCO_2 is the column-averaged dry air mole fraction of CO_2. These column concentrations are not direct measurements but are inferred by measuring spectra of sunlight reflected from the Earth's surface. The reflected electromagnetic radiation is absorbed by CO_2 and CH_4 in the atmosphere at very specific wavelengths. A space-borne spectrometer is able to measure the spectra which contain this information in the form of absorption lines, from which the amount of CO_2 and CH_4 in the atmospheric column can be retrieved using a radiative transfer model. CO_2 instruments typically measure reflected radiation in the thermal and short-wave infrared wavelengths (TIR and SWIR respectively) as CO_2 absorption is strong at these wavelengths. Measurements of SWIR radiation provides the key advantage of being particularly sensitive of CO_2 concentrations near to the surface where this is more useful for estimating surface fluxes (Olsen and Randerson, 2004).

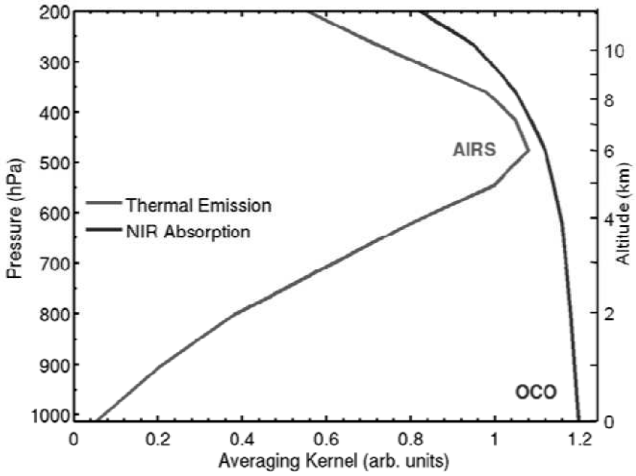

Figure 1.9: Representative averaging kernels for XCO_2 soundings using the near infrared (analogous to SWIR) CO_2 absorption band from OCO and the TIR CO_2 absorption band from AIRS(Crisp *et al.*, 2004).

The Atmospheric Infrared Sounder (AIRS) on-board the National Aeronautics and Space Administration (NASA) Aqua satellite, launched in 2002, was the first instrument from which global maps of atmospheric CO_2 in the cloud-free upper troposphere could be derived from measurements of TIR. TIR soundings are less sensitive to near-surface CO_2 due to the small surface-atmosphere temperature contrast. The CO_2 concentrations in the upper troposhere tend to be relatively zonal due to atmospheric mixing and provide limited information about surface fluxes (Chevallier *et al.*, 2005). For this reason, most subsequent missions, for example the NASA Orbiting Carbon Observatory (OCO) (Crisp *et al.*, 2004) have opted for soundings of XCO_2 in the SWIR part of the spectrum. Figure 1.9 shows the averaging kernels for AIRS and OCO respectively, where the averaging kernels represent the vertical weighting of the XCO_2 retrieval depending on which CO_2 absorption band is used. In addition to AIRS, The European Space Agency's (ESA) SCanning Imaging Absorption SpectroMeter for Atmospheric CartograpHY (SCIAMACHY) was also launched in 2002 aboard Envisat, which was the next satellite from which retrievals were made of XCO_2, this time from measurements of SWIR. Although the SCIAMACHY instrument was highly sensitive to surface CO_2, it was not initially optimised for observing the necessary absorption bands for XCO_2 retrievals, resulting in systematic XCO_2 retrieval errors and subsequent limitations on flux estimation Frankenberg *et al.* (2011). The Japanese Aerospace Exploration Agency (JAXA) launched the Greenhouse gases Observing SATellite (GOSAT) in 2009, carrying the Thermal And Near infrared Sensor for carbon Observation (TANSO), the first instrument dedicated to observing XCO_2 and XCH_4 concentrations from space. NASA's OCO was due to be launched in the same year as GOSAT, but an unfortunate failing of the launch model resulted in the loss of the satellite. A replacement for OCO was launched earlier this year. Space-borne sensor technology and algorithms for retrieving XCO_2 and XCH_4 are being developed rapidly, and these measurements are likely to provide substantially better constraints on the carbon budget when used in conjunction with ground-based data and flux inversion methods. Although there are many planned missions and many emerging mission concepts, there is a requirement for new designs which are lighter, more compact and with the ability to measure atmospheric XCO_2 and XCH_4 concentrations with greater accuracy.

1.2.4 CO_2 and CH_4 since 1958

Carbon Dioxide

Figure 1.10 shows estimates of anthropogenic CO_2 emissions and how they are partitioned into different carbon reservoirs from the Global Carbon Project 2013 (Le Quéré *et al.*, 2014). The top panel shows the increase in emissions from fossil fuel combustion and cement production, as well as those resulting from changes in land–use. The bottom panel shows estimates of how these emissions have been distributed among the different carbon reservoirs with time. It can be seen that each of the three reservoirs, the land, the oceans, and the atmosphere have gradually increased in size as emissions of CO_2 have increased. Note that there is far more interannual variability following 1958 due to the additional information from continuous CO_2 measurements, but also that the land sink shows significantly more variability than the oceans. The land carbon sink appears to be particularly sensitive to climate variability and it has been shown that large scale climate phenomena such as El Ninõ–Southern Oscillation (ENSO) explains much of this variability (Jones *et al.*, 2001). Cox *et al.* (2013) highlights the existence of an emerging linear relationship between the interannual variation in the CO_2 growth rate and tropical temperature anomalies which are highly correlated with ENSO.

By removing anthropogenic emissions from the annual growth rate in the atmospheric concentration of CO_2, it has been calculated that approximately 43% of anthropogenic emissions of CO_2 remain in the atmosphere annually, while the

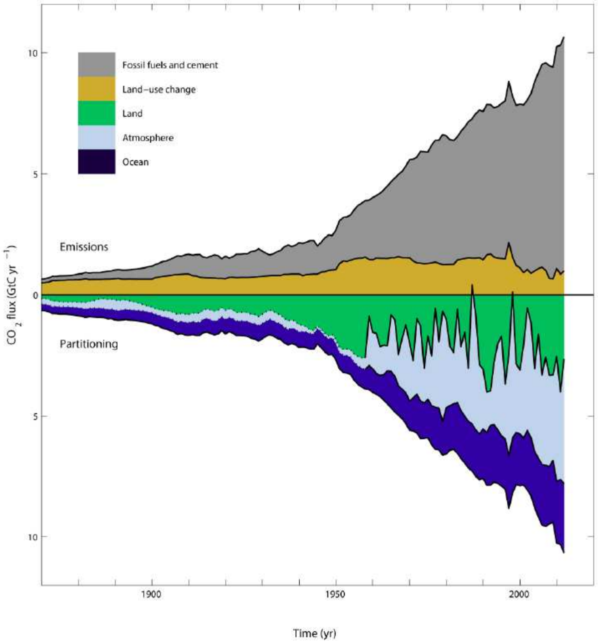

Figure 1.10: Sources of CO_2 (land use change and combined fossil fuel combustion and cement production) and estimates of how they are partitioned into different carbon reservoirs: the terrestrial biosphere, oceans and atmosphere (Le Quéré *et al.*, 2014). The interannual variability in the land flux is significantly larger than any of the other carbon fluxes.

rest is absorbed by the natural carbon cycle (Stocker *et al.*, 2013). This fraction is known as the airborne fraction (AF). As shown in Figure 1.10, the oceans and terrestrial biosphere are considered responsible for this "missing sink". While the rate of anthropogenic CO_2 emissions has been steadily rising, long term change in the AF appears to be small. This is in agreement with many studies suggesting that the natural carbon cycle has been taking up progressively more CO_2 (e.g. (Canadel *et al.*, 2007)) with uptake approximately doubling since 1960 (Ballantyne *et al.*, 2012). The biosphere and oceans have, in effect, provided a free service to us so far by reducing the proportion of our CO_2 emissions that remain in the atmosphere, and in turn preventing additional greenhouse warming. Changes in the efficiency of these sinks could have a large impact on the rate of climate change (Raupach, 2011).

It has been debated whether there has been a trend in the AF, with Le Quéré *et al.* (2009) estimating a 90% probability of a significant AF increase of 3±2% per decade over the period of continuous CO_2 measurements at Mauna Loa. Le Quéré *et al.* (2009) outline several possibilities to explain this increase: (1) a greater rate of increase in CO_2 emissions than strengthening of uptake from carbon sinks (2) a reduction in the rate at which carbon sinks are becoming more efficient due to the limits of CO_2 fertilisation and/or the oceans becoming saturated with CO_2 (3) a response of the carbon sinks to climate variability or change (4) some sink processes that have not yet been considered. A different study, by Knorr (2009), did not find evidence to support a statistically significant increase in the AF based on the available data and accuracy. This result however differed depending on whether the AF, which contains substantial interannual variability, was filtered to reduce the influence of interannual climate variability and volcanic eruptions. Knorr (2009) found trends in the AF of 0.2±0.17 and 1.2±0.9%/yr per decade over the same time period for the unfiltered and filtered cases respectively. Frölicher *et al.* (2013) found that previous studies such as Le Quéré *et al.* (2009) underestimate decadal-scale effects of large volcanic eruptions in calculations of AF trends, and also found a near-zero trend in their analysis.

It has been speculated that the AF alone is insufficient to make firm conclusions about a slowdown of land biosphere or ocean uptake of anthropogenic carbon - for example, Gloor *et al.* (2010) pointed out that changes in ocean and land sinks are not equivalent to changes in the airborne fraction. A more recent study has used an observable quantity that reflects sink properties more directly than the AF, k_s, the combined land–ocean CO_2 sink flux per unit of excess atmospheric CO_2 above pre–industrial levels (Raupach *et al.*, 2014). They find that this quantity has decreased by ∼33% throughout 1959-2012 re–enforcing the idea that CO_2 sinks have increased at a slower rate than the increase in excess CO_2 and where 20% of the trend is estimated to be a response to climate change. If this gap continues to widen, CO_2 will begin to accumulate more rapidly in the atmosphere. Indeed, this is not totally unexpected, as model simulations have estimated a decline in the future uptake of CO_2 by the ocean and terrestrial biosphere (Friedlingstein *et al.*, 2006). For example, while higher levels of CO_2 can enhance plant photosynthesis and water use efficiency, it can also increase plant and soil respiration rates. It is not currently known whether the terrestrial biosphere will remain a net sink of CO_2 or become a net source in the next century (Friedlingstein *et al.*, 2006).

It is likely that terrestrial ecosystems will respond differently to climate change and increased atmospheric CO_2 concentrations according to their geographical region. This will largely result from differences in plant physiology and different regional changes in climate in the tropics and mid to high latitudes. For example, boreal ecosystems which primarily lie >50°N between temperate forest and tundra, are being exposed to particularly rapid warming as a result of polar amplification of climate change, in addition to the higher levels of atmospheric CO_2. Our ability to monitor these ecosystems and their exchange rates of carbon with the atmosphere on regional scales as well as improving the methods by which we analyse existing data is now key.

Methane

Discrete global measurements of CH_4 began in 1983 as part of the NOAA/ESRL monitoring network (Dlugokencky *et al.*, 1983-2013). In the past 30 years, the atmospheric observations have shown a substantial rise in CH_4 of ~200 ppb. The atmospheric growth rate of CH_4 was ~12 ppb/yr between 1980–1992, but slowed to ~9 ppb/yr in the following decade, before reaching a relatively stable state in the early 2000s (Dlugokencky *et al.*, 1998). This “stagnation” period occured between 1999-2006, but in 2007 the concentration of CH_4 began to rise again at ~6 ppb/yr (Rigby *et al.*, 2008; Dlugokencky *et al.*, 2009).

The reasons for the observed changes in the growth rate are still not fully understood. On decadal timescales, estimates of natural CH_4 emissions from "bottom-up" inventories (based on process based models) appear to be ~20% larger than those estimated using "top down" methods (those that use atmospheric concentration measurements) (Kirschke, 2013). These inconsistencies indicate that estimates of regional emissions of natural sources are still not robust. Meanwhile, industrial emissions appear to be underestimated. Miller *et al.* (2013), for example, finds that anthropogenic emissions of CH_4 from fossil fuel extraction and processing is 4.9±2.6 times higher than those estimated in the Emission Database for Global Atmospheric Research (EDGAR), considered to be the most comprehensive global methane inventory.

A number of studies have found that the immediate rise in the CH_4 concentration following 2007 was partly due to a surge in natural wetland emissions in the Arctic (Dlugokencky *et al.*, 2011) and the tropics (Bousquet *et al.*, 2011) in 2008-2009 and 2010-2011 respectively (Bloom *et al.*, 2010). The increases in the Arctic were associated with abnormally high temperatures in 2007. Indeed, there are vast stores of CH_4 in the Arctic that are vulnerable to rapid increases in temperature. In addition to anthropogenic emissions from gas wells and pipelines, there are large areas of permafrost and methane hydrate trapped beneath offshore permafrost. Although the permafrost carbon pool accumulates slowly and can be preserved for millions of years when frozen, it is highly decomposable and can be released quickly when thawed (Zimov *et al.*, 2006b). When permafrost thaws, methanogenisis can occur in exposed soils on the land, and bubbles of previously trapped CH_4 can rise up to the ocean surface from the sea bed, subsequently being released into the atmosphere. Large emissions from decaying methane hydrates have already been observed from the East Siberian Arctic Shelf (Shakhova *et al.*, 2010, 2013), although these have not been detected in NOAA/ESRL atmospheric measurements and they are likely to remain limited in the next 100 years (Biastoch *et al.*, 2011). Permafrost sediments on the land have already begun to thaw (Romanovsky *et al.*, 2001), and many are questioning the fate of permafrost carbon (Zimov *et al.*, 2006a). Isotope measurements from surface and aircraft campaigns have also been used to highlight Arctic wetlands as a major source in the Summer, and gas leaks from industry in the Winter (Fisher *et al.*, 2011). A long term trend in Arctic emissions from permafrost has not yet been observed and despite the potentially large effect on future climate projections, few model simulations currently account for the potential of large Arctic CH_4 emissions.

1.3 Thesis Outline

My thesis has two primary objectives:

- Assess recent changes in the seasonality of the carbon cycle in high-latitude regions of the northern hemisphere for CO_2 and CH_4.
- Explore a novel satellite instrument concept for observing CO_2 from space.

As ever, I have an ultimate objective, which in this case is to improve our current understanding of recent changes in the global carbon cycle. The focus of my thesis is on recent changes in CO_2 fluxes from boreal vegetation, and high-latitude wetland sources of CH_4 in response to rapidly increasing Arctic and sub-Arctic temperatures.

In Chapter 2, I characterise the errors associated with analysing variability and trends of the CO_2 seasonal cycle when it is detrended using the wavelet transform. I analyse the phase and amplitude of the CO_2 seasonal cycle using a range of metrics, some of which have not previously been used. The phase of the seasonal cycle refers to changes in the timing of the net carbon uptake period, while the amplitude represents changes in overall carbon exchange. I compare the results with high-latitude temperature metrics and co-located observations of the CO_2 isotope ratio, $\delta^{13}C$.

In Chapter 3, I analyse ground-based in-situ and flask measurements of high-latitude CH_4 concentrations to look for evidence of changing CH_4 emissions from boreal and Arctic wetlands. In-situ observations at Barrow, Alaska, provide information about summertime CH_4 anomalies that are associated with wetland emissions from the North Slope of Alaska. These anomalies show the relative timing of wetland emissions with respect to the broad scale CH_4 seasonal cycle at high latitudes. It is hypothesised that increases in wetland emissions could result in a decrease in the seasonal amplitude of CH_4 at high-latitude sites. I analyse flask measurements of CH_4 for changes in amplitude, and use output from an atmospheric transport model to investigate whether this could be linked with a change in wetland emissions.

In Chapter 4, I present a novel instrument concept, developed by staff at the UK Astronomy Technology Centre, for observing atmospheric columns of CO_2 from space. I present the results from the prototype laboratory experiments which I carried out on the instrument and characterise the ability of the instrument to measure the three spectra necessary for XCO_2 retrievals on the same detector. This study is limited to theoretical design and proof of concept of the instrument.

In Chapter 5 I summarise the results and suggest future directions for this work.

Chapter 2

Evidence of large-scale changes in CO_2 uptake at high northern latitudes

2.1 Introduction

Observed variability of atmospheric carbon dioxide (CO_2) reflects changes in time- and spatial-dependent surface emission and uptake processes, and atmospheric transport and chemistry. Long-term records of atmospheric CO_2, available in some locations for more than half a century, show a near-monotonic increase superimposed with a seasonal cycle. Disentangling signals from individual processes from these data is generally non-trivial but particularly difficult for long-lived trace gases with atmospheric lifetimes of, say, longer than one year where the signal of interest typically represents a variation of, perhaps, only a few percent atop a slowly varying ambient concentration. We are instead reliant on computer models of surface processes and atmospheric transport, which have their own weaknesses, or complex analysis of the time series. Here, I use the wavelet transform to spectrally decompose CO_2 time series across the globe, revealing new insights about the growth rate, and changes in the amplitude and phase of CO_2 associated with the growing season.

A growing body of work shows that terrestrial ecosystems are particularly sensitive to changes in climate at the start and end of the growing season, largely based on relating earlier flowering and leaf flushing dates at mid-latitudes to warmer springtime temperatures (e.g., Schwartz *et al.* (2006); Taylor *et al.* (2008); Thompson and Clark (2008); Ellwood *et al.* (2013)). Predictions based on experimental studies have been unable to reproduce the sign or the magnitude of the observed variations in leaf phenology (Wolkovich *et al.*, 2012). Studies have typically shown a weaker relationship between autumn surface temperatures and the timing of leaf loss, with some work suggesting that increasing CO_2 contributes to delayed autumnal senescence (Taylor *et al.*, 2008). Changes in phenology have implications for carbon fluxes, and the associated analysis of the observed variability of atmospheric CO_2 generally supports the conclusions from the phenology studies of spring warming (Thompson, 2011). Keeling *et al.* (1996) reported an increase in the peak-to-peak amplitude of the seasonal cycle at Mauna Loa, Hawaii and Barrow, Alaska, interpreted as an indicator of increased activity of northern vegetation, and a change in the phase suggesting a lengthening of the growing season in response to warmer spring temperatures. A more update study by Graven *et al.* (2013) has shown that the increase in seasonal amplitude has persisted at Barrow, Alaska and can also be seen in aircraft measurements in the mid-troposphere, and that these changes, evident of increased CO_2 uptake by boreal and temperate forests, show no signs of slowing down. Later studies have showed that carbon uptake in the northern hemisphere is starting earlier in spring and that the release of carbon is also starting sooner in autumn (Piao *et al.*, 2008) in response to changes in the thermal growing season (Barichivich *et al.*, 2012) and snow melt dates (Barichivich *et al.*, 2013). Spectral decomposition of atmospheric measurements of CO_2 is not a new idea, with Keeling providing some of the early insights into his measurements at Mauna Loa. Previous studies have typically employed curve fitting techniques (e.g. Bacastow *et al.* (1985), Thompson *et al.* (1986), Piao *et al.* (2008) and Barichivich *et al.* (2012)) or filtering methods such as complex demodulation (Thompson and Clark (2008) and Thompson (2011). However there are inherent problems with analyses which focus on detrended seasonal cycles, in particular the aliasing effects that occur as a result of the detrending process.

I apply the wavelet transform (Torrence and Compo, 1998) to CO_2 mole fraction data, which simultaneously decomposes time series into time-frequency space, while preserving information about both the amplitude and phase of oscillations within the time series. When used as a filtering technique, this transform has an advantage over traditional filtering methods in that it removes noise at all frequencies and can be used to isolate single events that have a broad power spectrum or multiple events that have a varying frequency. This method provides easy isolation of changes in the CO_2 growth rate and seasonal cycle. I characterise the aliasing effects that result from the detrending process in order to determine the best metrics for estimating trends in the seasonal cycle. My data analysis is focused on high northern latitude sites where the boreal CO_2 seasonal cycle has a high signal-to-noise ratio relating to strong boreal terrestrial carbon fluxes.

In Section 2.2, I describe the data and methods used in the analysis. In Section 2.3, I describe the wavelet transform that I use to spectrally decompose the data and characterize the aliasing errors associated with detrending the data. I also compare my CO_2 growth rate estimates with those reported by NOAA/ESRL at Mauna Loa to quantify the uncertainty associated with both methods. In Section

2.4, I quantify the regional contributions to high-latitude CO_2 concentrations. In Section 2.5, I analyse global atmospheric CO_2 growth rates, and I use the wavelet transform to produce detrended time series of CO_2. I quantify changes in the amplitude and phase of the high-latitude seasonal cycle over the past 40 years at numerous high-latitude CO_2 monitoring sites. In Section 2.6, I further investigate the results by using gridded temperature data and CO_2 isotope observations. I conclude in Section 2.7.

2.2 Data and Methods

2.2.1 CO_2 and $\delta^{13}C$ Data

I use weekly mean CO_2 time series calculated from NOAA/ESRL CGASN discrete CO_2 surface mole fraction measurements, with geographical site locations shown in Figure 2.1. At each of these monitoring sites, flasks of air are collected twice weekly by the NOAA/ESRL GMD when conditions are considered representative of background conditions, before the CO_2 dry air mole fraction is determined using a non-dispersive infrared analyser. Ongoing calibrations at each site ensures reasonable accuracy of individual measurements and allows reliable intercomparisons of data time series within the NOAA/ESRL network. Uncertainties of discrete CO_2 measurements are calculated based on the ability to propagate the World Meteorological Organisation (WMO) XCO2 scale to working standards (±0.02 ppm based on a 68% confidence interval, Zhao and Tans (2006)), analytical repeatability when using the analysers for sample measurement (±0.03 ppm), and the agreement between pairs of samples collected simultaneously (±0.1 ppm across the entire sampling network). Comparison of monthly mean CO_2 at Mauna Loa determined independently by NOAA/ESRL and Scripps Institution of Oceanography (SIO) shows an average difference during 1974-2004 of 0.04 ppm with a standard deviation of the annual mean differences of 0.12 ppm - these comparisons provide confidence that the NOAA/ESRL CO_2 measurements are generally accurate to better than 0.2 ppm. The sum of these uncertainties is negligible in comparison to the magnitude of CO_2 variability observed at northern high-latitudes where there is a strong seasonal cycle.

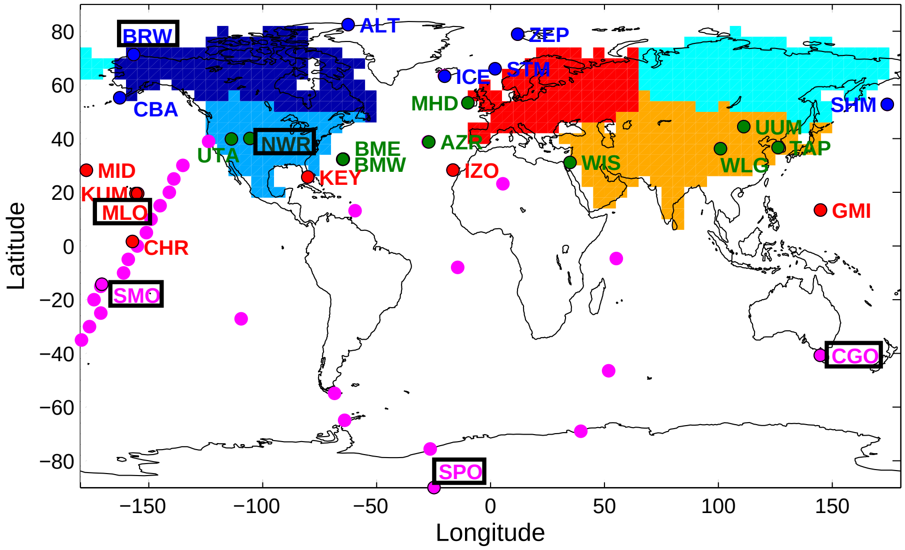

Figure 2.1: The locations of NOAA/ESRL sites used in my CO_2 time series analysis. For seasonal cycle analysis, I focus on northern hemisphere high-latitude sites marked in blue, where mid and low-latitudes sites are marked in green and red respectively. The sites shown in magenta, blue and green are used for growth rate analysis only. The six sites with a black border are those with the longest time span in each 30° latitude band. The shaded regions are the temperate and boreal northern hemisphere land regions defined in the initial TransCom study (Gurney *et al.*, 2002). These regions are used for analysis of temperature and atmospheric transport.

I also use coinciding measurements of $\delta^{13}C$ to help us attribute observed changes of CO_2 to land biospheric uptake. The isotope samples are analysed at the Stable Isotope Laboratory at The Institute of Arctic and Alpine Research within Colorado University (CU-INSTAAR) using flasks of air from the CGASN (White and Vaughn, 2011a). Precision is estimated to be approximately 0.028 permil for δ^{13}C-CO$_2$. The ratio δ^{13}C is defined as:

$$\delta^{13}C = \left[\frac{\left[\frac{^{13}C}{^{12}C}\right]_{sample}}{\left[\frac{^{13}C}{^{12}C}\right]_{standard}} - 1 \right] \times 1000, \qquad (2.1)$$

where $\left[\frac{^{13}C}{^{12}C}\right]_{sample}$ is the ratio of ^{13}C to ^{12}C within the sample, and $\left[\frac{^{13}C}{^{12}C}\right]_{sample}$ is the ratio of ^{13}C to ^{12}C in a standard (a substance with a known, unchanging ^{13}C to ^{12}C ratio). Individual measurements of ^{12}C and ^{13}C are carried out by isolating the CO$_2$ in a subsample of air from each flask and using a mass spectrometer to determine the isotopic composition. Measurements of δ^{13}C show strong seasonal variations, which are anti-correlated with CO$_2$. Plants preferentially take the lighter carbon ^{12}C isotope out of the atmosphere through photosynthesis during spring and summer resulting in an increase in δ^{13}C, and release more ^{12}C than ^{12}C during autumn and winter resulting in a decrease in δ^{13}C.

I only use data from sites where the length of the time series is at least 15 years, reflecting my primary interest of understanding long-term responses of CO$_2$ to changes in climate. Although there are typically more temporal discontinuities than monthly data, I focus on analysis of weekly mean CO$_2$ as it provides more detailed information about changes in the phase of the seasonal cycle.

The wavelet transform method requires a continuous time series with a constant time step and it is therefore necessary to impute missing data. To fill a missing value in the time series I extract a seasonal value from a locally averaged seasonal cycle (calculated from the 2 years to either side of the missing value) and a trend value from a latitude-specific reference time series (Figure 2.2), accounting for large-scale anomalies in the growth rate. Any remaining missing data points are extracted from a piecewise cubic spline curve-fit. Figure 2.3 shows an example of my imputation approach using CO$_2$ mole fraction and δ^{13}C time series from Cold

Bay, Alaska (CBA). At this site, there are typically few missing data points but there are periods of >1 year with no data at all. Parts of the time series that contain significant sections of missing data are likely to be unreliable, however prolonged periods are rare, with CBA being one of the worst examples, and I find that isolated missing data points do not significantly impact the determination of long-term trends in the phase and amplitude.

For analysis of atmospheric growth rates, I use estimates of CO_2 emissions from land use change and those resulting from the combined effects of fossil fuel combustion and cement production throughout 1960-2010. This data was sourced from the Global Carbon Project (Le Quéré *et al.*, 2014).

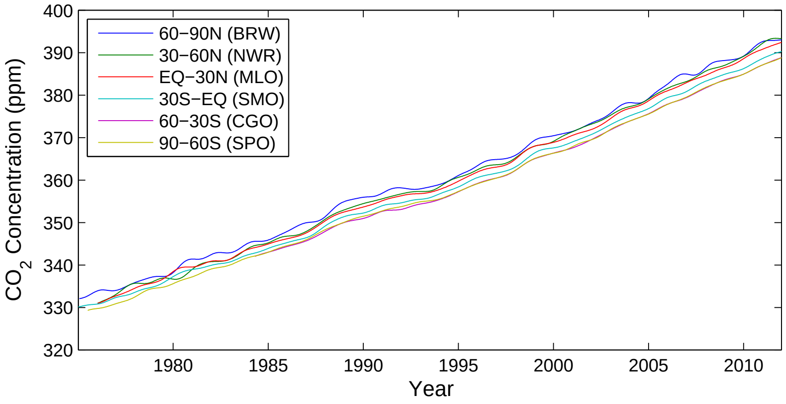

Figure 2.2: Reference weekly CO_2 mole fraction measurements (ppm) covering various time spans for 30° degree latitude bands used to impute missing data points. BRW, NWR, MLO, SMO, CGO, and SPO are codes to denote Barrow (71.3°N, 156.6°W), Niwot Ridge (40.0°N, 105.6°W), Mauna Loa (19.5°N, 155.6°W), American Samoa (14.2°S, 170.5°W), Cape Grim (40.7°S, 144.7°E), and South Pole (89.9°S, 24.8°W). Also see Figure 2.1 for site locations.

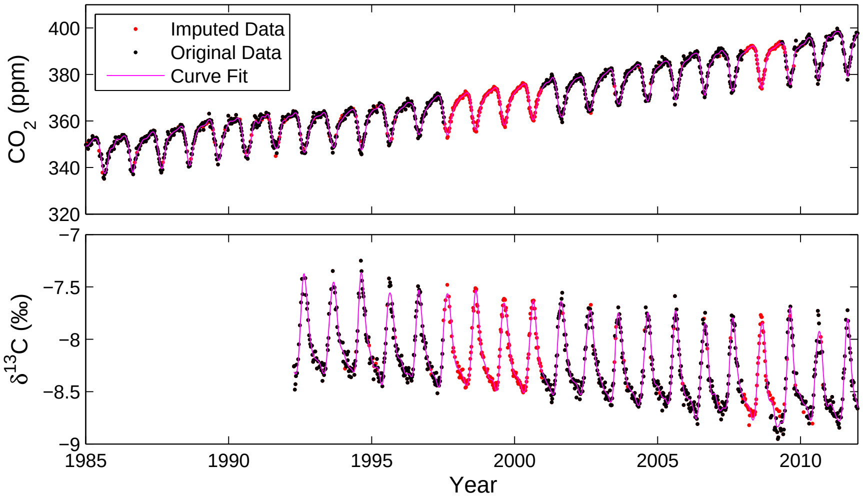

Figure 2.3: Weekly (top) CO_2 mole fraction (ppm) measurements (black) and (bottom) δ^{13}C values (per mil) at Cold Bay, Alaska (CBA, 55.2°N, 162.7°W) from 1980 to 2012. Imputed values, shown in red, are inferred from a locally averaged seasonal cycle adjusted for anomalies in growth rate. Any remaining missing values are extracted from a fitted piecewise cubic spline curve (magenta).

2.2.2 GEOS-Chem Atmospheric Transport Model

I use output from the GEOS-Chem ACTM to help interpret results from the CO_2 data analysis. In particular, this model output is used to estimate the proportion of seasonal variability in CO_2 observed at surface monitoring sites driven by carbon fluxes in different geographical regions.

Model Description

The GEOS-Chem model output was provided by Liang Feng of the Tropospheric Chemistry and Earth Observation Modelling Group within the School of Geosciences at the University of Edinburgh. The model output was produced using v7-03-06 of the GEOS-Chem ACTM, driven by GEOS-5 assimilated meteorological data from the NASA Global Modelling and Assimilation Office (GMAO) Goddard Earth Observing System (GEOS). It uses a horizontal spatial resolution of $4°$ latitude by $5°$ longitude (a degradation of the native resolution of $0.5° \times 0.667°$) with 47 vertical levels and a temporal resolution of 3 hours. The model uses prior CO_2 fluxes for the land biosphere (Randerson *et al.*, 1997), oceans (Takahashi *et al.*, 2002), biomass burning (GFEDv2), and fossil fuel combustion (Sunthar-alingam *et al.*, 2005). For the CO_2 attribution calculations, a "tagged" version of the model is used (Feng *et al.*, 2011), which decomposes the total CO_2 into contributions from specific processes and geographical regions. The 23 regions used here are those often adopted from the original CO_2 TransCom experiments (Gurney *et al.*, 2002). These include the boreal and temperate regions of North America, Europe and Asia.

Model Simulation

The simulation used is a perturbation simulation from 2004-2009. In the simulation, on the first day of every month, each region releases a fixed quantity of 1 $PgCO_2$ from the surface, which is then transported by the GEOS-5 meteorology.

The CO_2 is tagged by region and month of the year. I find and sample CO_2 at the nearest model grid point to each of the NOAA/ESRL CO_2 measurement sites to build up daily CO_2 time series over the five year period. In order to reflect the different magnitude of carbon fluxes from different regions and the fact that CO_2 fluxes vary seasonally, the 1 $PgCO_2$ is multiplied by the prior flux estimate for that region. The prior fluxes vary seasonally, but not from year to year. I then derive the relative quantities of CO_2 arriving at each site from different regions and times of the year. For each site, I take the maximum contribution from each region in the first 30 days from the initial monthly flux into the atmosphere.

2.2.3 Other Data

I use the University of East Anglia Climate Research Unit TS3.10 gridded land temperature dataset (Harris *et al.*, 2013) to help interpret observed variations in the CO_2 time series. This data has a 0.5×0.5 degree spatial resolution and monthly time resolution. I calculate regional mean time series of temperature using the northern hemisphere TransCom regions shown in Figure 2.1. This accounts for the fact that CO_2 measurements typically have a larger spatial footprint than the gridded climate data. I analyse the resulting time series through 1960-2012, defining a thermal growing season (TGS), where TGS_{BEG} is the 5°C spring crossing date (-ve to +ve), and TGS_{END} is the the 5°C autumn crossing date (+ve to -ve). This is equivalent to the method adopted by Barichivich *et al.* (2012). During this warm period of days >5°C (TGS_{LEN}), soil is likely to have thawed and temperatures are sufficient for plants to become active during the growing season. I regress these variables with with CO_2 seasonal cycle phase metrics.

I originally chose this dataset due to its long-time span, which went as far back as the beginning of the continuous CO_2 measurements at Mauna Loa. Although it was unnecessary to use such a long time series in this particular analysis, I found that the difference in results when doing the same analysis with other temperature datasets was insignificant.

2.2.4 Statistical Methods

I use standard linear regression to calculate regression coefficients and their 95% confidence intervals. I use the F statistic and its p value to test for statistical significance of trends. In an F-test, the test statistic has an F distribution under the null hypothesis - that there is no statistical relationship between two time series. In my analysis I assume that coefficients with $p < 0.05$ and $p < 0.01$ are statistically significant and highly statistically significant respectively, while a p value >0.05 represents a result that is not statistically significant. Unless otherwise specified, regression coefficients refer to the linear regression of a variable against time, where a statistically significant coefficient would indicate the presence of a trend. I use the Pearson product-moment correlation coefficient r, in order to determine the linear correlation between two time series. I use a Monte Carlo simulation to empirically derive estimates of uncertainty associated with the different seasonal cycle metrics used in my analysis.

For regression of CO_2 against $\delta^{13}C$ metrics, Method I (linear) regression is not appropriate because it assumes that there is no error associated with the dependent variable, and that the errors in the two variables are unrelated. This is not the case, as errors are likely to be present in both $\delta^{13}C$ and CO_2 and they are related because one is present in the other. These errors carry through to the phase metrics used in the analysis and therefore an alternative regression method is required. I use Method II regression, Reduced Major Axis

(RMA) Regression, which is also known as Geometric Mean Regression. RMA is specifically formulated to account for there being errors in both the x and y variables. This method provides regression coefficients, a 95% confidence interval on each coefficient, and a p value associated with the statistical significance of the relationship. I interpret these values as I do for those determined from standard linear regression.

2.3 Wavelet transform: methodology and error characterization

2.3.1 Method

I use a wavelet transform to spectrally decompose the observed CO_2 variations into individual frequency bands that can be attributed to the responsible biological and physical processes.

In general a wavelet transform W_n uses a wavelet function ψ_0, a pre-defined wave-like oscillation that is non-continuous in time or space, to decompose a time series into time-frequency space. This allows an investigation of the dominant modes of variability within a time series and how they change with time. This improves on the Fourier transform which determines frequency information using continuous sine and cosine functions.

The wavelet transform of a time series x_n is defined as

$$W_n(s) = \sum_{k=0}^{N-1} \hat{x}_k \hat{\psi} * (s\omega_k) e^{i\omega_k n\delta t} \tag{2.2}$$

where $\hat{x}_k$ is the discrete Fourier transform of x_n, N is the number of points in the time series, k=0...$N-1$ is the frequency index and $\hat{\psi} * (s\omega_k)$ is the complex conjugate of the Fourier transform of a normalized, scaled and translated version of $\psi_0(\eta)$, where s is the scale and ω_k is the angular frequency. I use the Morlet wavelet (Torrence and Compo, 1998), a plane wave modulated by a Gaussian envelope:

$$\psi_0\left(\eta\right) = \pi^{-1/4} e^{i\omega_0\eta} e^{-\eta^2/2} \tag{2.3}$$

where ω_0 is the nondimensional frequency and η is the nondimensional time-parameter. I chose the Morlet wavelet because it is nonorthogonal, which is an attractive property for the analysis of smooth and continuous variations such as those exhibited by CO_2 mole fraction time series. The wavelet is comprised of a real and imaginary part, providing information about amplitude and phase, respectively.

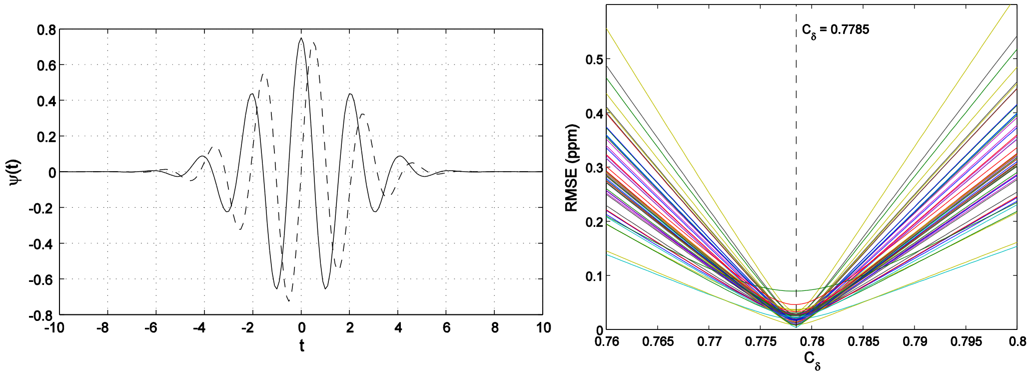

Figure 2.4: The left panel shows the real (solid) and imaginary (dashed) parts of the Morlet wavelet. The right panel shows the root mean square errors associated with different values of C_δ derived empirically from residuals determined by subtracting the reconstructed CO_2 time series from the original time series, where individually coloured lines are representative of different CO_2 monitoring sites.

The original time series can be recovered from wavelet space using the corresponding inverse transform Torrence and Compo (1998) and summing over all frequencies from the real part of the wavelet transform (or a subset of frequencies if the focus is isolating particular signals):

$$\hat{W}_n = \frac{\delta j \delta t^{1/2}}{C_\delta \psi_0(0)} \sum_{j=0}^{J} \frac{\Re\left\{W_n(s_j)\right\}}{s_j^{1/2}}, \tag{2.4}$$

where $\psi_0(0)$ removes the energy scaling and $s_j^{1/2}$ converts the wavelet transform to an energy density. C_δ and $\psi_0(0)$ are constants determined for the specific wavelet function. In order to determine the optimum range of frequencies over which to sum in order to reconstruct broad scale frequency components I generated a time series equal to the sum of three individual sine waves with equal magnitude but specific periods of 12, 6 and 4 months. Figure 2.5 shows the global wavelet spectrum of this time series, where the global wavelet spectrum is the power of the wavelet coefficient matrix summed over time. The dashed lines show the points of minimum overlap between different frequency components of the time series and are used as thresholds when reconstructing individual harmonics of the wavelet transformed data.

To minimize edge effects associated with the Fourier transform, I add synthetic data to pad the start and end of the time series. For my calculation I repeat the first (last) three years of data backward (forward), accounting for a growth rate based on following (preceding) years. I also “zero pad” the time series so that the number of points used is an integral power of two, as this further reduces edge effects and speeds up the transform. The addition of the padded synthetic data allows utilisation of the edges of the time series by ensuring that there is negligible additional error introduced by edge effects, but uncertainty in the spectral decomposition is still likely to be largest at these points. The padded data at the edges of the time series are removed prior to analysis after the time series has been wavelet decomposed, filtered, and reconstructed.

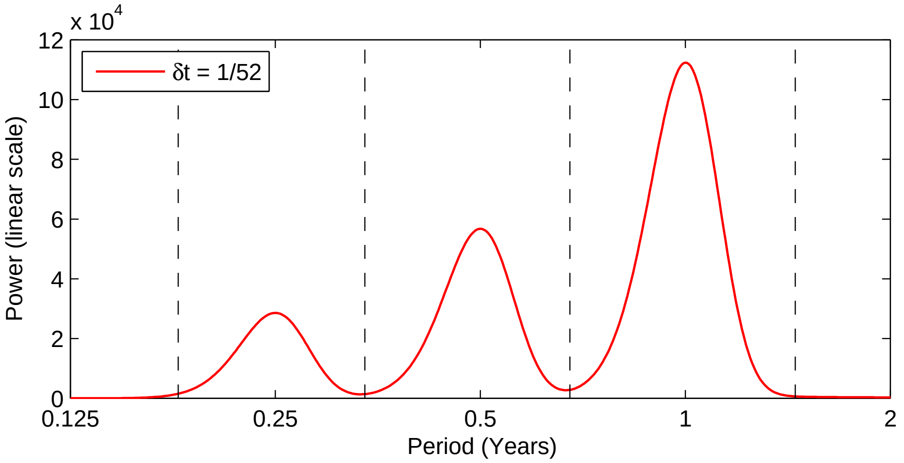

Figure 2.5: The global wavelet spectrum, defined as the power of the wavelet coefficient matrix summed over time, of a time series made up of three individual sine curves of equal magnitude but with periods of 12, 6 and 4 months respectively. The dashed lines show the points at which there is minimum overlap between the different components.

I quantify the numerical error associated with the wavelet transform by decomposing and reconstructing multiple time series before calculating the root mean square error (RMSE) from the residuals. I find that the value for C_δ previously reported (Torrence and Compo, 1998) introduces a small trend in the original minus reconstructed residual, and find that C_δ=0.7785 results in a much smaller, unbiased residual and RMSE with a typical value <0.05 ppm for monthly data and <0.025 ppm for weekly data (see Figure 2.4). Table 2.1 shows the wavelet parameter values I used in my analysis.

Additional uncertainties may arise in the long-term trend and detrended seasonal cycle as a result of spectral power being assigned to the incorrect frequency band. This could, for example, result in concentration changes caused by anthropogenic emissions creeping into what we deem the natural (seasonal) cycle of CO_2; the converse is also true. However, this problem is prevalent amongst most methods used to decompose the time series.

Table 2.1: Wavelet parameters

Parameter	δt=1/12	δt=1/52
δj	0.25	0.01
s_0	2δt	δt
C_δ	0.7785	0.7785
ψ_0	$\pi^{-\frac{1}{4}}$	$\pi^{-\frac{1}{4}}$

Example of spectral decomposition

Figure 2.6 shows, as an example, the spectral decomposition of CO_2 mole fraction measurements at Mauna Loa. The wavelet transform decomposes the 1-D time series into a 2-D power spectrum, describing energy per unit time, as a function of frequency (the reciprocal of period) and time. The cone of influence is the boundary below which wavelet coefficients are compromised by edge effects. I find that most of the power is in the annual and semi-annual periods, as expected, but also peaks in power at periods $>$ 12 months. This is likely to be a result of responses of the CO_2 growth rate to large-scale climate variability, e.g., the El Niño-Southern Oscillation (ENSO). This is supported by the global wavelet power spectra (integrated over all time). The interannual growth rate is determined by taking the value of the long-term trend (deseasonalized) on January 1st in one year, and subtracting the value from the previous year to leave the net change in concentration.

Figure 2.6 shows two example applications of the wavelet transform: 1) as a low-pass filter to deseasonalize the CO_2 data (red line in top panel); and 2) the associated annual growth rate (ppm/yr), which I find is within <0.1 ppm of the reported values from NOAA/ESRL (not shown).

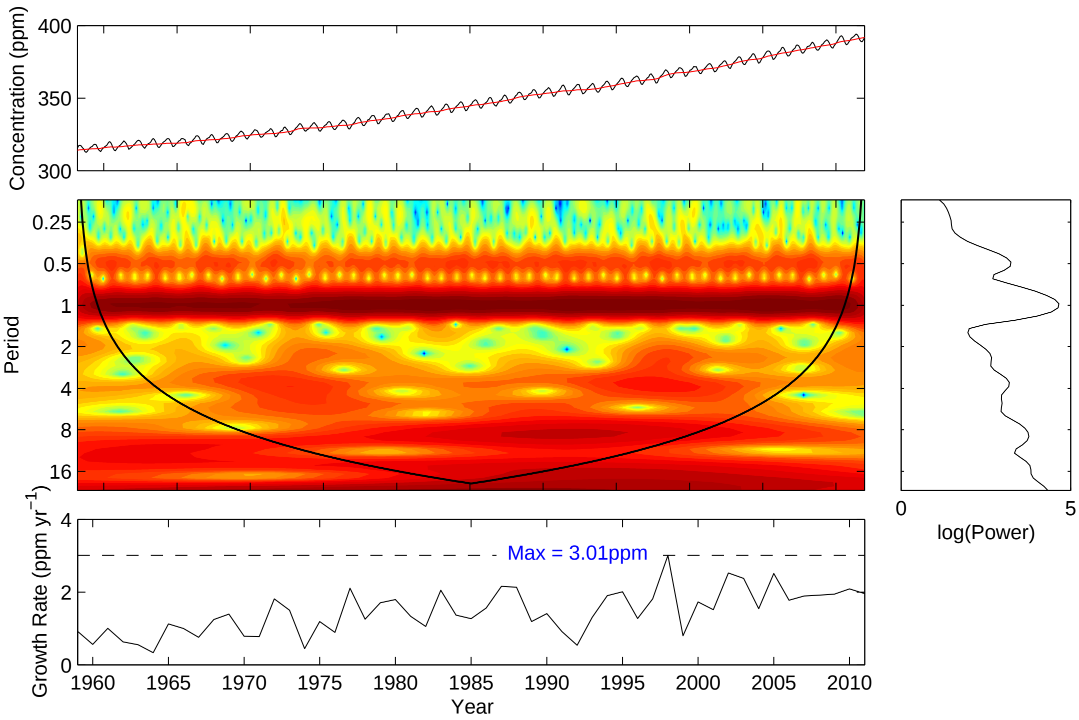

Figure 2.6: Top row: weekly mean (black) and low-pass filtered (red, frequencies >18 months) CO_2 mole fraction time series (ppm) at Mauna Loa, 1959-2012. Middle row: (left) the wavelet power spectrum where the colour scale is $\log$(power). The black solid lines denotes the cone of influence. The wavelet power spectrum tends to emphasise very low frequency information so I have subtracted an exponential term prior to applying the wavelet transform to emphasise the high frequency variability (right) the corresponding time-integrated global wavelet spectrum. Bottom row: the inferred annual growth rate of CO_2 (ppm/yr).

Components of the Seasonal Cycle

The annual cycle of CO_2 in the high-latitude northern hemisphere is driven primarily by photosynthesis and respiration of terrestrial vegetation, with a minima during the summer growing season months and a maxima during the winter months. The seasonal contribution from ocean sources and sinks is relatively small. This is discussed further in Section 2.4.

Past analyses of surface and aircraft in situ CO_2 concentration measurements have shown the presence of a semi-annual cycle in mid-tropospheric and surface CO_2 (e.g. Thompson *et al.* (1986), Jiang *et al.* (2012)). This signal has recently been attributed to biosphere-atmosphere CO_2 exchange with a small contribution from biomass burning (Jiang *et al.*, 2012), although better knowledge of ocean fluxes is also required to determine their contribution to the CO_2 semi-annual cycle. The semi-annual cycle has a minima during winter and summer just prior to the maxima and minima of the annual cycle, and has a maxima during spring and autumn just prior to times of peak net uptake and release of CO_2, respectively.

In terms of spectral decomposition, the presence of a semi-annual cycle in high-latitude CO_2 is not surprising. This is because the high-latitude seasonal cycle is not sinusoidal, but instead varies asymmetrically. Consequently, it is important to consider both the semi-annual and annual cycles together when interpreting changes in the phase of the seasonal cycle. For this reason, and based on the analysis of the global wavelet spectrums shown in Figures 2.6 and 2.5, I find that using periods of $>$2 months and $<$18 months to construct the CO_2 seasonal cycle adequately describes variability in the phase and amplitude.

In the next section, I define a number of metrics which describe different ways in which the seasonal cycle changes shape. I use a series of numerical experiments based on synthetic data to characterise the aliasing errors associated with detrending the seasonal cycle and the ability to detect trends and interannual variability in each of the metrics.

2.3.2 Error characterisation

Although the atmospheric growth rate of CO_2 contains important information about the carbon balance of large-scale vegetation, it is mixed in with information about many other sources and sinks of CO_2 such as oceanic and anthropogenic sources. The seasonal cycle on the other hand is predominantly driven by seasonal changes in the uptake and release of carbon by terrestrial vegetation. Furthermore, the high-latitude seasonal cycle is predominantly driven by boreal vegetation (see Section 2.4). It would therefore make sense that analysing this seasonal cycle could provide invaluable insights into changes in the CO_2 flux from boreal vegetation.

The wavelet detrended seasonal cycle of CO_2 contains a zero net annual flux by definition. Therefore, analysis of the detrended CO_2 seasonal cycle does not provide direct evidence about the balance between uptake and release of carbon. Furthermore, the detrending process can compromise our ability to accurately determine changes in the seasonal cycle - a result of aliasing. Here, I use synthetic CO_2 time series, defined with specific changes in amplitude and phase, to characterize the aliasing errors associated with analysing CO_2 concentration time series that have been detrended using the wavelet transform. Insights from this synthetic analysis will be applied to the interpretation of NOAA/ESRL mole fraction measurements. I attempt to use a number of metrics defined below to provide indirect evidence of trends in the carbon balance of the northern hemisphere.

The starting point of my numerical experiments is the detrended time series of atmospheric CO_2 mole fraction and it's first time derivative, $\Delta_t CO_2$.

Synthetic model framework

I use a simple box model based on the CO_2 mole fraction time series at BRW (Figure 2.7). BRW is the most suitable site for this purpose because it has the longest time series of all of the high-latitude sites and is considered highly representative of boreal vegetation in the northern hemisphere. I take the first time derivative of the detrended time series at BRW to get the "flux" time series, $\Delta_t CO_2$. I then take the time series mean seasonal cycle of the BRW CO_2 flux and adjust it so that in its initial state, the source and sink terms are balanced. This cycle is then repeated for 40 years which is roughly equivalent to the time span of the BRW data. For my experiments, described below, I apply trends and variability to various aspects of the CO_2 flux time series before integrating to retrieve the CO_2 concentration. The resulting concentration time series emulates an observed time series.

In these experiments, the trends are introduced to the flux time series rather than the mole fraction time series because this includes in the analysis the changes in the interannual growth rate which are now present due to the imbalance between the source and sink terms. If I were to instead apply the trends to the CO_2 mole fraction time series, the only error introduced would be the numerical error of the wavelet transform which is negligible.

Biological period defined by atmospheric CO_2

Based on the flux time series I define three periods during an annual cycle: 1) a carbon uptake period when there is a net negative CO_2 flux to the atmosphere (photosynthesis is higher than respiration); 2) a release period when there is a net source of CO_2 to the atmosphere; and 3) a dormant period, defined between the

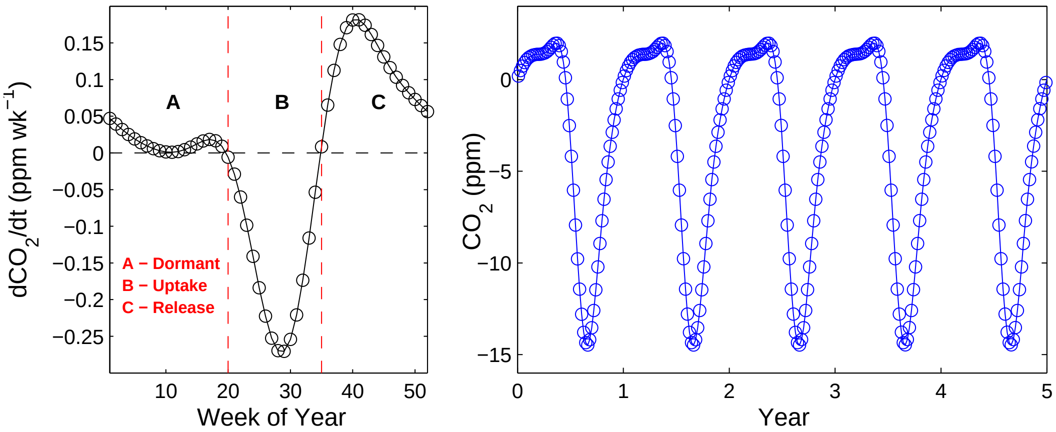

Figure 2.7: Synthetic CO_2 'flux', expressed here at ppm/wk over an annual cycle (left) and the corresponding mole fraction (ppm) time series repeated over successive years (right). The CO_2 annual cycle is based on the observed cycle at BRW.

latter half of winter and the start of the next uptake period, when plant activity is very low due to frozen ground such that $\Delta_t CO_2$ is typically small (but non-zero due to transport of CO_2 from the lower latitudes).

Metrics used to interpret atmospheric CO_2 variations

I use several metrics from the time series analysis, each of them determined from the detrended CO_2 seasonal cycle: the seasonal amplitude and zero-crossing points of the CO_2 mole fraction, and peak uptake/release and numerous phase thresholds from the first time differential of CO_2, $\Delta_t CO_2$.

The amplitude of the seasonal cycle, defined as the peak to peak difference (maxima minus minima) of the seasonal CO_2 mole fraction time series, has been used in previous studies as a measure of biological activity. This metric alone cannot tell us whether net uptake or release is responsible for observed variations in the seasonal cycle, but previous work has shown that it tends to have a stronger

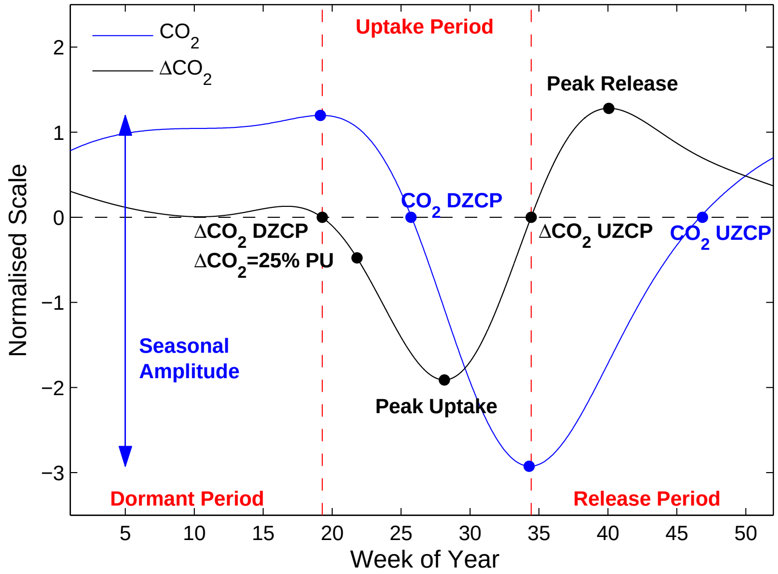

Figure 2.8: A schematic of the measures I used to characterize changes in the amplitude and phase of atmospheric CO_2 (ppm). In this example I use detrended annual and semi-annual components of CO_2 data from BRW.

relationship with the period of strong net uptake during summer months (Graven *et al.*, 2013). Zero-crossing points refer to times when the detrended seasonal cycle is equal to zero. For a seasonal cycle there is a downward and upward ZCP (DZCP and UZCP, respectively) within one year. The DZCP does not necessarily correspond with spring onset, but can be considered as a proxy; similarly, the UZCP is a proxy for the timing of autumn carbon release but typically lies near to the end of the period of net carbon release. Peak uptake (PU) and peak release (PR) refers to the minima and maxima of the flux time series respectively. Changes in $\Delta_t CO_2$ have a clearer physical interpretation than the concentration ZCPs. For example, the $\Delta_t CO_2$ DZCP and UZCP is the approximate timing of when terrestrial vegetation becomes a net sink or a net source of CO_2 respectively. For $\Delta_t CO_2$ I use a number of additional phase thresholds which represent the timing of when certain thresholds in $\Delta_t CO_2$ are reached (e.g. 25% of peak uptake). The $\Delta_t CO_2$ DZCP is more difficult to determine using the BRW seasonal cycle because small mole fraction variations during the dormant period (which has a near-zero flux) are sufficient to bring $\Delta_t CO_2$ below zero prior to the onset of large-scale net uptake. As discussed below a more robust approach is to use 25% of peak uptake as an indicator of spring timing rather than the DZCP. In contrast, the $\Delta_t CO_2$ UZCP is well defined and trivial to calculate. Finally, I define a carbon uptake period (CUP), CO_2 CUP and CUP_Δ for CO_2 and $\Delta_t CO_2$ respectively, where this represents the difference between the autumn and spring phase metrics defined above.

Numerical Experiments

The following three broad set experiments are designed to identify the best metrics to describe changes in the contemporary cycle from detrended CO_2 mole fraction measurements. First, I perturb the timing of spring or autumn by adding or subtracting a smooth Gaussian curve with a flat top centred roughly about the onset of net uptake or release, and increase the magnitude of the curve each year to introduce a trend across the time series. I use a different shaped Gaussian curve for spring and autumn to account for the asymmetry of the seasonal cycle. Second, I perturb the magnitude of net uptake or net release by multiplying the uptake (-ve $\Delta_t CO_2$) or release (+ve $\Delta_t CO_2$) by some factor, and increase the factor each year to introduce a trend. Finally, I add year to year variability (or noise) to each variable in the time series to assess the ability of the spectral method to extract trends from the data. I compare each metric by calculating the % difference in trend from the input time series and the wavelet detrended time series. A series of Monte Carlo simulations allows us to present statistical analysis of our ability to detect trends in the CO_2 time series.

Perturbing the timing of the spring and autumn phases

Figure 2.9 shows the results of the spectral analysis of a time series for which I introduced a progressively earlier onset of net CO_2 uptake of 0.50 days/yr for $\Delta_t CO_2$ DZCP. The $\Delta_t CO_2$ DZCP is very sensitive to the curve I used to perturb the time series due to the relatively flat period of near-zero net flux preceding it (it does not take much to bring this below zero). While for the synthetic example, I have used a smoothed version of the BRW time series, in practice there is substantial variability in the spring shoulder so that it is often difficult to accurately define a trend in the $\Delta_t CO_2$ DZCP. To address this I use an operational definition that is defined as 25% from zero to the peak uptake ($\Delta_t CO_2$=25%PU) - which in this example has a trend of -0.35 days/yr. The $\Delta_t CO_2$ metrics were found to be better at capturing the springtime trend to within 23% and 16% for $\Delta_t CO_2$ DZCP and $\Delta_t CO_2$=25%PU respectively, with the CO_2 mole DZCP underestimating the trend by 63%. This has implications for using this CO_2 mole fraction metric to interpret changes in the spring and autumn phase. There is little change in any of the UZCP metrics (typically <0.025 days/yr) as a result of aliasing. The wavelet detrending introduces a -0.01%/yr trend in peak CO_2 uptake and a concurrent increase in peak CO_2 release of 0.14%/yr corresponding to -0.4% and 5.6% across the 40 year time series respectively. This is considered an aliasing error and is relatively small considering the large trends introduced in spring uptake.

Figure 2.10 shows the same calculation but from introducing an earlier autumn onset of net CO_2 release of 0.30 days/yr with a trend of equivalent magnitude introduced for $\Delta_t CO_2$=25% PR. I find that the metrics for spring phase respond to the prescribed change in autumn phase due to aliasing, where the mole fraction and $\Delta_t CO_2$=0 metrics had non-zero trends up to ∼-0.16 days/yr. All three UZCP phase metrics underestimate the change in the defined phase change by amounts

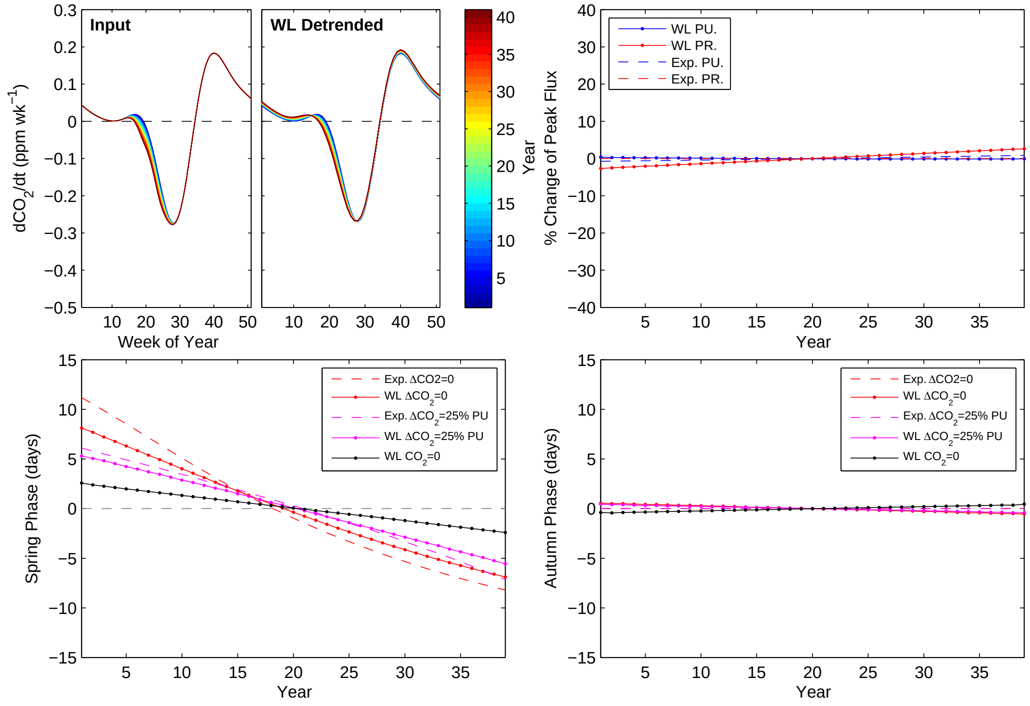

Figure 2.9: Wavelet analysis of $\Delta_t CO_2$ flux time series including a prescribed earlier onset of net CO_2 uptake. Top left panel: the defined flux time series and the associated wavelet detrended time series. Top right panel: the expected (defined) and measured change in peak uptake and release of CO_2. Bottom panels: the expected (defined) and measured change in (left) DZCP and (right) UZCP.

ranging from 11–22% where the CO_2 UZCP performed the best. The earlier onset of net CO_2 release aliases into a 2.5% increase in peak CO_2 release and a 5% increase in peak CO_2 across the entire time series.

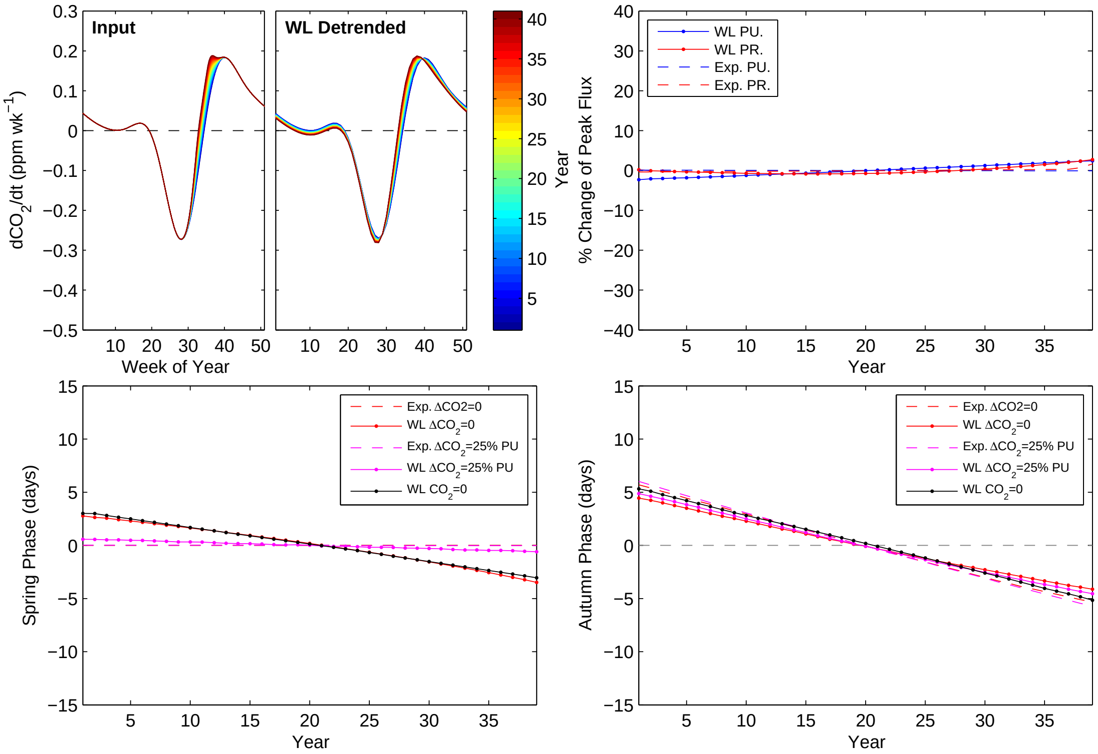

Figure 2.10: As Figure 2.9 but including an earlier autumn onset of net CO_2 release.

Perturbing the periods of net uptake and release of CO_2

Figure 2.11 shows the results of introducing a progressive enhancement of CO_2 uptake of roughly 0.70%/yr, equivalent to a 28% increase over 40 years. I introduce the trend by multiplying the negative flux by an increasing amount each year. This does not have an effect on the timing of the onset of net CO_2 uptake or release. I also introduce two exceptional years to emulate the effect of interannual variability such as variability driven by climate phenomena like ENSO.

I find that the wavelet transform attributes the 0.70%/yr increased uptake as 0.59%/yr uptake and 0.20%/yr release. The mole fraction metrics infer non-zero CO_2 DZCP and UZCP phase changes of 0.06 days/yr and 0.16 days/yr, respectively, while the 25% $\Delta_t CO_2$ DZCP and $\Delta_t CO_2$ UZCP, the operational metrics, exhibits negligible trends as expected. The exceptional years are well captured in the PU metric but also appear as changes in the phase for all phase metrics. The CO_2 UZCP not only exhibits the largest error, but also exhibits the spreading of information from the exceptional years into adjacent years. This is not the case for the $\Delta_t CO_2$ metrics indicating that they are potentially better for estimating interannual variability in the phase.

Simultaneous variations in phase and peak uptake and release

Figure 2.12 shows the results from a final experiment that describes a calculation in which I simultaneously perturb the phase of the spring and autumn, as diagnosed by the $\Delta_t CO_2 = 0$, and the PU and PR. I also superimpose Gaussian random noise of ±10 days and ± 25% to describe year-to-year changes to the phase and to the PU and PR respectively.

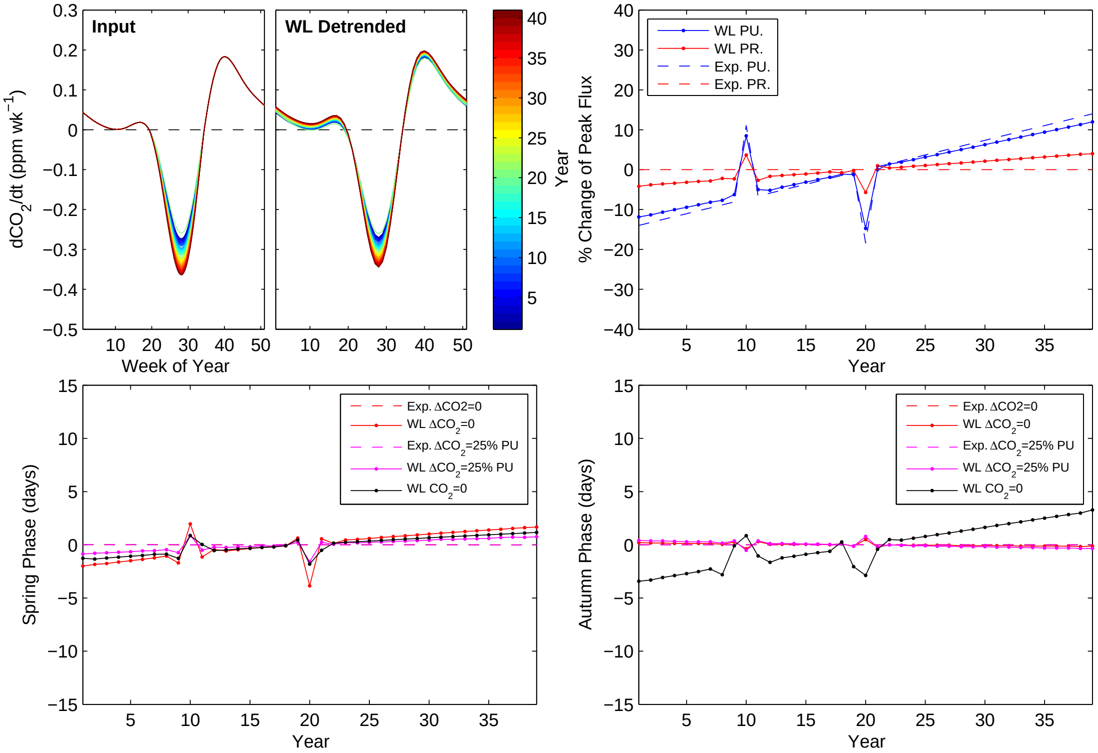

Figure 2.11: As Figure 2.9 but introducing a trend of 0.75%/yr trend in the peak uptake and an anomalously high year for uptake and release in years 10 and 20 respectively.

Despite large interannual variability, there is a negligible trend in the spring timing of CO_2 uptake (-0.02 days/yr). This is also shown by the $\Delta_t CO_2$ phase metric (0.02 days/yr). The CO_2 DZCP trend has the opposite sign and additionally overestimates the magnitude of the trend by 4×. The trend in the autumn $\Delta_t CO_2$ phase metric (0.05 days/yr) underestimates the expected trend (0.09 days/yr) by ∼45%, while the CO_2 UZCP overestimates it by 2.8×. The estimated trend in PU is 0.54% yr which is 80% of the expected trend (0.68%/yr), while the estimated PR trend (0.14%/yr) is opposite in sign and double the magnitude of the expected trend (-0.07%/yr). The estimated CUP_Δ trend is +ve but roughly zero, which is a little smaller than the expected trend of 0.12 days/yr. The increase in peak uptake (which is 3× larger than the rise in peak release) and the roughly zero trend estimated for the CUP_Δ coincides with an increase in annually integrated net uptake. The trend in net flux in this example is indeed negative with an increase in uptake of -0.16 ppm CO_2/yr.

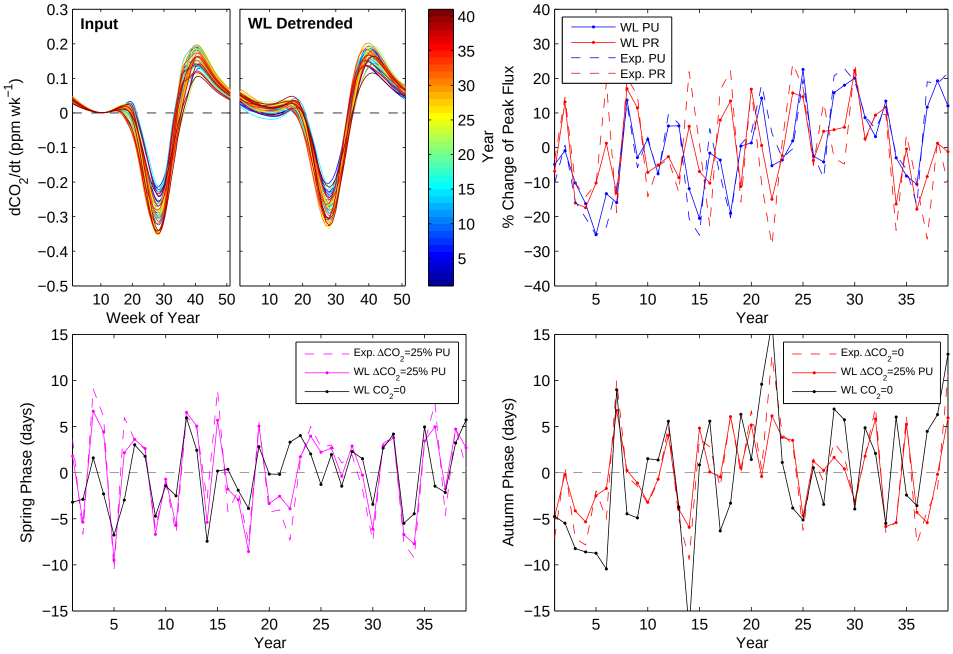

Figure 2.12: As Figure 2.9 but introducing simultaneous trends in spring and autumn phase and in the peak uptake and release of CO_2. I also superimpose Gaussian random noise to describe interannual variation.

So far, analysis of synthetic time series indicates that $\Delta_t CO_2$ metrics can reproduce prescribed phase changes to within 30%, but trends with a magnitude of <0.1 days/yr were uncertain in magnitude and sign. Strong shifts in spring and autumn phase caused changes in PU and PR of <6% due to aliasing. Strong trends in PU and PR were estimated to within 25% of their expected values. Next I repeat these experiments using a Monte Carlo simulation to determine the consistency of results acquired using this analysis when applied to a large number of randomly generated time series.

Monte Carlo simulations

I used a Monte Carlo simulation (MCS) to study the ability of the wavelet transform to simultaneously determine the PU, PR and changes in phase. I generated 1000 synthetic time series with random trends and variability such as the one exhibited in Figure 2.12, where Figure 2.13 shows the probability distributions of the trends introduced in the net carbon fluxes and changes in the CUP. Integrated uptake and release of carbon was in the range of -0.25 to 0.25 ppm/yr^2, while changes in the phase were within 1 day/yr. I regressed the expected trends in phase, PU and PR against the values I estimated following the wavelet detrending and seasonal cycle analysis. The regression coefficient was used as an estimate of the mean bias, while the r^2 is indicative of consistency in the bias and the likelihood of the estimates to deviate far from the expected value.

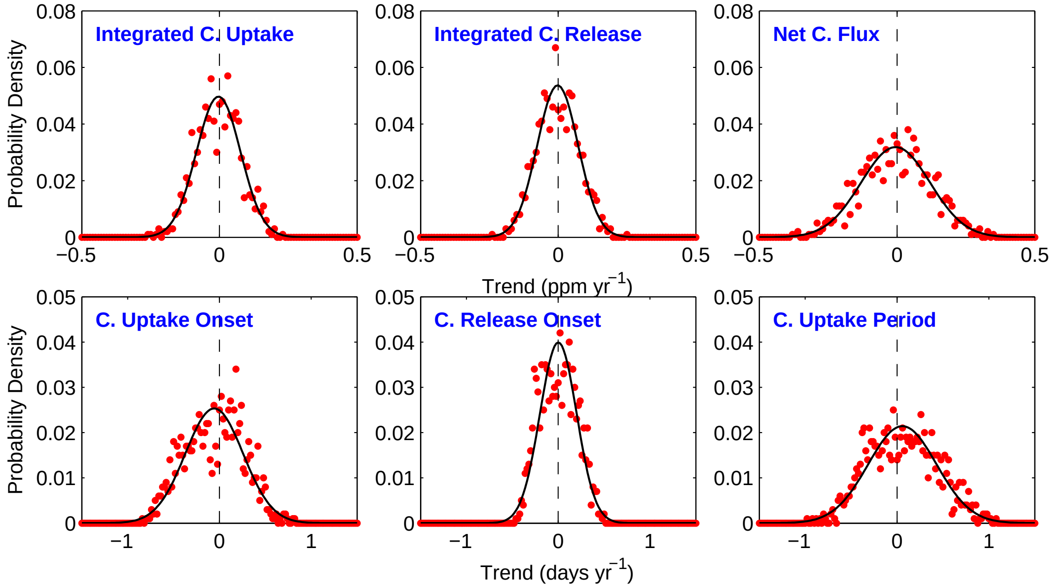

Figure 2.13: Probability densities of trends introduced in the 1000 synthetic time series generated for the MCS where the black line is the fitted probability distribution.

Figure 2.14 shows the results from the MCS regression analysis where I compare

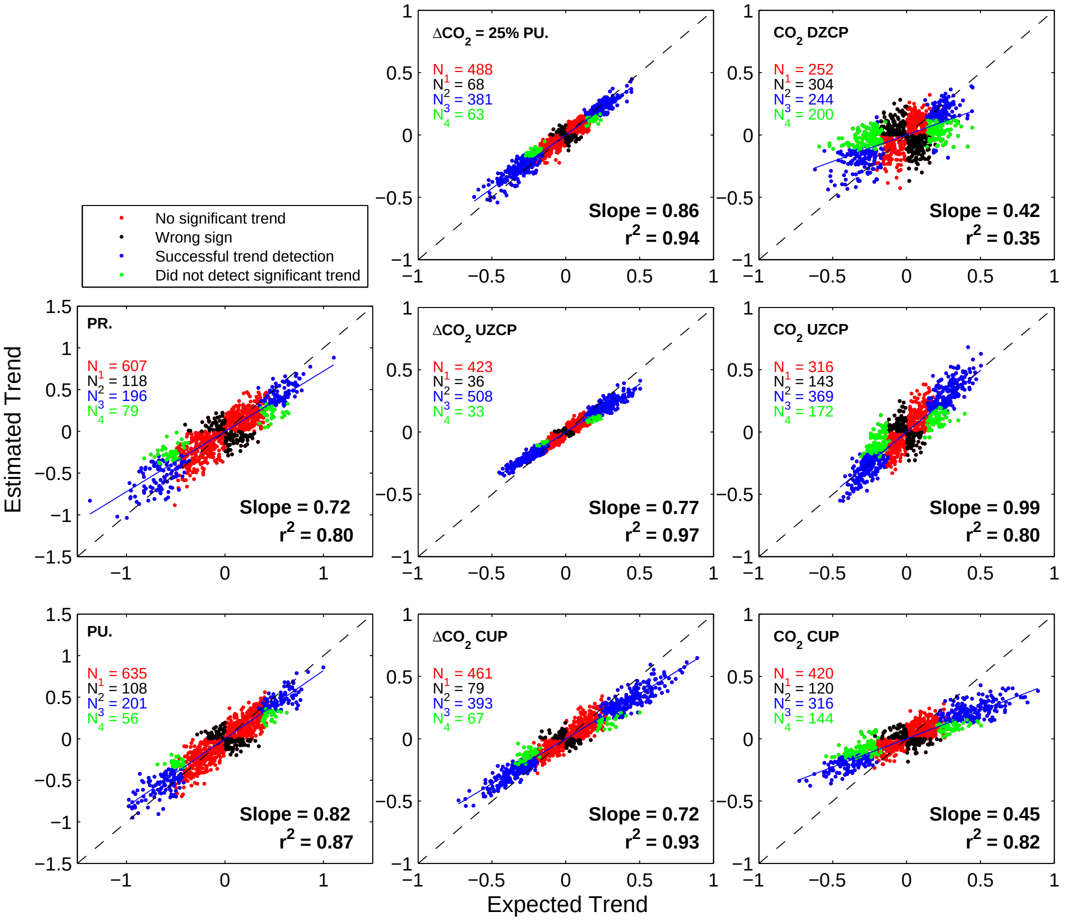

Figure 2.14: Regression of expected and estimated linear trends for PU, PR and the $\Delta_t CO_2$ and CO_2 phase metrics. Coloured points represent trends that were not statistically significant (red), trends where the estimate had the incorrect sign (black), statistically significant trends that were successfully detected (blue), and statistically significant trends that were not detected in the analysis (green). Statistical significance is at the 5% level. The numbers, $N_{1..n}$, are the number of points in each category and have a sum of 1000.

expected and estimated trends. The figure also shows the number of estimates where a trend of incorrect sign was detected and the number of statistically significant trends ($p<0.05$) that were and were not detected in the analysis. The

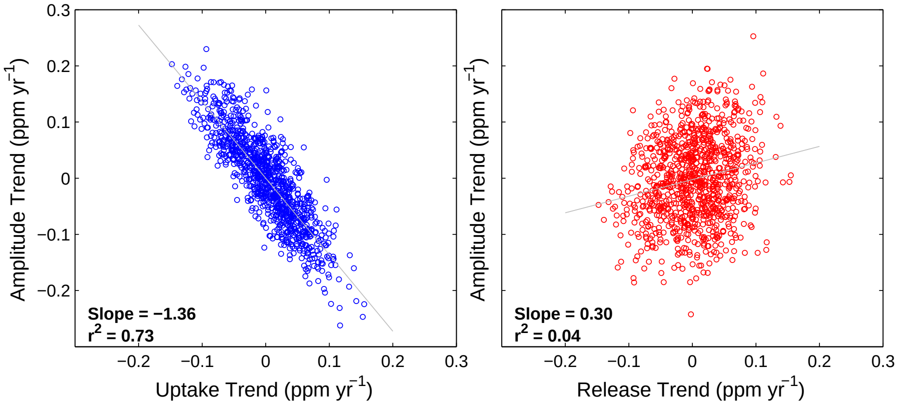

Figure 2.15: Regression of linear trends in integrated CO_2 uptake and release in 1000× synthetic time series against seasonal amplitude estimates.

results of the MCS indicated a large mean -ve bias in the CO_2 DZCP trend (-0.57±4%), but also a large spread about the mean bias (r^2=0.35) which suggests that the CO_2 DZCP is more susceptible to aliasing. On the other hand, the use of $\Delta_t CO_2$=25% PU resulted in a relatively small mean bias (-14±2%) with high consistency (r^2=0.94). Although the mean bias was less in the MCS for the CO_2 UZCP (-1±3%), it was also marginally less consistent (r^2=0.80). The $\Delta_t CO_2$ UZCP had a mean bias of -23±1% (r^2=0.97). Differences between the spring and autumn phase biases calculated from CO_2 and $\Delta_t CO_2$ phase metrics carry through to the respective CUP estimates, where the CUP_Δ had a mean bias of -28±1% (r^2=0.93) relative to a bias of -55±1% (r^2=0.45) in the CO_2 CUP. Estimates of $\Delta_t CO_2$ phase metrics tended to be more consistent, and while it resulted in significantly more accurate estimates of the trend in spring phase, the autumn phase was better represented by the CO_2 UZCP. I expect that this is a result of the asymmetry of the high-latitude CO_2 seasonal cycle resulting in different aliasing effects on different aspects of the seasonal cycle. Analysis of peak rates of uptake and release resulted in mean biases of -18±2% and -28±2% for PU and PR respectively. In general, the trend estimates from the analysis had the correct sign so long as the trend was sufficiently large (>0.25%/yr for PU and PR, and >0.1 days/yr for changes in phase). The CO_2 phase metric trend estimates were the most likely to have the wrong sign compared to the $\Delta_t CO_2$ phase metrics by 4.5, 4 and 1.5× for the DZCP, UZCP and CUP respectively. The $\Delta_t CO_2$ metrics were far more effective at detecting statistically significant trends where the CO_2 metrics typically missed 33–50% of significant trends. Finally, Figure 2.15 shows a regression of the linear trend in integrated CO_2 uptake and release against the estimated seasonal amplitude, showing that the seasonal amplitude is highly correlated with variations in uptake during the CUP (r^2=0.73), but far less so with changes in carbon release during autumn (r^2=0.04).

The aim of these experiments was to quantify our ability to make accurate measurements of the seasonal cycle metrics in order to aid the interpretation of the trends observed in uptake and release of CO_2 in high-latitude CO_2 data. In the next section, I apply this analysis to the CO_2 data.

2.4 Atmospheric Transport Analysis

I use output from the GEOS-Chem simulation described in Section 2.2.2 to determine regional contributions to seasonal CO_2 variations. I sample CO_2 concentrations, tagged by region, at the nearest grid point to each of the northern hemisphere monitoring sites shown in Figure 2.1. I take the maximum contribution to the variation in CO_2 concentration from each region at each site and for each month, and take the zonal mean in 30° latitude bins. It should be noted that these calculations are dependent on both the ability of the model to reproduce atmospheric transport over the time span of the data, and the accuracy of the prior CO_2 fluxes used for the TransCom regions. Despite this, as I have averaged over multiple years and over zonal bands, I expect that they reasonably represent the large scale contributions caused by different regions. Figure 2.16 shows the maximum monthly and annual contributions to the CO_2 concentration arriving at each zonal band by biospheric carbon fluxes from 5 of the TransCom land regions, averaged over the period 2004-2009. This figure shows that the CO_2 seasonality in the high-latitude region is dominated by carbon fluxes from vegetation in boreal North America, Europe and Asia. Peak uptake in Europe, as seen in the high-latitudes, is reached up to a month earlier than in the other regions. As such, it may play a marginally more dominant role in determining the springtime onset of carbon uptake at some high-latitude sites, however this is relative to its smaller overall contribution to seasonal CO_2. As expected, the mid-latitude sites have a much larger relative contribution from temperate vegetation, although the effect of boreal vegetation on the seasonal cycle is still prominent. In the low latitudes it is clear that northern vegetation is still the primary driver of the seasonal cycle, with both temperate and boreal vegetation playing an important role. While tropical vegetation is a significant component of the natural carbon sink and therefore for determining the annual atmospheric growth rate of CO_2, it exhibits much lower seasonality when compared with vegetation in the mid and high-latitudes. For this reason, I do not consider seasonal contributions from tropical vegetation in this analysis.

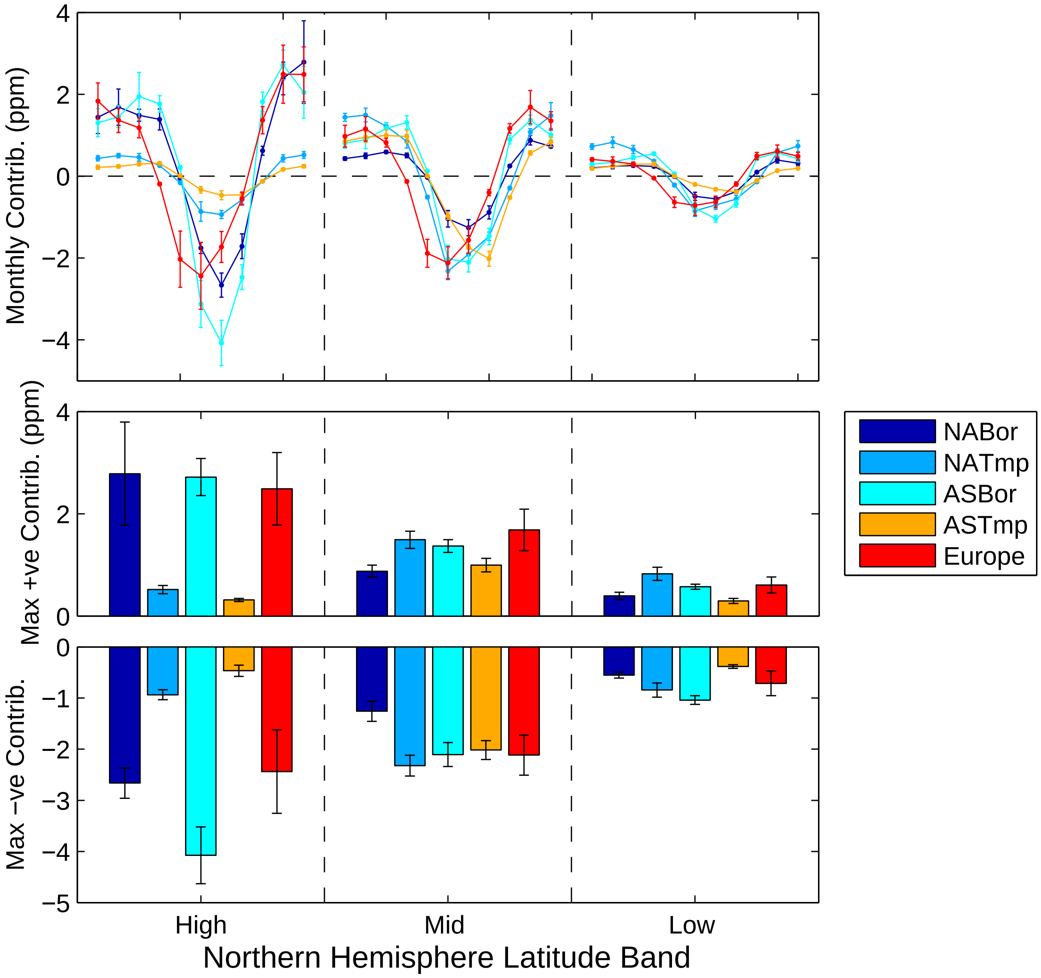

Figure 2.16: This figure shows the maximum CO_2 contributions caused by biosphere carbon fluxes from the TransCom land regions to the zonal mean concentrations in the high, mid, and low latitude northern hemisphere. These values were determined by using GEOS-Chem transport model output with prior fluxes on a 4°x5° horizonal grid from 2004-2009, where the error bars represent the 1σ of the year-to-year variability over this time period. The zonal means were defined as the mean of the grid points sampled nearest to the sites defined in Figure 2.1. The +ve perturbations are those caused by vegetative CO_2 sources, whereas the -ve perturbations are caused by sinks.

As the CO_2 concentration measured at a particular site is made up of flux contributions from different regions, interannual variability in the atmospheric transport and at different times of year could drive variability in the amplitude and phase of the seasonal cycle. Low and mid-latitude sites on average receive roughly equal contributions from temperature and boreal vegetation. In contrast, it can be seen that the high-latitude sites are overwhelmingly dominated by boreal vegetation, such that they are highly representative of the vegetation in the high-latitudes. In addition, the interannual variability of seasonal contributions indicated by the 1σ error bars, and resulting from interannual variations in atmospheric transport over the 5 year period, are relatively small ($<$0.5ppm). To determine the presence of any trends in the CO_2 seasonal cycle induced by long-term changes in atmospheric transport would require a control experiment using constant CO_2 emissions but variable transport over the time-span of the CO_2 data. The reliability of the results from such an experiment would be dependent on the ability to accurately constrain atmospheric transport over the past four or five decades.

2.5 Data Analysis

2.5.1 Growth Rates Analysis

I determined time series of annual growth rates for individual CO_2 sites (shown in Figure 2.1) using the method outlined in Section 2.3, before first calculating decadal mean growth rates, and second binning the decadal mean growth rates into 20° latitude bins. The subtracted decadal mean fossil fuel emissions are constant with latitude. Figure 2.17 shows how the decadal mean of the annual atmospheric growth rates have changed from 1980 to 2009 for individual sites and as a function of latitude. I find that in the 1980s and 1990s the growth rates are approximately the same in the southern hemisphere, but diverge further north. The 1980-1989 growth rate rises sharply towards the northern high-latitudes while there is a dip in the 1990-1999 in the same latitude band. I anticipate that this is partially due to the collapse of the Soviet Union but also due to changes in biospheric uptake in the northern hemisphere. It should be noted that the number of CO_2 monitoring sites in the 1980s is considerably more sparse. The 2000-2009 decadal mean growth rate is significantly higher than both of the previous decades by ~ 0.35 ppm/yr and rises from the southern hemisphere to mid-latitude northern hemisphere before dropping off again in the northern high-latitudes.

By subtracting anthropogenic fossil fuel emission estimates from the atmospheric CO_2 signal (see Table 2.2 for values) uptake from the ocean and terrestrial biosphere can effectively be isolated, acknowledging the uncertainties associated with the emission estimates and that I have not accounted for land use change emissions. The residual growth rate is negative, as expected. I find that during the 1980s the net uptake by the biosphere was typically -1.03 ± 0.11 ppm/yr. This

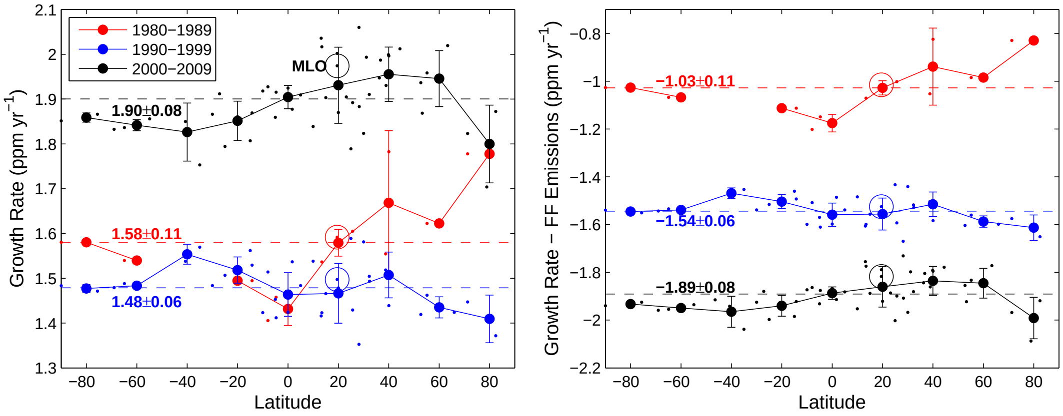

Figure 2.17: Decadal mean CO_2 growth rates inferred from measurements at individual sites and averaged in 20° latitude bins having retained (left) and subtracted (right) the decadal mean global fossil fuel emissions. The solid line with error bars represents the decadal mean growth rate in each latitude bin with $\pm 1\sigma$ representing the standard deviation between individual sites in that latitude bin. The global decadal mean growth rate is indicated by the dashed lines and mean values with $\pm 1\sigma$ representing the standard deviation between all sites. Values for Mauna Loa, which are typically taken to be representative of the global growth rate, are highlighted with a circle.

increases dramatically in the 1990s to approximately -1.54±0.06 ppm/yr and to -1.89±0.08 ppm/yr in 2000s. This supports the notion that the natural component of the carbon cycle is increasing the amount of carbon taken up in response to the amount of carbon emitted into the atmosphere, although the last two decades show a smaller increase in uptake. This apparent equilibrium state results in an approximate mean airborne fraction of 55.8±18.2% (including only fossil fuel) and 44.1±14.4% (including fossil fuel and land use change) which is consistent with existing analysis (Knorr, 2009; Le Quéré *et al.*, 2009; Gloor *et al.*, 2010).

Table 2.2: Decadal mean growth rates (ppm/yr)

Decade	No. Sites	Fossil Fuel (FF)	Growth Rate (GR)	GR 1σ	GR - FF
1960-1969	1	1.51	0.86	N/A	-0.65
1970-1979	2	2.25	1.21	0.055	-1.04
1980-1989	13	2.61	1.58	0.108	-1.03
1990-1999	38	3.02	1.48	0.056	-1.54
2000-2009	49	3.79	1.90	0.076	-1.89

2.5.2 Seasonal Cycle Analysis

Barrow, Alaska

I calculate changes in the seasonal cycle at BRW using the metrics defined in the previous section. Changes in the spring and autumn phase determined using the CO_2 and $\Delta_t CO_2$ metrics are shown in the left and right panels of Figure 2.18 respectively.

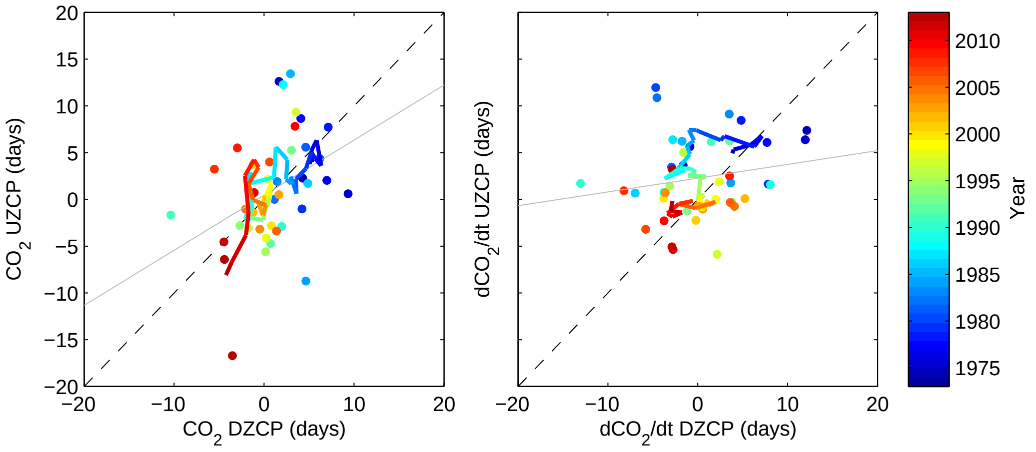

Figure 2.18: Scatterplot of spring (DZCP) and autumn (UZCP) phase calculated from BRW CO_2 (left panel) and $\Delta_t CO_2$ (right panel) time series respectively, where individual points are coloured according to the year of measurement (1973-2013).

The trends in CO_2 DZCP and UZCP at BRW are -0.20±0.08 days/yr ($p<0.01$)

and -0.18±0.14 days/yr ($p<0.05$), respectively, with a corresponding CUP change of 0.02±0.15 days/yr ($p>0.1$); The equivalent analysis using the $\Delta_t CO_2$ metrics shows changes in spring and autumn of -0.14±0.14 days/yr ($p<0.05$) and -0.25±0.08 days/yr ($p<0.01$) respectively with a change in CUP of -0.11±0.16 days/yr ($p>0.1$). Changes in the CUP length are not statistically significant in either case. The CO_2 phase metrics show a tighter coupling between the spring and autumn phases and a more conserved CUP. The $\Delta_t CO_2$ metric indicates a deviation to a slightly longer CUP throughout 1975-1990, however there is a negative linear trend in the CUP_Δ of -1.1±1.6 days/decade across the entire time series. This is a result of an earlier net release of carbon in autumn in comparison to the weaker trend in spring. In general, the CO_2 and $\Delta_t CO_2$ metrics attribute more variability to either autumn or spring phase changes respectively, but neither show a trend in the CUP.

The MCS indicated that phase trends needed a magnitude of >0.1 days/yr before high confidence could be given to the sign of the trend when assuming that interannual variability was ±10 days or less. In general interannual variability at BRW is <10 days, and the trends are sufficiently large (>0.1 days/yr) to give high confidence in the sign of the spring and autumn trends. The results of the MCS also suggested that the CO_2 DZCP was often underestimated compared to the expected change in spring phase, but this bias was not consistent across all of the synthetic time series. Infact, the trend in BRW spring phase determined from the CO_2 metric is larger in magnitude than the trend calculated from the $\Delta_t CO_2$ metric, which I estimated to have a smaller, yet more consistent bias. The general agreement of the trends determined from the CO_2 and $\Delta_t CO_2$ metrics for spring and autumn phase and their statistical significance gives high confidence that both have been advancing over the past 40 years. Given the large trends in spring and autumn phase over the span of the time series, it is remarkable that the CUP changes are so small.

My estimate of amplitude changes at BRW (0.09±0.02 ppm/yr) are consistent in percentage terms (∼0.62%/yr) with previous work (0.60%/yr, Graven *et al.* (2013)) who also showed that changes in atmospheric transport could only explain <7% of the amplitude variations. The seasonal amplitude which exhibits a consistent and almost linearly increasing trend suggests a larger exchange of carbon between vegetation and the atmosphere, however this does not appear to be a result of a change in the CUP as this has remained relatively constant over the past 40 years. I showed in Figure 2.15 that the seasonal amplitude is more highly correlated with changes in uptake during the CUP than changes in period of net carbon release. In addition, the increase in PR of 0.42±0.37 ppm/yr ($p<0.05$) is much smaller than the increase in PU of 0.65±0.34 ppm/yr ($p<0.01$) and the former is less statistically significant. I found in the MCS that changes in PU and PR must be >0.25%/yr assuming interannual variability of ±25%/yr to have confidence in the sign of the trend. This indicates that the PR observed at BRW is likely to be increasing, but significantly less so than the PU.

I analysed scenarios from the 1000 time series generated in the MCS which exhibited similar trend characteristics to those observed at BRW. These characteristics were as follows (1) CUP trend <0.15 days/yr, $p>0.1$ (2) PU trend, $p<0.01$ (3) PR trend, $p>0.1$ (4) PU trend > PR trend. There were only 14 time series which met these specifications, however, they all exhibited an increase in net uptake ranging from an additional 0.05-0.30 ppm/yr.

My analysis of BRW CO_2 suggests that the intensity of carbon uptake in summer has increased during the CUP. The trends in phase at either edge of the CUP appear to be robust, as both sets of phase metrics agree in sign, however there are some differences, where the $\Delta_t CO_2$ metric attributes a slightly greater trend to autumn, and the CO_2 metric attributes a slightly greater trend to spring. Piao *et al.* (2008) suggested that increased carbon losses in autumn resulting in a reduction of the CUP could result in a net source of CO_2 from northern vegetation. However, my analysis suggests that there is currently no robust evidence that there has been a trend in the CUP over the past 40 years.

Analysis of other high northern latitude sites

Table 2.3 shows the results of the linear regression analysis of CO_2 seasonal cycles from each of the high-latitude sites shown in Figure 2.1. The error characterisation of the seasonal cycle analysis was based on a 40 year time series based on the BRW CO_2 seasonal cycle. I therefore analysed these time series under the assumption that they typically exhibit a seasonal cycle of similar shape, phase and amplitude to the seasonal cycle observed at BRW. It should also be taken into account that each of these time series covers a different time span, which means that the magnitude of the linear regression coefficients is representative of different periods of time. In this discussion, I continue to use CO_2 DZCP and $\Delta_t CO_2$=25%PU as the operational spring phase metrics and CO_2 and $\Delta_t CO_2$ UZCPs as the autumn phase metrics.

I find that coefficients for the spring phase vary significantly depending on the site and between the CO_2 and $\Delta_t CO_2$ metric, however they are nearly all negative in sign. While most of the sites exhibit negative coefficients for the spring phase, the analysis of ICE shows a large positive coefficient for spring phase which is statistically significant for the CO_2 and $\Delta_t CO_2$ metrics. The remaining seasonal cycles exhibit a negative coefficient for spring phase ranging from zero (ZEP) to -0.4 days/yr (SHM). Other than BRW, only SHM has a statistically significant coefficient indicating the presence of a trend in the spring phase when using CO_2 and $\Delta_t CO_2$ phase metrics, while STM has a statistically significant trend when using the CO_2 metric.

Most sites also exhibit negative coefficients for autumn phase, where the only exceptions are the ZEP CO_2 UZCP and the ICE $\Delta_t CO_2$ UZCP. ALT, BRW, CBA and SHM each have statistically significant trends showing an advance of CO_2 UZCP where four sites have coefficients lying in the range of -0.24 and -0.27 days/yr.

The advances of spring and autumn phase is not entirely consistent between sites, as the magnitude varies significantly and few sites show statistically significant trends in spring phase and the $\Delta_t CO_2$ UZCP. ICE and ZEP show contradictory results in that they exhibit delays in the spring and autumn phases respectively. However, the differences in autumn and spring phases typically result in a CUP change which is not statistically significant. As this is consistent with my BRW analysis, this work provides strong evidence that the length of the high-latitude CUP had been roughly conserved over the past 40 years.

All sites exhibit significant increases in amplitude where the magnitude of increase differs from 0.05 to 0.14 ppm/yr where this range is likely to reflect differences in the time span of the data. Larger increases in PU than PR are seen at ALT, CBA and ZEP.

My analysis of CO_2 at other high-latitude sites emphasises the uniqueness of BRW in that almost every metric I used with the exception of PR and CUP exhibits a statistically significant trend. This may reflect the position of BRW with respect to boreal vegetation, however it is also likely that the longer time series at BRW increases the chance of detecting a long-term trend in data.

Site Info		**Spring Phase**				**Autumn Phase**				**Uptake Period**		**C. Exchange**		
Site	**Timespan**	**CO_2 DZCP (days/yr)**	**$\Delta_t CO_2$ DZCP (days/yr)**	**$\Delta_t CO_2$ = 25% PU (days/yr)**	**$\Delta_t CO_2$ = PU (days/yr)**	**CO_2 UZCP (days/yr)**	**$\Delta_t CO_2$ UZCP (days/yr)**	**$\Delta_t CO_2$ = 25% PR (days/yr)**	**$\Delta_t CO_2$ = PR (days/yr)**	**CO_2 CUP (days/yr)**	**$\Delta_t CO_2$ CUP (days/yr)**	**Seas. Amp. (ppm/yr)**	**PU (%/yr)**	**PR (%/yr)**
ALT	1986-2013	-0.14 ±0.15 ($p<0.1$)	-0.34 ±0.83 ($p>0.1$)	-0.16 ±0.26 ($p>0.1$)	-0.18 ±0.26 ($p>0.1$)	-0.27 ±0.19 ($p<0.01$)	-0.10 ±0.17 ($p>0.1$)	-0.09 ±0.20 ($p>0.1$)	0.15 ±0.59 ($p>0.1$)	-0.02 ±0.20 ($p>0.1$)	0.05 ±0.32 ($p>0.1$)	0.10 ±0.04 ($p<0.01$)	0.61 ±0.60 ($p<0.01$)	0.40 ±0.60 ($p<0.1$)
BRW	1973-2013	-0.20 ±0.08 ($p<0.01$)	-0.02 ±0.47 ($p>0.1$)	-0.14 ±0.14 ($p<0.05$)	-0.21 ±0.15 ($p<0.01$)	-0.18 ±0.14 ($p<0.05$)	-0.25 ±0.08 ($p<0.01$)	-0.26 ±0.10 ($p<0.01$)	-0.25 ±0.10 ($p<0.1$)	0.02 ±0.15 ($p>0.1$)	-0.11 ±0.16 ($p>0.1$)	0.09 ±0.02 ($p<0.01$)	0.65 ±0.34 ($p<0.01$)	0.42 ±0.34 ($p<0.05$)
CBA	1979-2012	-0.14 ±0.15 ($p<0.1$)	-0.56 ±0.34 ($p<0.01$)	0.06 ±0.11 ($p>0.1$)	-0.24 ±0.37 ($p>0.1$)	-0.27 ±0.27 ($p<0.05$)	-0.16 ±0.17 ($p<0.1$)	-0.17 ±0.20 ($p<0.1$)	0.14 ±0.33 ($p>0.1$)	-0.07 ±0.29 ($p>0.1$)	-0.22 ±0.34 ($p>0.1$)	0.07 ±0.04 ($p<0.01$)	0.66 ±0.48 ($p<0.01$)	0.58 ±0.48 ($p<0.05$)
ICE	1993-2013	0.34 ±0.27 ($p<0.05$)	0.62 ±0.98 ($p<0.01$)	0.63 ±0.65 ($p<0.01$)	0.25 ±0.54 ($p<0.1$)	-0.13 ±0.28 ($p>0.1$)	0.18 ±0.25 ($p>0.1$)	0.22 ±0.24 ($p<0.1$)	0.11 ±0.99 ($p>0.1$)	-0.21 ±0.33 ($p>0.1$)	-0.45 ±0.64 ($p>0.1$)	0.06 ±0.04 ($p<0.01$)	0.97 ±0.94 ($p<0.01$)	0.92 ±0.92 ($p<0.05$)
SHM	1987-2012	-0.40 ±0.18 ($p<0.01$)	-0.59 ±0.45 ($p<0.05$)	-0.45 ±0.34 ($p<0.05$)	-0.54 ±0.40 ($p<0.01$)	-0.27 ±0.22 ($p<0.05$)	-0.13 ±0.23 ($p>0.1$)	-0.11 ±0.25 ($p>0.1$)	-0.15 ±0.33 ($p>0.1$)	-0.13 ±0.24 ($p>0.1$)	0.32 ±0.44 ($p>0.1$)	0.06 ±0.05 ($p<0.05$)	-0.24 ±0.75 ($p>0.1$)	-0.05 ±0.69 ($p>0.1$)
STM	1981-2010	-0.17 ±0.14 ($p<0.05$)	-0.60 ±0.74 ($p>0.1$)	-0.03 ±0.65 ($p>0.1$)	-0.04 ±0.27 ($p>0.1$)	-0.24 ±0.25 ($p<0.1$)	-0.01 ±0.15 ($p>0.1$)	-0.01 ±0.18 ($p>0.1$)	0.16 ±0.62 ($p>0.1$)	-0.07 ±0.31 ($p>0.1$)	0.02 ±0.66 ($p>0.1$)	0.05 ±0.03 ($p<0.01$)	0.04 ±0.63 ($p>0.1$)	0.72 ±0.62 ($p<0.05$)
ZEP	1994-2013	-0.01 ±0.21 ($p>0.1$)	-1.24 ±1.78 ($p>0.1$)	0.01 ±0.61 ($p>0.1$)	-0.06 ±0.40 ($p>0.1$)	0.40 ±0.52 ($p>0.1$)	-0.16 ±0.33 ($p>0.1$)	-0.24 ±0.38 ($p>0.1$)	0.43 ±1.20 ($p>0.1$)	0.12 ±0.25 ($p>0.1$)	-0.18 ±0.76 ($p>0.1$)	0.14 ±0.05 ($p<0.01$)	1.00 ±1.06 ($p<0.05$)	-0.30 ±1.07 ($p>0.1$)

Table 2.3: Estimated trends of downward and upward zero crossing points (DZCP and UZCP, respectively), peak uptake and release (PU and PR, respectively), and carbon uptake period (CUP) calculated from CO_2 and $\Delta_t CO_2$ data for seven high latitude measurement sites (Figure 2.1). The 95% confidence intervals and p-values are calculated for each trend estimate.

2.6 Analysis of Ancillary Data

2.6.1 Surface Temperature Analyses

Table 2.4 shows results from the linear trend analysis of temperature and the TGS as determined from surface land temperatures averaged over northern hemisphere TransCom regions, where all trends are highly statistically significant ($p<0.01$). The analysis shows that temperatures have warmed significantly at high-latitudes since 1970. I find that an earlier onset of the mean temperature reaching 5°C in spring, TGS_{BEG} and a delay in the temperature dropping below 5°C in autumn, TGS_{END} results in a significant lengthening of the thermal growing season, TGS_{LEN} since 1970 for a number of high-latitude regions. Of the TransCom regions, I find that Europe exhibits the largest change in TGS_{LEN} of $\sim$3.41±0.9 days/decade, a result of equal shifts in TGS_{BEG} and TGS_{END}. Europe is followed by roughly equal changes in Boreal North America and Asia, however these regions exhibit different changes in spring and autumn temperature. The largest overall changes are seen >60°N where TGS_{LEN} has increased by up to 5±1.7 days/decade where a larger proportion of this change is due to autumn warming. This increase in TGS_{LEN} suggests that the potential period during which plant growth is not hindered by low temperatures has been significantly extended by approximately 11 days (>45°N) and 20 days (>60°N) since 1970, consistent with previous findings (Linderholm, 2006; Barichivich *et al.*, 2012).

Table 2.5 shows the relationship between TGS_{BEG}, TGS_{END} and TGS_{LEN} determined from northern high-latitude land surface temperature anomalies

Table 2.4: Temperature linear trend analysis (1970-2011)

	TGS$_{BEG}$ (Days/decade)				Spring T (°C/decade)			
Region	Trend	unc	r^2	p-value	Trend	unc	r^2	p-value
ASBor	-1.39	±0.49	0.45	<0.01	0.58	0.27	0.32	$p<0.01$
Europe	-1.67	±0.52	0.51	<0.01	0.33	0.11	0.47	$p<0.01$
USBor	-1.06	±0.72	0.18	<0.01	0.34	0.25	0.15	$p<0.05$
>45° N	-1.24	±0.44	0.44	<0.01	0.41	0.13	0.49	$p<0.01$
>60° N	-2.12	±0.75	0.45	<0.01	0.45	0.18	0.40	$p<0.01$

	TGS$_{END}$				Autumn T			
Region	Trend	unc	r^2	p-value				
ASBor	1.07	±0.79	0.16	<0.01	0.57	0.29	0.28	$p<0.01$
Europe	1.74	±0.66	0.42	<0.01	0.38	0.12	0.49	$p<0.01$
USBor	1.57	±0.69	0.35	<0.01	0.47	0.21	0.34	$p<0.01$
>45° N	1.34	±0.47	0.45	<0.01	0.44	0.13	0.55	$p<0.01$
>60° N	2.85	±1.04	0.43	<0.01	0.52	0.16	0.53	$p<0.01$

	TGS$_{LEN}$				Annual T			
Region	Trend	unc	r^2	p-value				
ASBor	2.46	±1.08	0.35	<0.01	0.45	0.16	0.45	$p<0.01$
Europe	3.41	±0.90	0.60	<0.01	0.35	0.10	0.61	$p<0.01$
USBor	2.63	±1.25	0.31	<0.01	0.43	0.16	0.41	$p<0.01$
>45° N	2.57	±0.78	0.52	<0.01	0.40	0.10	0.67	$p<0.01$
>60° N	4.97	±1.69	0.47	<0.01	0.43	0.11	0.63	$p<0.01$

>45°N and >60° with the BRW CO_2 and $\Delta_t CO_2$ phase metrics throughout 1973-2011 respectively, where the individual time series are shown in Figure 2.19. The autumn phase metrics for CO_2 and $\Delta_t CO_2$ are anti-correlated with TGS_{END} indicating that autumn carbon release has increased while temperatures have risen in autumn. The spring phase is positively correlated indicating that carbon uptake has increased as temperature has risen in spring. If spring and autumn temperature variations could account for 100% of changes in carbon uptake in spring and autumn, the expected regression coefficients for CO_2 and $\Delta_t CO_2$ would be roughly equal to one. This is the case for the CO_2 DZCP and the

CO_2			
	DZCP vs. TGS$_{BEG}$	**UZCP vs. TGS$_{END}$**	**CUP vs. TGS$_{LEN}$**
>45°N	1.02±0.47 (r^2=34, $p<0.01$)	-0.13±0.73 (r^2=0.01, $p>0.1$)	0.31±0.44 (r^2=0.04, $p>0.1$)
>60°N	0.63±0.27 (r^2=0.38, $p<0.01$)	-0.11±0.34 (r^2=0.01, $p>0.1$)	0.14±0.22 (r^2=0.04, $p>0.1$)
$\Delta_t CO_2$			
	DZCP vs. TGS$_{BEG}$	**UZCP vs. TGS$_{END}$**	**CUP vs. TGS$_{LEN}$**
>45°N	0.57±0.81 (r^2=0.05, $p>0.1$)	-0.89±0.51 (r^2=0.25, $p<0.01$)	-0.42±0.48 (r^2=0.08, $p<0.1$)
>60°N	0.28±0.48 (r^2=0.04, $p>0.1$)	-0.42±0.24 (r^2=0.26, $p<0.01$)	-0.19±0.24 (r^2=0.07, $p<0.1$)

Table 2.5: Regression coefficients between CO_2, $\Delta_t CO_2$ and temperature phase metrics (1973-2012).

$\Delta_t CO_2$ UZCP which both have statistically significant relationships ($p<0.01$) with TGS$_{BEG}$ and TGS$_{END}$ respectively when compared with temperature anomalies >45°N. However both metrics show either a weak correlation in spring phase or a weak correlation in autumn phase, and all CO_2 metrics are smaller than the temperature trend >60°. The low correlation between the CO_2 CUP and CUP$_\Delta$ reflects that the CUP has not extended despite a significantly longer period of potential plant productivity.

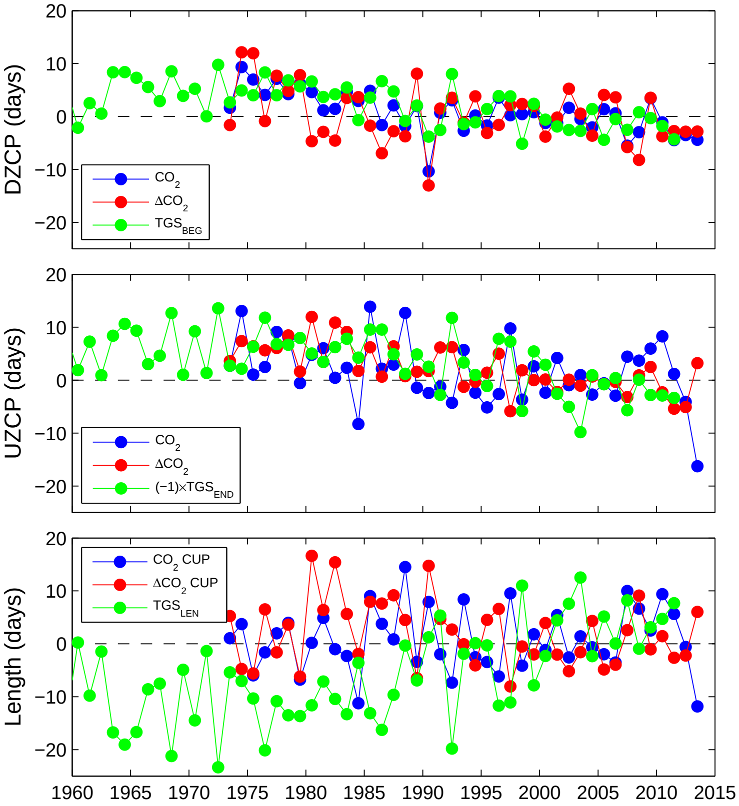

Figure 2.19: Phase anomalies for CO$_2$, Δ_tCO$_2$ and >60°N TGS. Regression coefficients and stats are shown in Table 2.5.

2.6.2 δ^{13}C Isotope Measurements

As the seasonality of δ^{13}C is anti-correlated with CO_2, I perform the same phase analysis on (-1)×δ^{13}C and (-1)×$\Delta_t\delta^{13}$C to determine annual time series of δ^{13}C phase changes. I compare the variability and trends of the CO_2 and δ^{13}C phase changes using RMA. RMA accounts for there being errors in both regression variables, where the errors are related to each other. In this case, the errors are related because the phase metrics are derived from measurements of δ^{13}C and CO_2 which are obtained from the same flask samples. The phase time series determined from CO_2 and δ^{13}C are shown in Figure 2.20.

Table 2.6 shows the RMA regression coefficients and stats for the spring and autumn phase and the CUP. If the trend in biospheric uptake was perfectly represented by δ^{13}C and the trend in CO_2 was caused entirely by changes in the biosphere, the expected regression coefficients would be equal to one. Indeed, many of the regression coefficients are close to a value of one, the coefficients are much larger than the uncertainties, the time series are highly correlated, and they each exhibit a highly statistically significant relationship ($p<0.01$). The CO_2 seasonal signal measured at BRW, while mostly being driven by boreal vegetation is also subject to variability in atmospheric transport and minor contributions from other CO_2 sources and sinks that are difficult to separate from the seasonal signal. As the CO_2 and δ^{13}C values are retrieved from the same flask samples, this means that the trends are primarily either a result of CO_2 and δ^{13}C transported from elsewhere, or changes biospheric fluxes. However Graven *et al.* (2013) found in a study of northern hemisphere seasonal amplitude changes that atmospheric transport was a larger contributor in the lower latitudes, and that its magnitude was 7% or less at all locations, subject to errors in model transport. It therefore appears that much of the variability in phase, at least 80% of the spring and autumn phases, are likely driven by changes in carbon exchange by the terrestrial biosphere. The CO_2 vs. $\delta^{13}C$ regression shows a similar pattern to the temperature regression analysis, in that the CO_2 spring phase and $\Delta_t CO_2$ autumn phase are the most highly correlated with the isotope record. The CO_2 and $\delta^{13}CO_2$ CUP changes are also highly correlated.

	DZCP	**UZCP**	**CUP**
CO_2 vs. $\delta^{13}C$	0.97±0.18 ($r^2=0.91$, $p<0.01$)	1.04±0.37 ($r^2=0.61$, $p<0.01$)	0.99±0.36 ($r^2=0.58$, $p<0.01$)
$\Delta_t CO_2$ vs. $\Delta_t \delta^{13}C$	0.95±0.33 ($r^2=0.64$, $p<0.01$)	0.87±0.22 ($r^2=0.83$, $p<0.01$)	0.79±0.26 ($r^2=0.69$, $p<0.01$)

Table 2.6: Regression coefficients comparing changes in CO_2 against changes in $\delta^{13}C$ at BRW during the overlapping time span of the data (1990–2012).

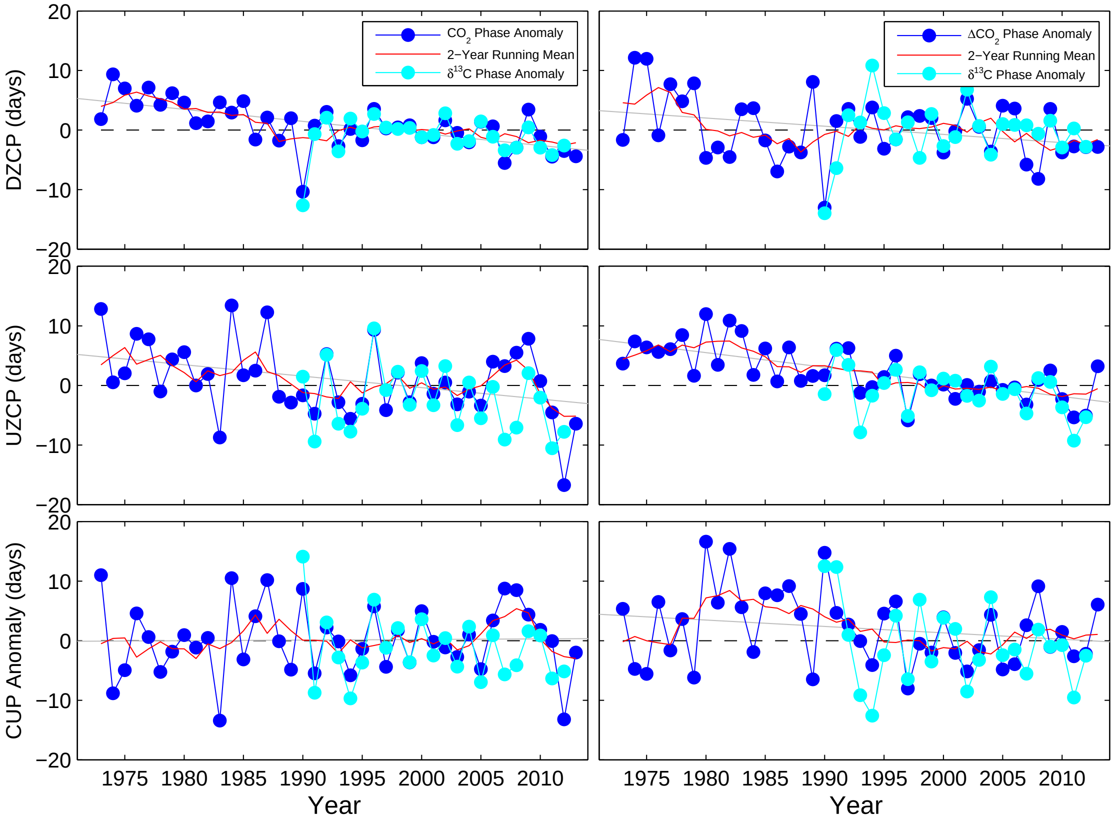

Figure 2.20: Comparison of phase time series determined from the CO_2 and $\Delta_t CO_2$ seasonal cycles and the equivalent values calculated from δ^{13}C ratios.

2.7 Summary

Changes in the functioning of terrestrial ecosystems represent a substantial climate feedback, but current understanding precludes our identification and protection of the responsible geographic regions. My results provide evidence of substantial changes in carbon uptake and release by northern high-latitude ecosystems.

I used the wavelet transform to spectrally decompose CO_2 mole fraction data into a trend component and a seasonal cycle. I compared growth rates determined from the trend component at Mauna Loa with NOAA/ESRL values and found differences of <0.1 ppm/yr. I found that global atmospheric growth rates exhibit large decadal changes, and once the anthropogenic signal has been removed, I find strong evidence that the natural signal corresponding to oceanic and biospheric sinks has responded to increasing atmospheric CO_2 concentrations. This has resulted in a near-constant airborne CO_2 fraction of 55.8 ± 18.2 % (including only fossil fuel emissions) and 44.1 ± 14.4 % (including fossil fuel and land use change emissions).

I used numerical Monte Carlo experiments to characterize the aliasing errors associated with independently identifying changes in phase and amplitude of the detrended CO_2 seasonal cycle that can otherwise lead to the misinterpretation of the data; these errors are not unique to the wavelet transform. For example, I show that a realistic trend in the downward, spring phase can be misinterpreted as changes in the downward and upward phase and in the peak uptake and release of CO_2.

Statistical analysis from the Monte Carlo simulation generally indicated that use of the first derivative of the CO_2 mole fraction produces more reliable and less biased estimates for the changes in either phase with an estimated 25% aliasing error. I also found that the wavelet transform can capture at least 80% of independent changes in the peak and trough of the seasonal cycle, which has not been reported previously and allows us to study changes in characteristics more closely related to annual changes in biological release and uptake of CO_2.

My data analysis was predominantly focused on the BRW site in Alaska as this site has the longest time series of atmospheric CO_2 in the high-latitude northern hemisphere, but is also highly representative of boreal carbon fluxes. I found advances in both the spring and autumn phases of the seasonal cycle indicating an earlier onset of net carbon uptake in spring and an earlier onset of net carbon release in autumn. Changes in the spring and autumn phase are supported by concomitant changes in the $\delta^{13}C$ records supporting the idea that at least 80% of the observed phase variations are due to the terrestrial biosphere. Analysis of surface temperature analyses also support this result, although I find that the start of the thermal growing season (defined as the continuous period above 5°C) is advancing two (three) times faster at latitudes >45°N (>60°N). In contrast, the CO_2 autumn phase is anti-correlated with the end of the thermal growing season and tracks it more closely. PU was found to be increasing at a greater rate than PR, which along with the increase in seasonal amplitude, indicates that uptake during the CUP is likely to be increasing. Statistical analysis indicated that the trends in the high-latitude seasonal cycle are consistent with an increase in net uptake by boreal vegetation. However, our understanding of the processes underlying the changes at the edges of the CUP need to be improved.

My analysis here does not provide direct evidence about the balance between uptake and release of carbon, but changes in the peak uptake and release together with an invariant carbon uptake period provides indirect evidence that high northern latitude ecosystems are progressively taking up more carbon. Changes in the atmospheric CO_2 mole fraction only tell us part of the underlying carbon cycle story in terms of how the underlying ecosystems are changing. Clearly, additional measurements and models need to be applied to better understand these observed changes. A more frequent inspection of these data using advanced statistical tools such as the wavelet transform is likely to have a role to play.

Chapter 3

Are high latitude CH_4 emissions increasing? An analysis of surface CH_4 mole fraction data

3.1 Introduction

Methane is the second most important greenhouse gas after carbon dioxide. Although CH_4 has a much shorter atmospheric lifetime (<10 years) than CO_2, it has a much higher radiative forcing on a per molar basis, such that additional release of CH_4 is particularly important over short durations. The concentration of CH_4 has more than doubled since pre-industrial times. However the atmospheric growth rate of CH_4 which has been positive throughout much of the twentieth century, slowed towards the end of the 1990's, reaching a relatively stable state (Dlugokencky *et al.*, 1998) before continuing to increase again in 2007 (Rigby *et al.*, 2008; Dlugokencky *et al.*, 2009). There are a large number of sources of CH_4 to the atmosphere, the largest being wetlands and rice paddies, but the recent changes in the atmospheric growth rate are still poorly understood. Our need to increase the effectiveness of emission reduction schemes and detect feedbacks to climate change depends on our ability to quantify CH_4 emissions at regional scales. The purpose of this chapter is to determine whether an increase in the emissions of CH_4 from high-latitude wetland sources can be detected in atmospheric concentration data by looking at changes in the seasonal cycle amplitude. In particular, I focus on using changes in the amplitude of the CH_4 seasonal cycle for the detection of large-scale change. Measurements of the CH_4 concentration at any particular site contains contributions from different local and non-local sources and sinks. This makes interpretation of the data particularly difficult. High-latitude sites are likely to be the most sensitive to changes in wetland emissions and use of concentration data means that long time series can be utilised for trend analysis.

Arctic permafrost is a particularly vulnerable source of CH_4 to the atmosphere. Large amounts of organic carbon is stored within Arctic permafrost (Ping *et al.*, 2008; Tarnocai *et al.*, 2009) and in CH_4 hydrates beneath subterranean and submerged permafrost (Corell *et al.*, 2008). McGuire *et al.* (2009) estimated that the amount of CH_4 stored as gas hydrate in the Arctic is likely to range between 35 and 365 Pg CH_4. When the frozen soils in land-based permafrost layers thaw, the organic carbon stored within becomes exposed to microbial decomposition releasing it into the atmosphere.

Current CH_4 fluxes from the Arctic are currently considered relatively small from a global perspective. A recent review of the Arctic carbon cycle by McGuire *et al.* (2012) found that most estimates lie within the range of 8-29 $TgCH_4$/yr. The vast stores of carbon in the region are vulnerable to the unprecedented rises in temperature that have been observed in the Arctic (Overland *et al.*, 2008), especially as much of the warming is occurring near to the surface (Screen and Simmonds, 2010). It has been determined that while methanogenesis is sensitive to a number of environmental variables (primarily soil temperature, labile carbon availability and the depth of the water table), soil temperature is the dominant factor in determining emissions on an annual basis (Zhuang *et al.*, 2007). Therefore these stores are a significant cause for concern due to the potency of CH_4 as a greenhouse gas, with the possibility of strong climate-feedbacks as a consequence of its release into the atmosphere. As most hydrates are stored at considerable depth, most modelling studies have suggested that the climate-CH_4 feedback from high-latitude wetlands and permafrost is unlikely to be catastrophic, but will occur in the form of sustained CH_4 release over the next few decades (Archer, 2007). Gedney *et al.* (2004) and Zhuang *et al.* (2006) both estimate a doubling of Arctic CH_4 emissions by 2100 under high anthropogenic emissions scenarios.

Current estimates of Arctic CH_4 emissions have been determined independently using direct flux observations, process-based models, and atmospheric inversions in conjunction with surface CH_4 concentration measurements. Flux observation studies have been of great use in understanding surface processes affecting the strength of CH_4 emissions during summer and autumn. However these studies tend to be short, perhaps one or two years, and are typically representative of reasonably local areas (which are subsequently scaled up). The spatio-temporal discontinuities inherent across the range of flux observations and the range of instruments each with their own uncertainty ranges means that it has been difficult to quantify the decadal trend in emissions. CH_4 emissions from wetlands are difficult to quantify using assimilation systems for two reasons: poor or inaccurate knowledge of their global distribution, and large variability in emission rates over small spatial scales making it difficult to upscale to larger spatial scales.

Some studies have recorded large, short-term increases in CH_4 flux from the Arctic, highlighting the sensitivity of emissions to even small amounts of warming. For example, Bloom *et al.* (2010) found increases in Arctic wetland emissions (>67°N) of 30.6±0.9% in the period 2003-2007 using data from SCIAMACHY, and that these changes were highly correlated with surface temperature. Again these short term datasets do not give us much information about long-term trends in Arctic CH_4 emissions.

It has been argued that if there had been a large-scale increase in surface emissions of CH_4 as a result of recent Arctic warming, that we should be able to see it in atmospheric measurements of CH_4, for example from the NOAA/ESRL CGASN. The numerous high-latitude measurement sites, some of which have been running for up to 30 years, provide a long-term picture of the growth rate and seasonality of surface CH_4 concentrations. These measurements contain information about local surface fluxes, and fluxes from other parts of the world as a result of atmospheric mixing. ACTMs are typically used to disentangle such signals, where inversion studies produce emission estimates of CH_4 from different regions. Previous studies have shown that the network has a sensitivity of at least $3TgCH_4/yr$ (Dlugokencky *et al.*, 2003). Despite this, there has been no evidence using concentration data that has shown a significant *decadal* increase in Arctic wetland emissions. This could either be because there is simply no long-term trend in emissions, that the trend is too small to detect over factors such as variations in atmospheric transport, or because the measurement network is not sensitive enough to detect changing emissions in the Arctic.

In this chapter, I use a simple approach to investigate long-term changes in the seasonality of high-latitude CH_4 concentrations. I focus my analysis on CH_4 concentrations measured at the site of Barrow in northern Alaska. Analysis of CH_4 at this site is beneficial for a number of reasons: (1) it has the longest CH_4

concentration time series of all of the high latitude sites (2) it is host to a number of measurement programs, including in situ and discrete CH_4 flask measurements and measurements of the isotope ratio δ^{13}C-CH_4 and (3) it is in close proximity to large areas of natural wetlands. First I use in situ measurements of BRW CH_4, filtered using local meteorological fields, to estimate changes in summer CH_4 anomalies at a local scale, making a comparison with local variations in temperature. Second, I spectrally decompose CH_4 flask time series measured at numerous high-latitude sites to quantify variability and trends in the seasonal amplitude. Wetland emissions typically peak in late summer/early autumn, which roughly coincides with the seasonal minima of the high-latitude CH_4 concentration. Next, I test the hypothesis that increased high-latitude wetland emissions could reduce the seasonal amplitude of CH_4 by "filling" in part of this minima. I use an atmospheric transport model to interpret the observed variability and trends in CH_4, with a focus on the contribution from transport variability and Arctic wetland emissions.

3.2 Data and Methods

3.2.1 Data

In situ CH_4

To estimate local CH_4 summer anomalies on the Alaska North Slope, I use hourly averaged in situ CH_4 measurements at Barrow, Alaska (BRW) provided by the NOAA/ESRL CGASN. These measurements are made using a gas chromatograph designed specifically for analysis of ambient levels of CH_4, CO (carbon monoxide) and CO_2. The precision of a single CH_4 measurement is estimated to be approximately 0.2%, the standard deviation (1σ) of 20 measurements of standard gas (Dlugokencky *et al.*, 1995). Measurements made when the analytical instrument was not working properly are first removed using a rule-based editing algorithm (Masarie *et al.*, 1991). Hourly averages were calculated from 2-3 individual measurements per hour from 1986-1996 and 4 measurements per hour from 1996 to the present day.

Flask CH_4

I use weekly values and monthly averages of CH_4 from flask measurements at a number of high-latitude sites shown in Figure 3.2 from the NOAA/ESRL CGASN. Air samples (flask) are collected at the sites and analysed for CH_4 at NOAA/ESRL in Boulder, Colorado by the NOAA/ESRL GMD using a gas chromatograph with flame ionization detection. Each sample aliquot is referenced to the NOAA 2004 CH_4 standard scale (Dlugokencky *et al.*, 2005). Individual measurement uncertainties are calculated based on analytical repeatability and the ability to propagate the World Meteorological Organization (WMO) CH_4 mole fraction standard scale. Analytical repeatability has varied between 0.8 and 2.3 ppb, but averaged over the measurement record is approximately 2 ppb. Propagation of the scale is based on a comparison of flask and in situ measurements at the MLO and BRW observatories and has a fixed value 0.7 ppb. These two values are added in quadrature (square root of the sum of the squares) to estimate the total measurement uncertainty, equivalent to a ~68% confidence interval.

These monitoring sites usually collect at least one CH_4 sample per week, and thus it is suitable to use weekly values or monthly averages for the analysis. As there are data gaps in the weekly time series and we need a continuous time series with a constant time step to use the wavelet decomposition technique, it is necessary to impute missing data points in the time series. Initially I subtract the long-term trend from a reference time series which is representative of the latitude band, in this case BRW. I then calculate a locally averaged in time seasonal cycle and

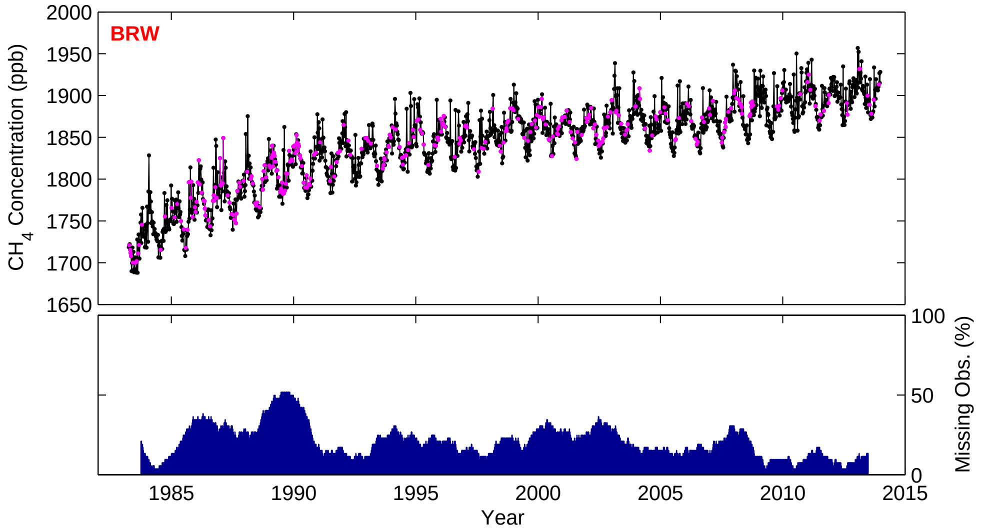

Figure 3.1: Discrete CH_4 flask data at BRW (black) where magenta points are those which have been interpolated. The lower panel shows the number of missing weekly observations across the time series in a running window of 52 weeks.

extract the missing value from this seasonal cycle before adding the trend value from the reference time series. This method ensures that imputed data points are weighted by variability in the actual data under the assumption that the atmospheric growth rate at any particular site is similar to BRW. Any remaining missing data points are extracted from a piecewise cubic spline curve fit. Parts of the time series which contain significant sections of missing data are likely to exhibit unreliable interannual variations - this is especially the case because the CH_4 time series are noisy. However missing sections are unusual and I find that isolated missing data points do not significantly impact the determination of long-term trends.

Figure 3.1 shows the discrete CH_4 flask measurements at BRW and data points that I have imputed, where the lower panel shows the % of measurements missing in any 52 week period. It can be seen that the first 5-6 years has the largest proportion of missing data but in general there is <25% missing data points and they tend to be sporadic rather than consecutive. The earliest years of the BRW time series are likely to be the most unreliable.

Marine Boundary Layer Reference CH_4 (MBL)

The NOAA/ESRL CO_2 MBL is a data product showing the evolution of CH_4 concentration by latitude over time. The MBL is based on measurements from the CGASN. The sites which are included are those at remote marine sea level locations with prevailing onshore winds such that they pick up well-mixed marine boundary layer air that is representative of large volumes of the atmosphere. These data are smoothed in time (Thoning and Tans, 1989), temporal gaps in the data are filled using a data-based extension methodology (Masarie and Tans, 1995), and latitudinal smoothing is also applied by fitting curves to each weekly latitudinal distribution, where sites exhibiting higher signal-to-noise and more consistent sampling have greater weighting (Tans *et al.*, 1989). The MBL reference surface is a 2-dimensional matrix composed of weekly CH_4 concentrations from 1984-2012 at intervals of 0.05 sine of latitude from 90°S to 90°N. I also use zonal-averages of CH_4 from the MBL, namely the Polar Northern Hemisphere (PNH) mean.

CH_4 Isotope Record ($\delta^{13}C$-CH_4)

I also use weekly measurements of the stable isotopic composition (^{13}C) of atmospheric CH_4, $\delta^{13}C$-CH_4 (White and Vaughn, 2011b). The isotope samples are analysed at CU-INSTAAR where precision is estimated to be approximately 0.06 permil for $\delta^{13}C$-CH_4. The $\delta^{13}C$-CH_4 ratios at ALT and BRW cover the time spans of 1990-2012 and 1998-2012 respectively, and are the only high-latitude records with a time span of >10 years. The isotope ratios are derived from the same flasks of air used to measure the quantity of CH_4. The δ notation refers to the ratio of minor to major isotopes relative to a standard:

$$\delta^{13}C_{sample} = \left[\frac{(^{13}C/^{12}C)_{sample}}{(^{13}C/^{12}C)_{std}} - 1\right] \times 1000 \tag{3.1}$$

and is expressed in units of 'permil' (parts per thousand).

I use the Keeling plot approach outlined in Pataki *et al.* (2003) to assess bulk inputs of CH_4 into Arctic air. This involves using RMA regression to find the intercept of δ^{13}C-CH_4 and $1/CH_4$, a value which can be associated with the CH_4 source. Method I (standard linear) regression is not appropriate because it assumes that there is no error associated with the dependent variable, δ^{13}C-CH_4, and that the errors in the two variables are unrelated. This is not the case, as errors are likely to be present in both δ^{13}C and CH_4 and they are related because one is present in the other. I use a running window of 9 weeks across the $1/CH_4$ and δ^{13}C-CH_4 time series and produce a Keeling plot, calculating the intersect for each window, assuming that the window has at least 5 coinciding measurements. The geometric mean regression provides the intersect and 95% confidence interval for each Keeling plot. I also calculate the mean intersect by season for each year. The three primary classes of CH_4 have distinct isotopic signatures, δ^{13}C≈-60‰ for bacterial CH_4, δ^{13}C≈-40‰ for thermogenic CH_4 and δ^{13}C≈-20‰ for biomass burning CH_4 (Quay *et al.*, 1991). While individual sources of CH_4 are likely to be significantly different from the source type's characteristic signature, the average values are likely to be valid for large spatial scales (Conny and Currie, 1996).

Meteorological Data

For the analysis of BRW insitu hourly mean CH_4 I use local meteorological data from the site of BRW. This includes hourly mean time series of wind speed and wind direction which are used to separate the measurements of CH_4 into air sectors. I use hourly averages of the two metre temperature for comparison with CH_4 emission estimates.

Other Data

I compare trends and interannual variability of CH_4 with gridded temperature (resolution of 1 degree latitude × 2/3 degrees longitude) from the Global Modelling and Assimilation Office (GMAO) Modern Era-Retrospective Analysis for Research and Applications (MERRA) dataset (Rienecker *et al.*, 2011). MERRA covers the time span of modern era remotely sensed data (1979-present), and also overlaps with the period of consistent ground-based observations of surface CH_4 concentrations from NOAA/ESRL CGASN. I sample gridded surface temperatures over areas of Eurasian and North American permafrost affected wetlands (see Figure 3.2) and build up time series of growing season temperature anomalies and potential growing season length (where the potential growing period is defined as days$>0°$) for each region. The permafrost affected wetland map is based on a reclassification of the FAO-UNESCO soil map of the world, combined with a soil climate map from USDA-NRCS.

3.2.2 Wavelet Transform

I use the wavelet transform to decompose the CH_4 time series into a wavelet coefficient matrix, which shows the power of different frequencies contained within the data and how they evolve with time. I use this method with the Morlet wavelet to spectrally filter CH_4 time series, to separate the seasonal variability and long-term trend, and also to remove high frequency noise. In general I remove high

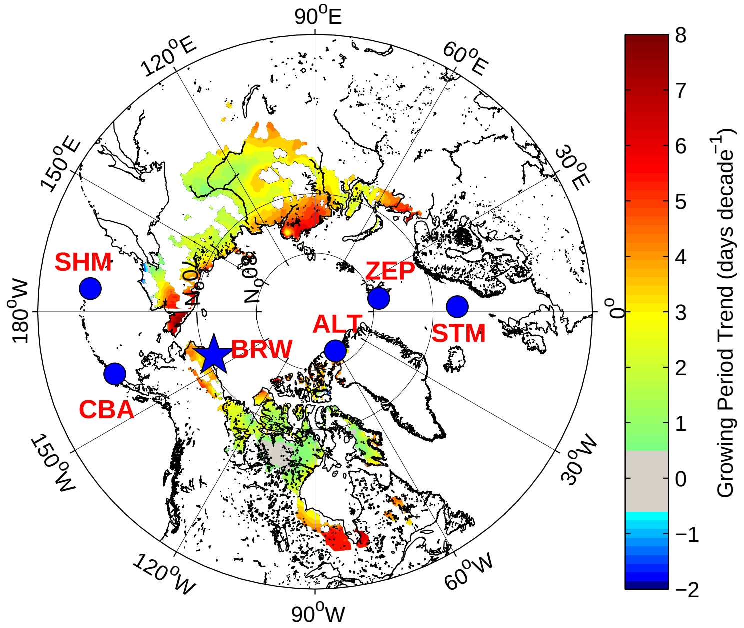

Figure 3.2: Map of the polar northern hemisphere. Decadal trends in potential period of thaw (days >0°C) over the period 1979-2012 are imposed over permafrost affected wetland regions as calculated from the MERRA reanalysis dataset (Rienecker *et al.*, 2011). Decadal trends <0.5 days/decade are shown in grey. The NOAA/ESRL CH_4 flask sites used in the analysis are shown by the blue markers, where sites with a blue star also have an in situ measurement program. Monitoring sites are as follows: Alert, Nunavut, Canada (ALT - 62.51°W, 82.45°N), Barrow, Alaska (BRW - 156.61°W, 71.32°W), Cold Bay, Alaska (CBA - 162.72°W, 55.21°N), Storhofdi, Vestmannaeyjar, Iceland (ICE - 20.29°W, 63.40°N), Shemya Island, Alaska (SHM - 174.13°E, 52.71°N), Ocean Station M, Norway (STM - 2.00°E, 66.00°N), Ny-Alesund, Svalbard, Norway (ZEP - 11.89°E, 78.91°N).

frequency variations (<2 months) and retain a sub-annual frequency (<7 months), an annual frequency (<18 months), and a trend component (>18 months).

3.2.3 TM5 Atmospheric Transport Model

Model Description

To help interpret the trends in Arctic CH_4 concentrations, I use model output from Transport Model 5 (TM5, Krol *et al.* (2005)), firstly to determine trend contribution from atmospheric transport and second, to simulate the effect of increased Arctic wetland emissions to the CH_4 concentrations observed by high-latitude monitoring sites. The TM5 model simulations used in this study were provided by Lori Bruhwiler from the Carbon Cycle Greenhouse Gases Group within the NOAA GMD in Boulder, Colorado (Bruhwiler *et al.*, 2014). TM5 is developed and maintained jointly by the Institute for Marine and Atmospheric Research Utrecht (IMAU, the Netherlands), the Joint Research Centre (JRC, Italy), the Royal Netherlands Meteorological Institute (KNMI, the Netherlands), NOAA and ESRL. The inputs of TM5 are 3D meteorological fields and best guess regional estimates of CH_4 sources and sinks (priors), including loss processes of CH_4 (e.g. by reaction with OH) in the atmosphere. The output of the model is a gridded 3D field of CH_4 concentration throughout the period 1989-2010. In this case, the winds used for transport in the TM5 simulations come from the European Centre for Medium range Weather Forecast (ECMWF) operational forecast model. The TM5 simulations have a horizontal resolution of $4°$ latitude $\times$ $6°$ longitude and a vertical resolution of 34 hybrid sigma-pressure levels (from 2006 onwards; 25 levels previously).

Prior Emission Estimates

The prior flux estimates used for wetlands are from Bergamaschi *et al.* (2005). Wetlands are the largest natural source of CH_4, and occur in regions that are permanently or seasonally water logged, a broad category including high-latitude bogs and tropical swamps. The prior flux estimates of Bergamaschi *et al.* (2005)

are based on wetland distribution of Matthews (1989) and wetland emission model of Kaplan (2002) which parameterizes emissions based on moisture, temperature and soil carbon. Arctic wetland emissions are symmetric across the growing season, peaking in mid-summer. Other prior emissions include fossil fuel, agriculture and waste (EDGAR 3.2FT2000, European Commission (2009)), biomass burning (Global Fire Emissions Database), and atmospheric chemical loss. Atmospheric chemical loss from the reaction with OH is the primary mechanism by which CH_4 is removed from the atmosphere. This reaction roughly balances the total atmospheric input of CH_4 from sources, however small differences lead to trends in the atmospheric abundance of CH_4 as have been observed in recent years. Interannual variability of the OH sink is expected to be small, within ∼2% (Montzka *et al.*, 2011). This is equivalent to ∼10 $TgCH_4$/yr, the approximate size of inter-annual variability in CH_4 emissions (Bruhwiler *et al.*, 2014). Details of chemical loss fields can be found in Bergamaschi *et al.* (2005) and consist of a single, repeating seasonal cycle resulting in a CH_4 lifetime of approximately 9.5 years.

Model Simulations

I use a number of different model simulations, a control simulation in which prior emissions do not vary from year to year, and a series of emissions scenarios where Arctic wetland emissions increase each year. In the control simulation, prior emissions do not change (2000 anthropogenic emissions are used), so that only meteorology changes on an interannual basis. This allows me to determine the interannual variability in seasonal amplitude produced by variations in atmospheric transport alone and also acts as a reference time series with which I can compare the output from the emission scenarios. The emission scenarios are the same as the control simulation but with incremental increases in high-latitude wetland CH_4 emissions of 1, 2 and 5 $TgCH_4$/yr respectively, where the emissions increases are symmetric across the growing season. The high-latitude region is defined as an aggregation of the TransCom 3 regions boreal North America, boreal Eurasia and Europe. As some of Europe lies to the south of what might typically be considered high northern latitudes, the area of Europe north of 47°N is used in the definition of the high-latitude region as this roughly corresponds with the southern extent of boreal North America and Eurasia (Bruhwiler *et al.*, 2014). To compare model output with CH_4 mole fraction data, the 3D field of model CH_4 concentrations is sampled at the surface level at the nearest grid point to each of the NOAA/ESRL monitoring sites. The result is a time series made up of 48 data points per year (1 per 7.6 days). I then interpolate these time series to a constant weekly time step (52 data points per year) for consistent comparison with the CH_4 data.

I decompose the sampled time series into sub-annual, annual and trend components using the criteria previously defined. First, I check for consistency between the model and data by comparing the mean seasonal cycles from the model output and CH_4 data respectively. I then use the model time series for analysis of the seasonal cycle amplitude, as described for the CH_4 mole fraction data.

3.3 Analysis of Isotopes

My analysis of the δ^{13}C-CH_4 ratio at ALT and BRW is shown in Figure 3.3. It can be seen in the top panels that some years have sparse observations of the isotope, however each Keeling plot was calculated using at least 5 coinciding measurements in each window of 9 measurements across the time series. The middle panels show that the majority of intersects >-60‰ tend to occur in spring and winter whereas the opposite is true for summer and autumn. The time series mean intersects for summer and autumn are -68.79±13.55‰ and -69.47±13.55‰ for ALT and -68.10±12.90‰ and -64.74±4.81‰ for BRW respectively. Most isotopic wetland signatures tend to lie in this region where, for example, the signatures associated with worldwide boreal wetland emissions are typically between -69 to -65‰ (Striskantharajah *et al.*, 2012). This suggests that the large-scale variability in summertime CH_4 is driven by high-latitude wetlands, as expected.

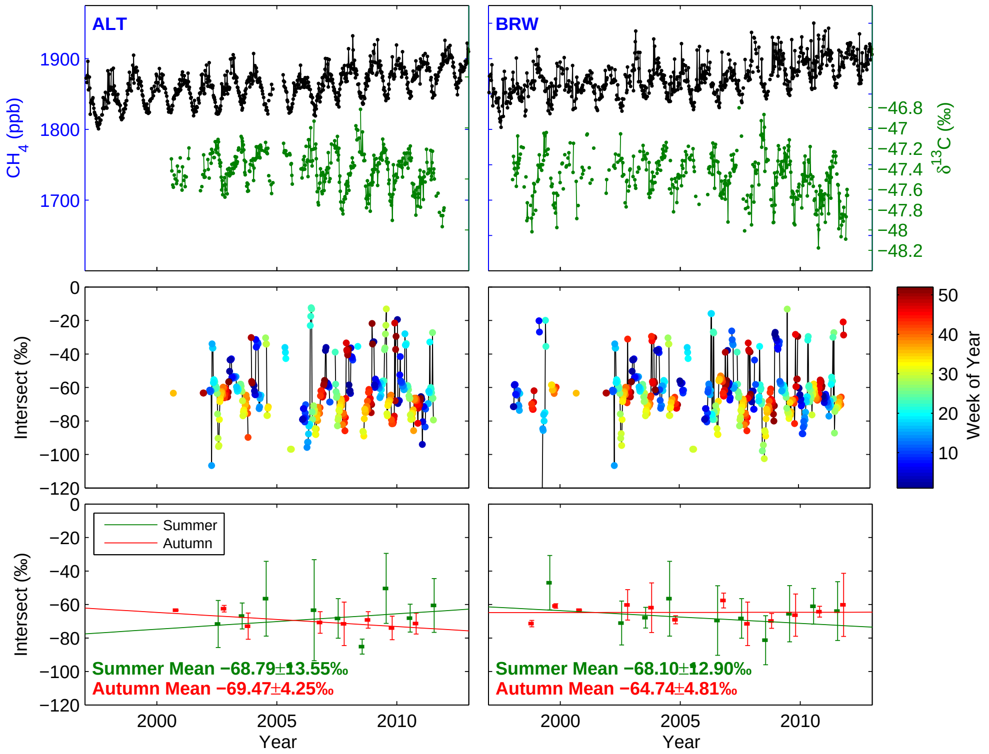

Figure 3.3: Top two panels show (black) CH_4 and (green) $\delta^{13}C$-CH_4 time series between 1997 and 2013 for (left) ALT and (right) BRW. Middle panels show the Keeling plot intersects for the 9 week running window calculated from $1/CH_4$ and $\delta^{13}C$-CH_4, where the colour of the markers represents the week of the year. The bottom panels show the seasonal mean intersects for (green) summer (JJA) and (red) autumn (SON) where the error bars show the standard deviation in each season and the solid lines show the linear trend in the seasonal means.

3.4 Barrow In situ Data Analysis

I use hourly averages from the continuous measurements of surface CH_4 at Barrow, Alaska (BRW) in an attempt to quantify changes in local summertime CH_4 anomalies associated with wetlands. I use hourly averages of local meteorological data, namely wind speed and wind direction to filter the CH_4 data by air sectors as defined in (Dlugokencky *et al.*, 1995). Measurements of CH_4 inbound from the north air sector (020°-110°) are typically used to avoid contamination from "non-background" or local sources, namely anthropogenic sources from gas wells and the town of Barrow, and emissions from the large areas of permafrost affected wetlands in the region. The air from the north air sector is therefore considered to be representative of "background" conditions and contain information about regional variations of CH_4. Here I also use measurements of CH_4 from the south air sector (135°-220°), which *does* contain information about the local emissions as well as regionally representative air. I use CH_4 measurements only when the wind speed is $\geq$1m/s and ensure that the selected meteorological conditions have been in effect for at least one hour. Examination of data from the north and south air sector indicates that there is significant diurnal variability of the CH_4 concentration from the south air sector, where there is a maximum between 03:00-05:00. To reduce potential biases without over-constraining the data, I calculate diurnal averages from 09:00-17:00, the period of least variability. Finally, I determine monthly averages from the filtered data. Figure 3.4 shows graphical representation of my choices of filtering criteria for wind direction and time of day. It can be seen in the bottom left panel of Figure 3.4 that prevailing winds from the north result in substantially more observations from the north air sector than from the south air sector. The top left panel shows that air from the south air sector typically has much higher CH_4 concentrations as a result of local emissions. The diurnal variability in CH_4 is much greater in the air from the south air sector, with the greatest variability in summer. It is suspected that this is partially a result of CH_4

building up in the boundary layer over night, but also due to the recirculation of air during onshore/offshore winds.

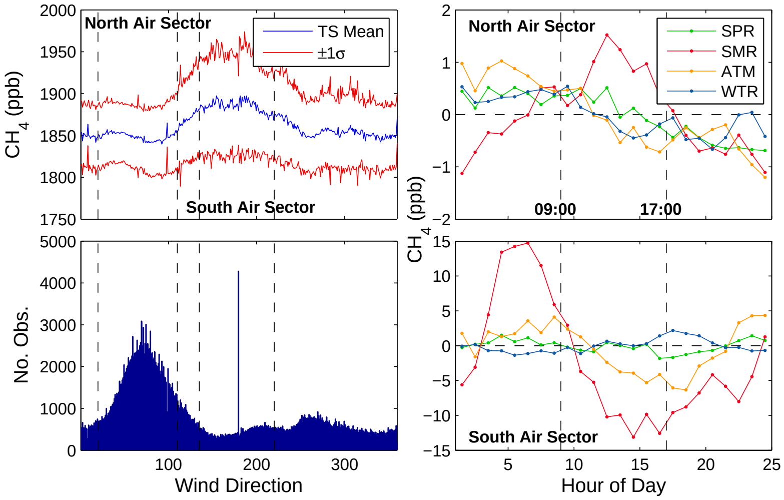

Figure 3.4: (Top left) mean CH$_4$ concentrations with 1σ observed from different wind directions (Bottom left) histogram showing the number of hourly observations taken of different wind directions (Top right) mean diurnal cycles measured during winds inbound from the north air sector for each season (Bottom right) mean diurnal cycles measured during winds inbound from the south air sector.

As the prevailing wind is from the north air sector, this sector is better represented by the observations than the south air sector. This leaves potential for biases. One way to better reduce large biases introduced by low number of observations is to use a curve-fitting procedure for comparison with the data averages. Figure 3.5 shows the BRW hourly CH$_4$ observations filtered according to air sector, where the top left inset panel shows the time series mean CH$_4$ seasonal cycle (blue) and the mean difference of the two time series (red).

There are some striking differences between the CH$_4$ concentrations inbound from the north and south air sectors. Notably, while they are both strongly seasonal, the seasonal maxima from the south air sector typically occurs during the ascending shoulder of the seasonal cycle and often overlaps with the seasonal

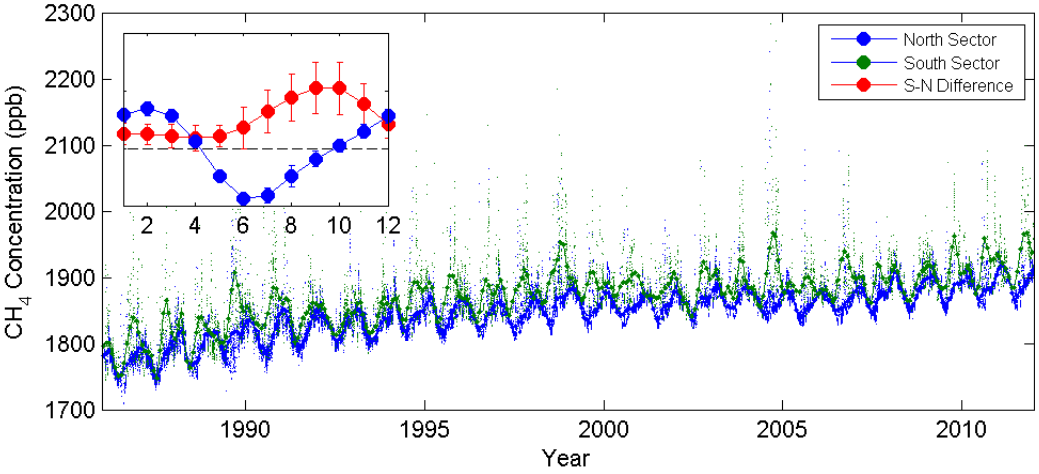

Figure 3.5: CH_4 time series filtered according to the criteria defined for the north (blue) and south (green) air sectors. The most significant differences between the two time series occurs during the summer and autumn months, when local wetland emissions peak, with the differences in winter being small. The top left panel shows the mean north air sector seasonal cycle, and the mean South-North Difference.

minima from the north air sector. The timing of the strong seasonal differences occurring primarily in summer and autumn are consistent with the timing wetland CH_4 emissions, which typically peak in late summer. Local anthropogenic sources are likely to play a minor role in these differences. In addition, the difference between the north and south CH_4 concentrations are small during the north air sector seasonal maxima, which occurs during winter when local wetland emissions are likely to be negligible. I subsequently calculate the "South-North" difference (SND) by subtracting the monthly-averaged CH_4 concentrations from the north air sector from those of the south air sector. In theory, this will remove the part of the CH_4 concentration that is representative of large, well-mixed air masses, leaving primarily the CH_4 anomalies resulting from sources local to BRW. I compare the CH_4 anomalies with an analysis of BRW 2 metre temperature data. I use the number of days >0°C as a temperature metric, representing the potential period of soil thaw and wetland CH_4 emission, although emission of CH_4 may continue until the soil has frozen over in autumn. Figure 3.6 shows a contour of temperature at BRW, where the dashed lines are the linear fit to the start and end dates of the >0○C period. The temperature at BRW typically rises above 0°C in June and drops below in September, however I find that these dates have been shifting by -3.0±2.6 days/decade ($p<0.01$) and +5.6±3.1 days/decade ($p<0.01$) respectively. Figure 3.7 shows the result of the CH_4 analysis and the resulting time series of summer CH_4 anomalies determined from the SND, compared to the annual rise in days >0°C.

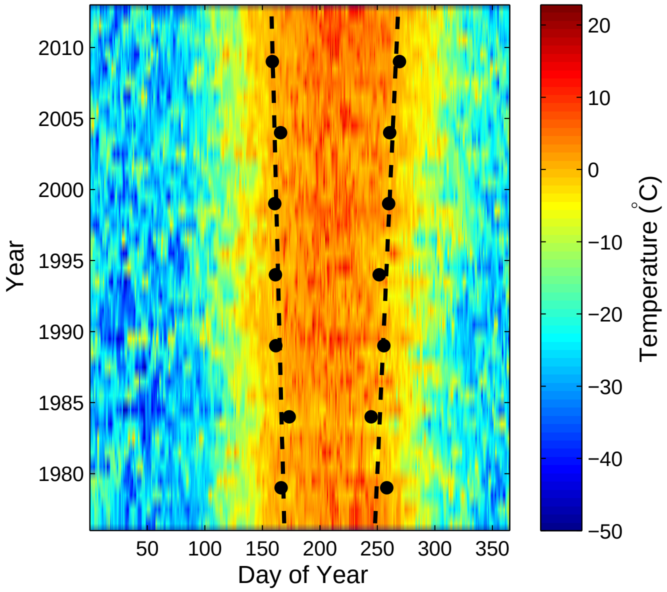

Figure 3.6: 2 metre temperature measurements at BRW, where colour represents changes in temperature seasonally (horizontal axis) and annually (vertical axis). Black markers are 5 year means of the dates when smoothed temperature passes above (left) and below (right) 0°C. Dashed black lines represent the least squares linear fit to the annual zero crossing dates. The time series mean zero crossing dates are approximately day 160 for -ve to +ve and 260 for +ve to -ve respectively.

Having calculated the SND summer anomalies, I find three periods of relatively high CH_4 anomalies and a positive linear regression coefficient of

5.4±9.0 ppb/decade which is not statistically significant ($p>0.1$). The interannual variability is similar using different filtering criteria and averages calculated from the data and curve fit (not shown), and while altering these variables does have an effect on the magnitude of the coefficient calculated from the summertime CH_4 anomalies at BRW, the sign of the coefficient remains positive in all cases. Despite this, there was no evidence of a trend. The sensitivity of the coefficient to filtering criteria is a result of the low number of CH_4 observations from the south air sector which is likely to significantly increase the effect of averaging biases and increases the uncertainties associated with the summer anomalies from the SND. This is not surprising as the site was chosen to be representative of background conditions. Despite this, I find that some of the temporal variability in CH_4 coincides with temperature variability, where the linear trend in the number of days $>0°C$ over the same time span is 8.2±7.7 days/decade ($p<0.01$), with a particularly rapid increase following 2000. The linear relationship between temperature and the CH_4 anomalies ($r^2=0.18$) is statistically significant, with a sensitivity of 0.47±0.42 ppb per additional day $>0°C$ ($p<0.05$), where some peaks in CH_4 (e.g. 2004) cannot be explained by temperature variability. The r^2 is small, which suggests a weak relationship, but it remains statistically significant for a range of CH_4 filtering criteria which gives some confidence that at least some of the observed changes in CH_4 may be due to physical mechanisms rather than an artefact of biases and data processing.

We have seen that emissions from the wetlands close to BRW are greatest during summer and early autumn. This partially overlaps with the seasonal cycle minima from the north air sector, and also creates a shoulder on the ascending phase of the seasonal cycle. A large-scale increase in high-latitude wetland emissions is therefore likely to have two major effects on high-latitude measurements of surface CH_4: first we expect an increase in the growth rate resulting from the net increase in emissions, and second, we expect both a reduction in the amplitude of

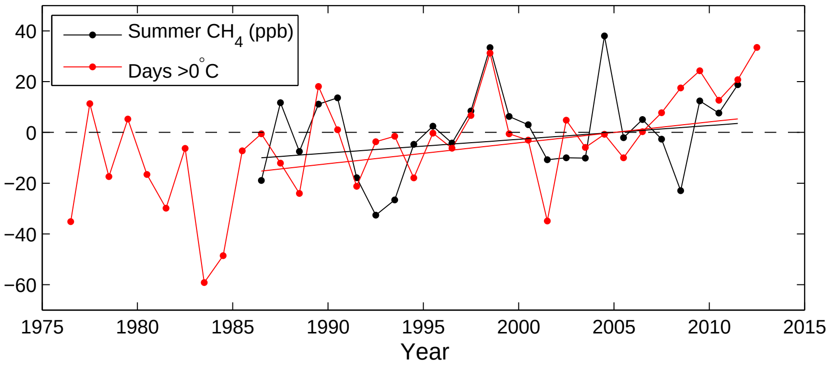

Figure 3.7: Summer CH_4 anomaly (black) and number of days >0°C (red) with linear least squares fit.

the seasonal cycle due to the summertime emissions partly "filling in" the seasonal minima, and an enhanced shoulder on the ascending edge of the seasonal cycle. In the next section I examine changes in the amplitude of the seasonal cycle at numerous high-latitude sites, before assessing how useful the amplitude is as an indicator of changes in wetland emissions. My hypothesis is that an increase in Arctic wetland emissions will lead to a decrease in the seasonal amplitude of CH_4.

3.5 Flask Time Series Data Analysis

Here I analyse time series of surface CH_4 concentrations from the high-latitude monitoring sites of the NOAA/ESRL CGASN - these sites are shown in Figure 3.2. The background flask sites sample air that is considered to be representative of large, well-mixed air parcels, and the high-latitude sites were selected as they are likely to be the most sensitive to changes in large-scale changes in emissions from Arctic wetlands.

Figure 3.8 shows the linear regression coefficients of seasonal amplitude of CH_4 calculated from monthly flask time series at sites in the NOAA/ESRL network

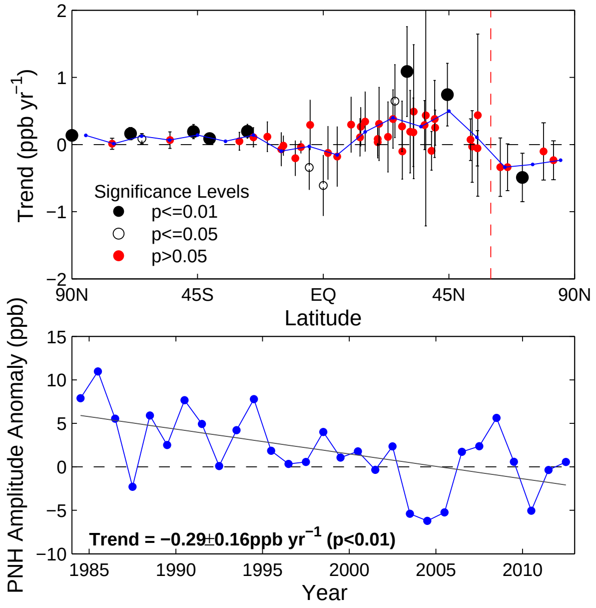

Figure 3.8: (Top) Linear regression coefficients of time vs. amplitude anomalies from individual CH_4 flask sites. Error bars indicate the 1σ uncertainty on the linear trends while significance levels are shown by the different markers. (Bottom) Time series of amplitude anomalies determined from the MBL CH_4 PNH zonal mean, with linear least-squares fit.

and a time series of seasonal amplitude for the PNH mean. The coefficients show a number of regional patterns: a small but statistically significant increase in amplitude in the southern hemisphere, huge variability in amplitude in the mid-latitude northern hemisphere, and decreasing amplitude in the high-latitude northern hemisphere. The high-latitude region contrasts with the other regions in that the linear regression coefficients lie consistently below zero, whereas most of the coefficients in the mid-latitudes lie above zero. The PNH mean seasonal amplitude, based on high-latitude CH_4 flask data is consistent with the negative coefficients of the individual sites, exhibiting a significant trend of -2.9±1.6 ppb/decade ($p<0.01$) over the 29 year period.

In order to test how robust this result is, I perform a more in-depth analysis of CH_4

at individual high-latitude sites. I calculate the seasonal amplitude at these sites using two methods and from both monthly and weekly time series determined from the NOAA/ESRL discrete CH_4 flask measurements. The first and most simple option is take the range of the detrended CH_4 concentration in a given year, termed the *annual range*. As the seasonal maxima occur during winter, this doesn't take account of the fact that there can be two seasonal maxima in one year when the timing of the maxima shift. A second option is therefore to take the peak to peak difference of one seasonal oscillation, termed the *seasonal range*. The results of this analysis are shown in Table 3.1.

The regression coefficients calculated from the seasonal amplitude time series when using NOAA/ESRL monthly means are predominantly negative. However, I find that there are just three sites that exhibit a statistically significant (or near) trend in amplitude over the time span of the data. These sites are ALT ($p<0.01$, since 1990), BRW ($p<0.01$) and STM ($p=0.06$), where time series of the amplitude anomalies at these sites are shown in Figure 3.9. While most of the decrease in amplitude at ALT occurs following 1990, the largest decrease at BRW and STM occur between 1984-1998 and 1984-2004 respectively. Interannual variability of the seasonal amplitude at ALT shows some correlation with the peaks and troughs in amplitude at BRW, however it is unclear whether the first few years of the ALT time series, which show a period of particularly low amplitude anomalies, were preceded by anomalously high years in amplitude as seen at BRW and STM.

I also calculate seasonal amplitude time series from discrete CH_4 mole fraction measurements (weekly means), the associated regression coefficients of these time series are also shown in Table 3.1. Interannual variability in the amplitudes appear to be sensitive to both the method of imputing missing data, and the filtering criteria defined in the wavelet transform, a result of the level of noise in the CH_4 time series. However, the regression analysis using weekly data still shows a statistically significant trend at BRW ($p<0.01$) and an even more robust trend at STM ($p<0.01$). The trend at ALT since 1990 is statistically significant ($p<0.05$) at -3.62±3.48 days/decade.

NOAA/ESRL Monthly Flask Data					
		Annual Range		Seasonal Range	
Site	Time Span	Mean$\pm1\sigma$ (ppb)	Trend$\pm1\sigma$ (ppb/decade)	Mean $\pm1\sigma$ (ppb)	Trend$\pm1\sigma$ (ppb/decade)
ALT	1986-2013	50.18±6.22	-2.34±2.90 ($p>0.1$)	50.21±6.00	-2.30±2.86 ($p>0.1$)
BRW	1984-2013	47.45±9.27	-4.91±3.61 ($p<0.01$)	47.73±9.34	-5.14±3.60 ($p<0.01$)
CBA	1984-2012	38.16±6.01	-0.60±2.60 ($p>0.1$)	37.92±5.95	-1.03±2.59 ($p>0.1$)
ICE	1993-2013	32.77±6.00	-3.37±4.35 ($p>0.1$)	32.45±5.65	-2.35±4.22 ($p>0.1$)
SHM	1986-2013	41.27±6.00	0.73±3.10 ($p>0.1$)	40.62±6.33	-2.35±3.10 ($p>0.1$)
STM	1984-2008	37.04±6.44	-3.38±3.49 ($p=0.06$)	36.37±6.15	-3.06±3.13 ($p=0.06$)
ZEP	1995-2013	46.23±4.73	-1.03±4.27 ($p>0.1$)	46.09±4.87	-0.92±4.41 ($p>0.1$)

NOAA/ESRL Weekly Flask Data					
		Annual Range		Seasonal Range	
Site	Time Span	Mean$\pm1\sigma$ (ppb)	Trend$\pm1\sigma$ (ppb/decade)	Mean$\pm1\sigma$ (ppb)	Trend$\pm1\sigma$ (ppb/decade)
ALT	1986-2011	56.26±6.14	-0.93±2.98 ($p>0.1$)	56.49±6.41	-1.05±2.87 ($p>0.1$)
BRW	1984-2011	56.17±8.55	-4.70±3.29 ($p<0.01$)	56.63±8.67	-4.48±3.31 ($p<0.01$)
CBA	1984-2011	45.49±7.93	-2.70±3.73 ($p\sim0.1$)	45.66±8.19	-2.91±2.58 ($p\sim0.1$)
ICE	1993-2011	39.75±7.35	-4.82±4.71 ($p<0.05$)	37.76±6.01	-2.58±4.45 ($p>0.1$)
SHM	1986-2011	48.36±6.93	3.43±4.05 ($p\sim0.1$)	48.84±6.60	2.81±3.81 ($p>0.1$)
STM	1984-2008	43.53±7.92	-5.65±3.69 ($p<0.01$)	41.96±7.28	-4.31±3.35 ($p<0.05$)
ZEP	1995-2011	52.97±5.49	-2.07±4.87 ($p>0.1$)	51.92±6.23	-1.79±5.61 ($p>0.1$)

Table 3.1: CH_4 amplitude trends at ALT, BRW, CBA, ICE, SHM, STM and ZEP determined from NOAA/ESRL monthly and weekly CH_4 data respectively.

We saw in Figure 3.1 that the first 5-6 years of the weekly BRW CH_4 time series had the largest proportion of missing observations. As a result, this section of the time series has a larger proportion of imputed data points which could have significantly contributed to the observed trend. However I repeated this analysis for the in situ observations at BRW by taking weekly averages from the north air sector and wavelet filtering them before calculating the equivalent amplitude time series. Figure 3.10 shows a comparison of the CH_4 concentrations and seasonal amplitude for annual and sub-annual frequency components determined from the flask and in situ time series respectively. Although there are occasionally large differences in the interannual variability of the flask and in situ amplitude anomalies, the in situ time series also exhibits a decline in the CH_4 seasonal amplitude which arguably persists for longer than in the flask time series. This comparison of two independent time series indicates that the amplitude trend is not a result of my treatment of the data but due to the presence of a trend in both time series. In both datasets, the trend is predominantly caused by a decrease in the annual component of the time series.

Although my analysis shows negative coefficients in the seasonal CH_4 amplitude at all but one of the high-latitude monitoring sites, the predominant sites are ALT, BRW and STM. My analysis suggests that ALT, BRW, and STM seem to be largely responsible for the negative amplitude trend observed in the PNH mean calculated from the MBL.

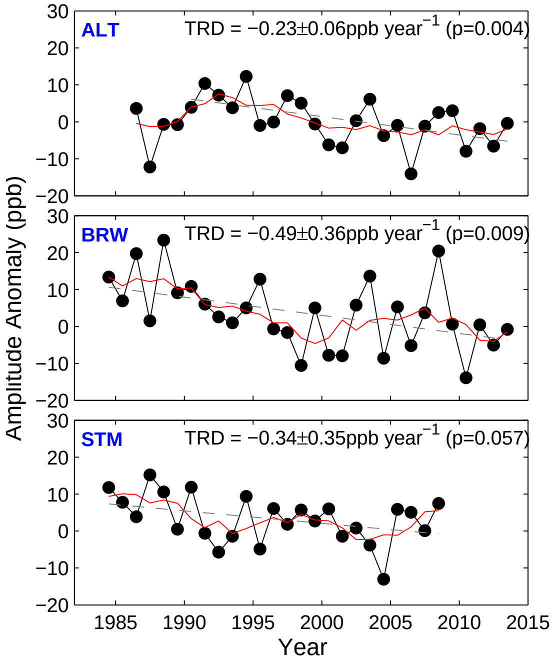

Figure 3.9: Time series of amplitude anomalies calculated from monthly averages of CH_4 at ALT, BRW and STM. TRD is the trend$\pm 1\sigma$ and p is the value of the trend.

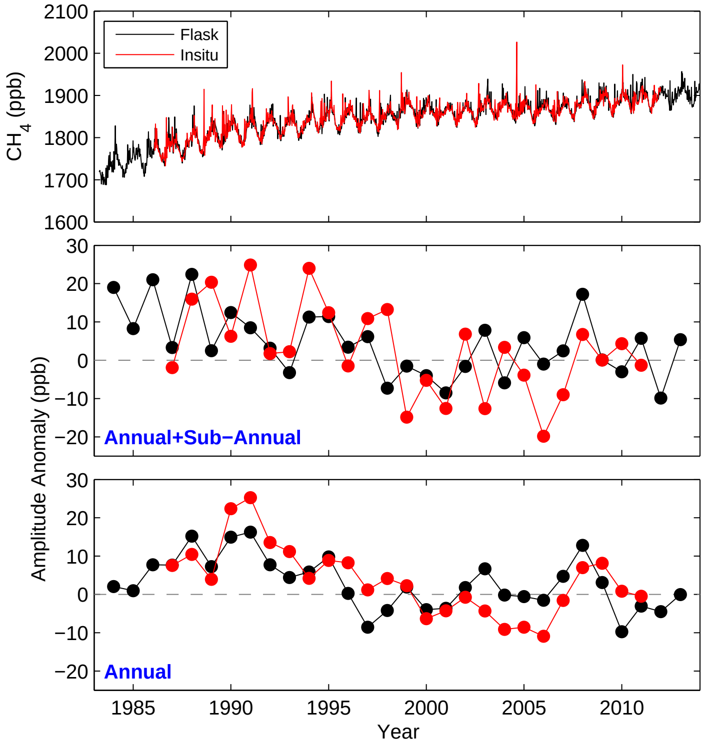

Figure 3.10: (Top) Comparison of flask and in situ CH_4 concentration. (Middle) Amplitude anomalies calculated from annual + sub-annual frequency components. (Bottom) Amplitude anomalies calculated from annual frequency component only.

There are a number of possible drivers of these observed trends: (1) atmospheric transport variability, (2) a change in Arctic wetland emissions, (3) a trend transported from mid-latitude CH_4 sources or (4) variability in OH. In the next section I will use the TM5 model output to investigate the first and second of these hypotheses.

3.6 TM5 Emission Experiments

Here, I aim to (1) determine the contribution of atmospheric transport to the observed trend in the high-latitude CH_4 seasonal amplitude and (2) investigate the magnitude of trends in amplitude we would expect to see given a range of different emission scenarios.

3.6.1 Control Simulation

My first use of the TM5 control simulation is to test whether the modelled seasonal cycle is consistent with the seasonal cycle observed in the data. Although the control simulation uses prior emissions which remain the same each year, I expect that the seasonal cycles should at least be similar in shape and amplitude when compared with the data. To do this, I simply isolate the seasonal cycle using the wavelet transform (same filtering criteria as used previously) and take the mean seasonal cycle, before making a comparison with the equivalent seasonal cycle from the data at each site. These comparisons can be seen as solid lines in the lower panel of Figure 3.11. Most of the seasonal cycles generated using the model closely match those calculated from the data indicating that the CH_4 priors and meteorology used in the model are able to describe realistic variations in CH_4. The timing of the seasonal minima/maxima and the seasonal amplitude are captured at ALT, CBA, SHM and ZEP. The model does not capture well the seasonal cycle at ICE or STM as it largely underestimates the seasonal cycle amplitude. These sites are in relative close proximity to each other and the poor representation of the seasonal cycle at these locations is likely to be caused by an issue with the ACTM. It is therefore necessary to exclude an interpretation of ICE and STM from my model analysis. At BRW, there appears to be a “hump” on the descending edge of the seasonal cycle which is not apparent in the data, and this leads to a much later minima in the modelled BRW seasonal cycle. It is suspected that this is due to the presence of local emissions that are sampled by the model but not observed in the data. This is due to the NOAA/ESRL BRW bi-weekly flask samples being collected when the wind is from offshore, which largely negates the contribution from the local emissions, whereas the model includes CH_4 concentrations from onshore and offshore. This is particularly apparent at BRW because the site is in close proximity to areas of natural wetlands. In contrast, most of the other Arctic sites are more remote, which means that there is some delay before they pick up the wetland signal and by this time the air is more well mixed and representative of a larger area. This difference in sampling at BRW and the subsequent over estimate of the early summer wetland CH_4 anomaly in the modelled CH_4 time series must be taken into account in the interpretation of the results.

I also use the control simulation to look at the interannual variability and trend in amplitude as a result of changes in atmospheric transport of CH_4 to each of the Arctic sites. I first calculate regression coefficients from the individual amplitude time series from the data and the model, and second determine the Pearson correlation coefficient and p-value corresponding to the relationship between the two time series. The results of this analysis are shown in Table 3.2. The model simulation did not extend as far back as some of the observations and thus my analysis only shows a comparison during the period of overlap. My results show that the amplitude regression coefficients resulting from atmospheric transport typically have the same sign as the coefficients determined from the data, but also that some sites exhibit coefficients of a similar magnitude and correlated amplitude anomalies. The correlation coefficients for the most part are small ($<$0.26). The TM5 amplitude regression coefficient for ALT CH_4 driven by atmospheric transport is -6.10 ± 6.29 ppb/decade, which is larger than the coefficient observed in the data by $\sim$1.5-3 ppb/decade. Variations in CH_4 seasonal amplitude driven by transport are also correlated with some of the interannual variability observed in the data at ALT, although the relationship between the time series is not statistically significant. The most robust decrease in seasonal amplitude was observed at BRW and I noted that the largest decrease occurred in the earlier years of the time series. The regression coefficient for the BRW data during the period overlapping with the model output is not statistically significant but is still negative in sign. The magnitude of the trend observed in the data is matched by the coefficient for amplitude changes driven by atmospheric transport, and shows a statistically significant correlation with the monthly amplitude anomalies, but not those calculated from the discrete measurements. Atmospheric transport also seems to explain the change in amplitude at the only site that showed a positive trend, SHM. ZEP exhibits a negative (but not statistically significant) trend in amplitude of -2.80±6.41 ppb/decade, while the model suggests transport has caused a very large increase in the seasonal amplitude of 6.63±8.94 ppb/decade. The statistically significant relationship between the model and data amplitude anomalies at ZEP is not representative of the trend, but the interannual variability which appears to be well explained by transport.

This analysis shows that variability in atmospheric transport could be a large factor in driving the CH_4 seasonal amplitude in the high latitudes. At ALT, a statistically significant trend in seasonal CH_4 amplitude ($p<0.05$) results from variations in atmospheric transport, although the reasons for this remain unclear. While the trend at BRW can be explained by transport during the period of overlap with the model, the biggest decrease occurs in the earlier years of the time series for which I do not have model output. We would therefore require a control simulation which extends further back in time to determine the proportion of the amplitude trend which is driven by atmospheric transport at BRW.

NOAA/ESRL Monthly Flask Data					
		Amplitude Trend		**Regression**	
Site	Time Span	Data (ppb/dec)	Model (ppb/dec)	r^2	p-value
ALT	1990-2010	-4.39±4.45	-6.10±6.29	0.13	0.10
BRW	1990-2010	-2.96±6.39	-2.74±8.06	0.18	0.05
CBA	1990-2010	-1.68±4.90	-0.21±6.23	0.01	0.58
ICE	1990-2010	-1.56±6.29	9.40±8.57	0.02	0.65
SHM	1990-2010	3.33±4.54	1.70±7.50	0.26	0.01
STM	1990-2010	-0.28±5.60	-1.70±12.39	0.20	0.04
ZEP	1990-2010	-0.90±6.52	6.63±8.94	0.33	0.01
NOAA/ESRL Weekly Flask Data					
		Amplitude Trend		**Regression**	
Site	Time Span	Data (ppb/dec)	Model (ppb/dec)	r^2	p-value
ALT	1990-2010	-3.15±3.89	-6.10±6.29	0.16	0.06
BRW	1990-2010	-2.33±4.86	-2.74±8.06	0.07	0.24
CBA	1990-2010	-2.03±4.87	-0.21±6.23	0.02	0.52
ICE	1990-2010	-3.73±5.61	9.40±8.57	0.01	0.72
SHM	1990-2010	3.35±4.86	1.70±7.50	0.20	0.03
STM	1990-2010	-1.63±4.68	-1.70±12.39	0.03	0.47
ZEP	1990-2010	-2.80±6.41	6.63±8.94	0.07	0.32

Table 3.2: Trends in amplitude from the data and model (calculated for the overlapping time period) and r^2 and p-values of their relationship.

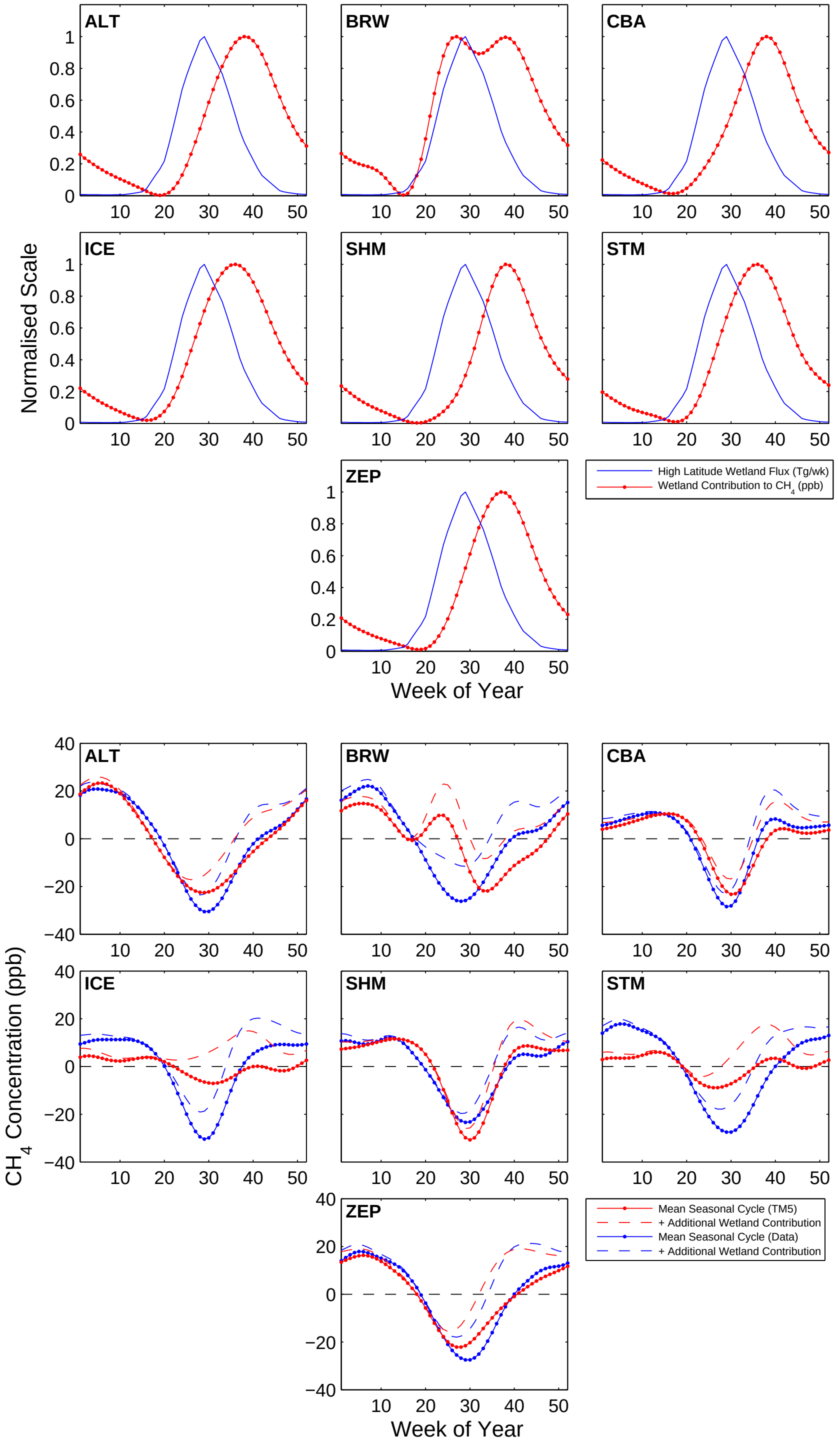

Figure 3.11: Top panel shows the high-latitude wetland flux (solid blue) and the resulting increase in seasonal CH_4 concentration observed at individual monitoring sites. Bottom panel shows mean seasonal cycles calculated from CH_4 mole fraction data (solid blue) and TM5 control simulation (solid red). Dashed lines show mean effect of additional wetland emissions (15 $TgCH_4$) to the seasonal cycles.

3.6.2 Emissions Scenarios

Next I introduce three emissions scenarios, by adding a trend to the prior CH_4 wetland emissions of 1 $TgCH_4/yr$, 2 $TgCH_4/yr$ and 5 $TgCH_4/yr$ respectively, in order to assess the observed effects of the increased emissions on the high-latitude CH_4 seasonal cycle amplitude. As an example, the time series generated at BRW for the control simulation, and each of the emissions scenarios are shown in Figure 3.12. First I look at the timing of the additional wetland emissions relative to the seasonal CH_4 concentration. In order to isolate the additional contribution from wetland emissions "seen" at each site, I subtract the control simulation time series from the emissions scenario time series. The remaining residual time series is made up of a seasonal variation in CH_4 which peaks in the summer when wetland emissions are highest, overlying a trend component resulting from the additional CH_4 flux into the atmosphere. In order to isolate the seasonal component, I remove the trend by fitting a smooth curve through the seasonal minima and subtracting it from the residual time series. The wavelet transform is inappropriate for this as it would centre the seasonal oscillation on zero.

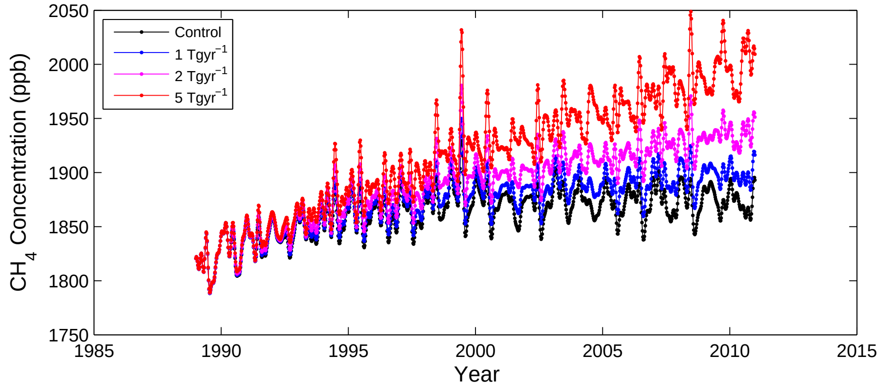

Figure 3.12: BRW TM5 time series for the control run and 1, 2 and 5 $TgCH_4/yr$ high-latitude wetland emissions scenarios respectively, where each time series has been filtered of high frequency variability using the wavelet transform.

The top panel of Figure 3.11 shows the prior CH_4 high-latitude wetland flux used in the TM5 simulation, and the seasonal component of the wetland contribution to the CH_4 concentration measured at individual monitoring sites. There is a delay between the peak emission in the CH_4 wetland flux and the apparent CH_4 concentration, where the delay depends on the distance of the site from wetlands. BRW appears to see an immediate rise in CH_4 due to a combination of differences in the way the air is sampled in the model and data, and due to its close proximity to large areas of wetlands. The wetland CH_4 signal takes several weeks longer to reach some of the more remote sites. The dashed lines in the lower panel of Figure 3.11 show the effect of adding an increase in wetland emissions of 15 TgCH_4 to the mean seasonal cycle. It is clear that at some sites, such as ALT and BRW, additional wetland emissions are likely to reduce the seasonal amplitude. At some sites, both the minima and maxima of the seasonal cycle are raised, in which case the amplitude would not be a good metric to show changes in wetland emissions. The additional wetland emissions are very evident over the ascending edge of the seasonal cycle in Figure 3.11, but this would be non-trivial to detect when analysing detrended CH_4 mole fraction data due to the aliasing effects of detrending discussed in the previous chapter, and the level of noise often contained within the CH_4 time series.

So far I have primarily focused on the seasonal cycle amplitude calculated from the combined annual + sub-annual frequency components of the CH_4 time series. Table 3.3 shows the amplitude regression coefficients and variability determined separately from the annual and annual + sub-annual components of the seasonal cycle for each scenario at ALT, BRW, CBA, SHM and ZEP. At the majority of sites, there is not a consistent decrease in amplitude for either seasonal cycle as wetland emissions increase. For example, a trend of 1 TgCH_4/yr produces

	Frequency Component			
ALT	**Annual**		**Sub-Annual + Annual**	
Scenario	Mean±σ (ppb)	Trend (ppb/decade)	Mean±σ (ppb)	Trend (ppb/decade)
Control	42.4±7.3	-6.8±3.9 ($p<0.01$)	54.7±9.6	-6.1±6.2 ($p<0.1$)
1TgCH$_4$/yr	40.5±7.0	-7.7±3.9 ($p<0.01$)	52.4±9.6	-7.4±5.9 ($p<0.05$)
2TgCH$_4$/yr	39.7±6.5	-6.1±4.1 ($p<0.01$)	53.1±8.5	-4.1±6.2 ($p>0.1$)
5TgCH$_4$/yr	44.4±8.7	4.7±4.6 ($p>0.1$)	61.6±14.1	10.7±8.8 ($p<0.05$)
BRW	**Annual**		**Sub-Annual + Annual**	
Scenario	Mean±σ (ppb)	Trend (ppb/decade)	Mean±σ (ppb)	Trend (ppb/decade)
Control	27.3±4.3	1.1±3.1 ($p>0.1$)	49.7±11.4	-2.7±8.1 ($p>0.1$)
1TgCH$_4$/yr	20.9±5.0	-4.1±3.0 ($p<0.01$)	48.4±14.9	-5.3±10.4 ($p>0.1$)
2TgCH$_4$/yr	13.7±7.5	-8.5±3.7 ($p<0.01$)	50.1±18.5	-4.5±13.1 ($p>0.1$)
5TgCH$_4$/yr	19.9±10.7	6.2±7.2 ($p<0.1$)	64.6±24.1	10.4±16.6 ($p>0.1$)
CBA	**Annual**		**Sub-Annual + Annual**	
Scenario	Mean±σ (ppb)	Trend (ppb/decade)	Mean±σ (ppb)	Trend (ppb/decade)
Control	21.3±4.5	1.5±3.3 ($p>0.1$)	41.1±8.7	-0.2±6.2 ($p>0.1$)
1TgCH$_4$/yr	18.9±4.2	-3.4±2.6 ($p<0.01$)	39.9±7.9	-0.3±5.7 ($p>0.1$)
2TgCH$_4$/yr	18.7±3.6	-1.2±2.5 ($p>0.1$)	43.4±9.5	6.4±6.0 ($p<0.05$)
5TgCH$_4$/yr	23.9±10.0	9.6±5.6 ($p<0.01$)	52.7±15.4	18.6±7.0 ($p<0.01$)
SHM	**Annual**		**Sub-Annual + Annual**	
Scenario	Mean±σ (ppb)	Trend (ppb/decade)	Mean±σ (ppb)	Trend (ppb/decade)
Control	30.3±7.2	0.4±5.1 ($p>0.1$)	51.6±10.5	1.7±7.5 ($p>0.1$)
1TgCH$_4$/yr	29.2±6.9	-0.1±4.9 ($p<0.01$)	51.6±10.6	2.2±7.5 ($p>0.1$)
2TgCH$_4$/yr	29.8±6.4	1.9±4.5 ($p>0.1$)	54.5±11.3	7.4±7.4 ($p<0.1$)
5TgCH$_4$/yr	35.2±9.1	11.3±3.8 ($p<0.01$)	66.7±17.4	20.5±8.0 ($p<0.01$)
ZEP	**Annual**		**Sub-Annual + Annual**	
Scenario	Mean±σ (ppb)	Trend (ppb/decade)	Mean±σ (ppb)	Trend (ppb/decade)
Control	35.3±8.2	6.0±9.2 ($p>0.1$)	57.3±8.1	6.6±8.9 ($p>0.1$)
1TgCH$_4$/yr	33.1±8.1	5.4±9.2 ($p>0.1$)	56.7±11.3	7.1±12.9 ($p>0.1$)
2TgCH$_4$/yr	33.4±8.1	10.1±7.9 ($p<0.05$)	63.4±18.2	18.0±19.4 ($p<0.1$)
5TgCH$_4$/yr	44.2±15.4	27.4±9.1 ($p<0.01$)	84.9±33.1	46.1±29.7 ($p<0.01$)

Table 3.3: Mean seasonal cycle amplitude and amplitude trends calculated from the annual and annual + sub-annual components of the TM5 control simulation and emission scenario time series.

a more negative coefficient relative to the control at ALT, whereas a trend of 2 $TgCH_4$/yr causes a more positive coefficient. Likewise at CBA, the 1 $TgCH_4$/yr simulation doubles the magnitude of the negative coefficient determined from the annual component, but 2 $TgCH_4$/yr brings the coefficient closer to zero. Furthermore, the sites of SHM and ZEP see a consistent increase in amplitude as the wetland emissions increase, where ZEP in particular sees the largest increase in amplitude. The extreme scenario of 5 $TgCH_4$/yr results in large increases in amplitude at all sites. BRW is an exception in that the amplitude trend determined from the annual component becomes consistently more negative from the control (1.1±3.1 ppb/decade, $p>0.1$), to 1 $TgCH_4$/yr (-4.1±3.0 ppb/decade, $p<0.01$) to 2 $TgCH_4$/yr (-8.5±3.7 ppb/decade, $p<0.01$). At the end of the BRW time series in the 2 $TgCH_4$/yr emission scenario, the annual component of the BRW seasonal cycle has completely diminished. From my analysis, BRW is clearly the most sensitive site to increases in wetland emissions - this point is emphasised in Figure 3.13, which shows the wavelet power spectrum of the residual from subtracting the control simulation time series from the 1 $TgCH_4$/yr scenario time series. A gradual increase in power of the annual frequency of the spectrum is evident of the increasing wetland emissions. Although some variability is introduced to the sub-annual frequencies, this does not appear to be present in the form of a trend.

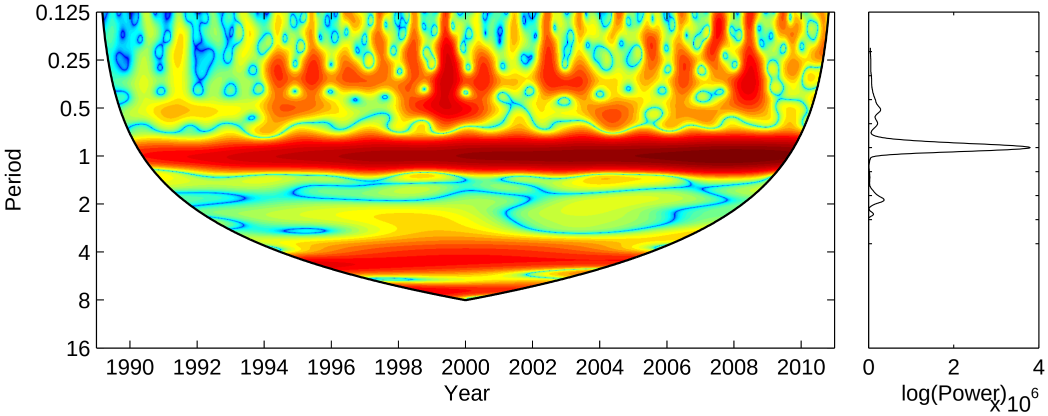

Figure 3.13: The left panel shows the wavelet coefficient matrix calculated by subtracting the wavelet coefficient matrix of the BRW control simulation from that of the BRW 1 TgCH_4/yr wetland simulation. The right panel shows the global power spectrum for the coefficient matrix and indicates that the dominant frequency which differs between the two time series is the annual frequency.

3.7 Summary

My analysis of high-latitude surface temperature data suggests that the period of potential ice thaw (>0°C) has lengthened significantly over the past 30 years. The trends calculated from the gridded MERRA reanalysis dataset indicated that temperature trends over high-latitude wetland areas in boreal and Arctic North America and Eurasia were predominantly positive, ranging from +0.5 to 8 days/decade. My analysis of temperature at the BRW site in Alaska was at the higher end of the scale with a trend of 8.2±7.7 days/decade where most of the change (5.6±3.1 days/decade) was due to an increase in autumn warming, indicating that trends could be much stronger at local scales. While temperature is not the only controlling variable on CH_4 emission rates from thawed soils, the rapid warming recently observed in the Arctic is a clear indicator of the potential for large-scale increases in CH_4 emissions.

I used in situ CH_4 observations at BRW, filtered by air sector, to look at local changes in summertime CH_4 anomalies. By subtracting monthly mean CH_4 concentrations from the north air sector from those of the south air sector, I isolated CH_4 anomalies that I expect are representative of CH_4 emissions from the North Slope of Alaska. Although there are other local sources of CH_4 in the vicinity of the BRW site, the seasonal variation in CH_4 anomalies were consistent with those of wetland emissions, with a seasonal peak in late summer/early autumn. I found that although the summertime CH_4 anomaly from the south air sector was increasing by 5.4±9.0 ppb/decade, the trend was not statistically significant ($p>0.1$). The CH_4 anomalies were correlated with surface temperature anomalies measured at the site of BRW, with a statistically significant relationship of 0.47±0.42 ppb for each additional day >0° ($p<0.05$). This analysis was inherently biased, as the site of BRW was chosen specifically because of the prevailing winds from the north, leading to limited observations from the south air sector. Despite this I did not find that expanding the filtering criteria I used to define the air sectors resulted in anything but a positive trend in CH_4 anomalies. It was noted that the seasonal peaks in the south air sector CH_4 time series typically coincided with the seasonal minima or the ascending edge of the seasonal cycle from the north air sector. The north air sector contains information about much larger scale fluxes of CH_4, including those in low, mid and high latitudes. I hypothesised that a large-scale increase in wetland emissions, and the subsequent increase in the seasonal peak could "fill" in part of the seasonal minima of time series that are representative of large-scale CH_4 concentrations. The most sensitive of these are likely to be flask sites in the northern high latitudes.

I found a statistically significant decrease in the seasonal amplitude in the PNH mean determined from the MBL CH_4 surface. This time series is based on CH_4 observations at individual sites and weighted according to the size of the air mass that they typically represent. I found statistically significant trends in amplitude at a number of the high-latitude flask sites, where the most robust trend was observed at BRW, showing a decrease of approximately 14.10 ± 9.90 ppb over 30 years. The use of in situ and flask data both confirmed the presence of a trend in BRW seasonal CH_4 amplitude indicating that the trend is not a result of the way I handled missing data. The site of BRW also happens to be in closest proximity to wetlands, while many of the other sites are relatively isolated such that the relative timing of the seasonal CH_4 minima, and the peak in CH_4 resulting from summertime wetland emissions are likely to have less overlap. While this result was consistent with my hypothesis, there are numerous other factors that can influence the seasonal amplitude. One of these would be a change in the amount of OH, as this could for example limit the amount of CH_4 destroyed in the atmosphere, however a number of studies have found that there is no trend in OH that could cause such a change (e.g. Dlugokencky *et al.* (1997)). Two further possibilities were that a trend in CH_4 emission from the mid-latitudes could have been transported to the northern sites, or that a change in atmospheric transport alone could result in the decreased amplitude.

I used a number of simulations from the TM5 ACTM to interpret the recent variability in the high-latitude CH_4 seasonal amplitudes. The first was a control simulation to assess the variability in CH_4 introduced by changes in atmospheric transport alone. This simulation showed that the trends in seasonal amplitude observed in the flask sites were easily within the range of the changes induced by atmospheric transport, and that atmospheric transport also resulted in large interannual variability in the amplitude. However at this stage in my analysis, I was not able to use a simulation that extended as far back in time as flask time series such as BRW. This is significant, because the biggest decrease in amplitude at BRW is observed in the earlier years of the time series. Secondly there were some issues with the TM5 simulations that are still being resolved. For example, the modelled BRW seasonal cycle includes CH_4 from the south, whereas the NOAA/ESRL GMD only use CH_4 samples when the wind is coming from the north.

Finally, I found using a number of emissions scenarios that using the seasonal amplitude as a metric for changes in wetland emissions was not useful at most sites. BRW seems to be an exception as this experiment resulted in a strong decrease in the annual frequency component of the seasonal cycle. Although this was also observed in the CH_4 flask and in situ data, I cannot at this point prove that this was not a result of changes in atmospheric transport. In addition, this result is likely to be exaggerated due to sampling differences between the model and data.

A major weakness of this analysis was the assumption that the timing of the edges of the high-latitude growing season does not change, as I used prior wetland emissions which were symmetric about the growing season. Substantial warming at both edges of the growing season suggests that this is unlikely to be the case. For example, there is evidence for rapid increases in CH_4 emissions during spring (Song *et al.*, 2012) and that there is a relationship between autumn emissions and spring emissions the following year (Sturtevant *et al.*, 2012; Mastepanov *et al.*, 2013). Earlier spring emissions would result in more overlap of the high CH_4 anomalies resulting from Arctic wetlands with the seasonal minima from the large-scale seasonal cycle, while an increase in autumn emissions could offset this by increasing the seasonal maxima.

At present I do not appear to have sufficient evidence to link the recent decrease in the high-latitude CH_4 seasonal amplitude to an increase in Arctic wetland emissions. It is possible that this trend is a result of a shift in atmospheric transport, however the reasons for this are not currently understood. This will therefore be a topic for future research. It appears that there would have to be large increases in Arctic wetland emissions before they become detectable in high-latitude CH_4 seasonal cycles. Our ability to detect such changes is essential however, as permafrost CH_4 could contribute significantly to the carbon-climate feedback.

Chapter 4

PERSIST - Prototype Earth obseRving System using Image Slicer Technology

PERSIST is the Prototype Earth obseRving System using Image Slicer Technology. The PERSIST project was funded by the Centre for Earth Observation Instrumentation (CEOI) as a seed-corn study that took place at the UK Astronomy Technology Centre (ATC) during January and February of 2012. The aim of the project was to build a bench mounted prototype image slicer spectrometer with a SWIR detector system capable of measuring the atmospheric spectra need to infer XCO_2. The instrument should have the ability to (1) simultaneously measure three wavelength ranges with one spectrometer (2) demonstrate the feasibility of the technology for use in an Earth Observation instrument to measure atmospheric CO_2. My contribution to this project was the lab-based testing of the bench mounted prototype spectrometer and analysis of the results. The results of the study were placed in an CEOI report but also published in SPIE (Lee *et al.*, 2012). First I will introduce the basic concepts of observing XCO_2 from space. In the following section I will introduce the instrument concept and layout of the bench mounted prototype before presenting the test results.

4.1 Introduction

Space-based observations of XCO_2 from low-Earth orbit sensors have the potential to dramatically improve our knowledge of the carbon cycle. The primary advantage of space-borne sensors is the potential of repeated global coverage with high spatial resolution over the vast areas of the Earth where the ground-based measurement network remains sparse. To be effective, these instruments need a high spatial resolution in order to locate important point sources of CO_2 but also a high spectral resolution in order to detect diffuse spatial variations in CO_2 that reflect larger scale sources and sinks. CO_2 in the atmosphere is considered to be well mixed, a result of its long lifetime in the atmosphere and relatively low levels of natural variability. As a consequence, there are only small changes in XCO_2 over large spatial scales. This represents a significant challenge to the carbon cycle science community.

At present there are two primary systems typically used to measure XCO_2 from space: the “push broom” system and the Fourier Transform Spectrograph. Both of these systems measure three atmospheric spectra necessary to infer concentrations of XCO_2: the Oxygen (O_2) A-Band, the weak CO_2 band, and the strong CO_2 band with central wavelengths of approximately 765, 1605 and 2060 nm respectively (Crisp *et al.*, 2004). Each waveband plays an important role in determining an accurate XCO_2 concentration. The Weak CO_2 band for example is the most sensitive to surface CO_2. The Strong CO_2 band provides a second, independent measure of the CO_2 abundance. This waveband however is particularly sensitive to variations in atmospheric pressure and moisture, as well as certain aerosol particles. The O_2 band is useful because it provides a measure of the presence of aerosols and clouds which would reduce the measurement accuracy, and also allows the determination of surface pressure which is necessary to retrieve the XCO_2 concentration.

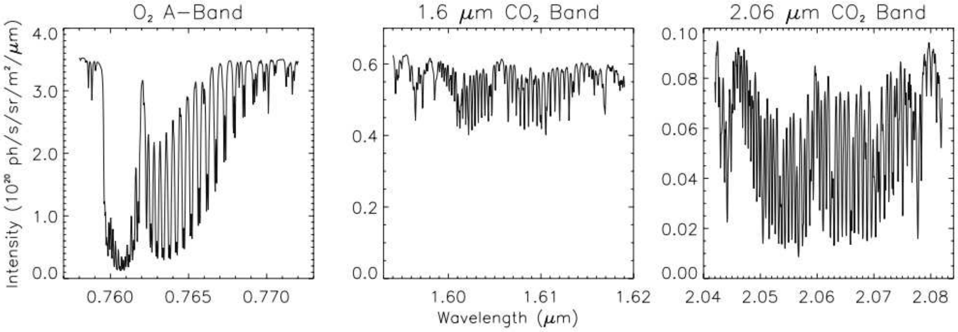

Figure 4.1: Atmospheric spectra observed by OCO in the O_2, Weak CO_2 and Strong CO_2 wavebands respectively (Connor *et al.*, 2008).

Fourier Transform Spectrographs such as GOSAT have been utilised for space-based missions in order to improve spectral sampling. These instruments typically offer very high spectral resolution but the instrument design is high in complexity with coinciding increases in cost and weight. Furthermore, the effective scanning of the instruments means that light collection can still be inefficient and spatial sampling is more sparse than a "push broom" system.

OCO is an example of a "Push broom" system. It provides a spectrum in one spatial dimension and builds up a second spatial dimension in time as the satellite passes over the Earth's surface or by use of a scanning system. Systems such as OCO use a dispersive spectrograph to sample the spectral dimension. The primary limitation of this technique is the amount of light that can pass through the aperture. Only a small amount of the available light can be transmitted through the slit, which compromises the level of the signal that can reach the detector. This leads to a reduction in either spatial or spectral sampling. The

OCO design uses three separate spectrometers and detectors, one to capture the O_2, weak CO_2 and strong CO_2 wavebands respectively. For each wavelength channel, light enters a slit which illuminates the instrument detector, however only a small proportion of the detector is filled with useful information.

An Integral Field Spectrometer (IFS) can overcome this problem. The feasibility of using an IFS for Earth Observation was determined in a theoretical study by (Lee *et al.*, 2011). An IFS consists of an Integral Field Unit (IFU) which contains an *image slicer*. The image slicer reformats light entering the instrument to form three entrance slits to the spectrometer, one slit for each waveband. A *multiple diffraction order spectrometer* is then used to simultaneously disperse spectra for the three wavelength channels onto the same detector. This fills the detector with useful information making more efficient use of the available space. The use of an IFS can provide numerous performance advantages, but can also reduce the weight and cost of an instrument while providing similar performance to an instrument such as OCO. The science requirements for the feasibility study of using the IFS for space-based XCO_2 measurements are shown in Table 4.1. If an instrument such as OCO implemented the IFU, it would have three detectors to fill with useful information. This could provide a three fold improvement in exposure time, increasing signal to noise, or a three fold increase in spatial resolution (because exposure time can be reduced by a factor of three). Alternatively, an instrument developed with an IFU could measure the three wavelength channels required for XCO_2 with just one spectrometer and one detector, substantially reducing the instrument weight and cost of the mission. The image slicer is not limited to three slices. An instrument that utilised an IFU could also measure additional wavelength channels, for example those required to infer XCO and XCH_4.

The PERSIST design is based on the use of this technology to provide simultaneous coverage of a number of different wavelength channels for the measurement of

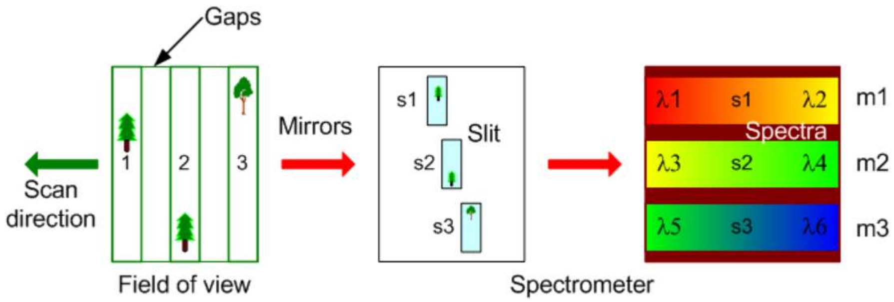

Figure 4.2: Schematic describing the principle of operation of the CEOI-IFS hyperspectral imager used in PERSIST.

XCO_2. Figure 4.2 describes the principle of operation of PERSIST when used to observe XCO_2 from space. The field of view (left) on the ground is sampled by the image slicer mirror. Re-imaging optics then reformat the three slices into three slits which form the entrance slit at the focal plane of the spectrometer. Each slit forms a spectrum with a different wavelength range, with the spectrometer subsequently dispersing the light from each slit onto the instrument detector. The spectra, which contain information about absorption in the respective wavelength channels are used to infer XCO_2 concentrations sampled in space and time.

To test the instrument concept, I performed a number of laboratory tests on PERSIST. The lab setup is described in the following section.

Requirement	**Performance Target**
Orbit	Sun synchronous orbit
Orbit altitude	705km
Viewing modes	Nadir
Ground track	6.78km/s
Swath width	$\geq$10km
Spatial resolution	Across track: 1.3km, Along track: 2.2.km
Instrument	3 channel imaging grating spectrometer
Wavelengths	O_2:758-772nm, CO_2:1594-1619nm, CO_2:2042-2082nm
Spectral Resolution	O_2:21000, CO_2:24000, CO_2:24000
Signal to Noise	O_2:>TBD, CO_2:>300, CO_2:>240

Table 4.1: Science requirements of CEOI-IFU mission, adapted from Lee *et al.* (2011).

4.2 PERSIST Laboratory Layout

Figure 4.3 shows a schematic of PERSIST as it was laid out on the bench in the laboratory. In this section I will describe the components of the PERSIST prototype. I will also explain in steps how PERSIST works as light passes through each optical component.

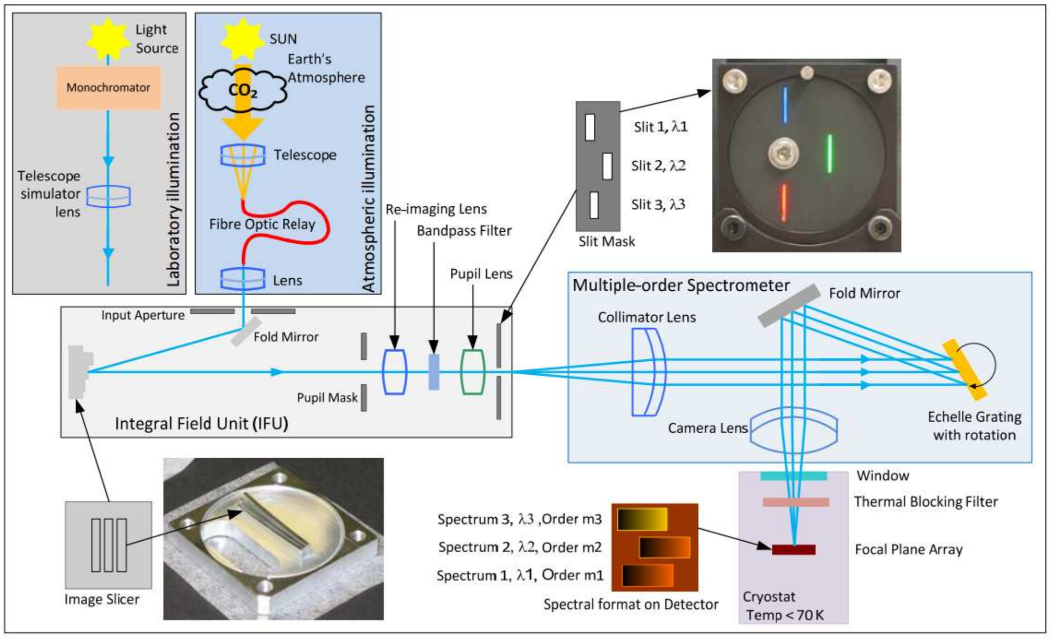

Figure 4.3: Schematic of the optical layout of PERSIST in the lab.

Light source

A light source is used to act as an input to the PERSIST instrument for my tests. I used a number of light sources for difference purposes. The primary light source was an Apex Illuminator with a Quartz Tungsten Halogen Lamp. It was beneficial to use this light source as the output of the lamp is very stable, allowing accurate comparisons of throughput through each of the spectral channels of PERSIST. The top left panel of Figure 4.3 also shows the schematic of the setup for observing atmospheric spectra. An optical fibre was used to relay light from a telescope focused on the sun to the input of PERSIST.

Telescope simulator

The PERSIST telescope simulator is the made up of a 150mm focal length collimator lens, an aperture stop, and a 300mm focal length camera lens. The collimator directs the incoming light into the instrument. The aperture can be opened or closed to control the amount of light entering the system, however this affects the image quality. The camera lens focuses the light onto the input aperture of the IFU.

Integral Field Unit

The IFU is made up of an entrance aperture, an input fold mirror, an aluminium image slicer with 3 off-axis slices, a set of three band pass filters, a set of re-imaging lenses and finally a slit mask containing three output slit apertures. The input fold mirror directs the light onto the image slicer. The image slicer is made up of three slices each tilted at a slightly different angle which splits the field of view contained in the incoming light beam into three, one for each wavelength channel. The band pass filters cut off light outside of the bandwidth of each wavelength channel. The expected bandwidth differs for each channel, 16 nm, 15 nm and 17 nm for the 1600 nm, 1020 nm and 2000 nm channels respectively. The transmittance through the band pass filters are also different, where the 2000 nm wavelength has the lowest transmittance.

Bench spectrometer

The spectrometer used in PERSIST was made up using off the shelf components which significantly limited the spectral resolution of the instrument. However for proof of concept of PERSIST it was sufficient. The bench spectrometer was made up of a collimator lens, a multiple diffraction order grating, a fold mirror and a camera lens. Upon leaving the output slit of the IFU, the collimator lens focuses the light from each wavelength channel onto the diffraction grating. It is subsequently directed from the fold mirror through the camera lens which projects the image into the cryostat where the instrument detector is housed.

A spectrometer that uses multiple diffraction orders allows the simultaneous diffraction of multiple wavelengths onto the detector. This can only work if the diffraction orders and wavelengths satisfy the following condition:

$$m_1\lambda_1 = m_2\lambda_2 = m_3\lambda_3 = k \tag{4.1}$$

where k is a constant. As it is unlikely to find an exact solution, an error term, Δm is added to each diffraction order:

$$(m_1 + \Delta m_1)\lambda_1 = (m_2 + \Delta m_2)\lambda_2 = (m_3 + \Delta m_3)\lambda_3 = k \tag{4.2}$$

The best solution results in the minimum value of the sum of the Δ_m error terms. The use of the multiple order diffraction grating increases the probability of ghost images propagating in the system. A ghost image is an image which arrives on the detector as a result of internal reflections within the system after the light has been split into diffraction orders. It typically appears as a lower intensity version of one of the spectra on the detector.

Cryostat and detector

Finally the images from each channel arrives onto the detector housed in the cryostat. The detector was a Raytheon VIRGO-2 detector, with a standard resolution of 2048×2048 pixels. However for PERSIST, only one half of the detector was utilised. As the detector was only sensitive to light in the range of 800-2500 nm, it was not possible to use the 765 nm channel (typically used to infer XCO_2) in the PERSIST prototype. The cryostat was cooled to $\sim$50K and a thermal blocking filter was placed at the entrance in order to reduce the thermal background and noise on the detector.

4.3 Test Results

Table 4.3 summarises the series of experiments performed with the PERSIST instrument during the project. The results of the tests are compared with the expected results from the computer simulated instrument in the initial study. Next I will discuss the outcome of the tests in more detail.

Input Light Source	**Tests Performed**
Apex Illuminator and optical fibre (monochromatic)	Used to focus instrument, optimised in the spatial direction
Apex Illuminator (monochromatic)	Wavelength scan to determine bandwidth, dispersion and check for light leaks
Apex Illuminator (monochromatic)	Adjustment of PERSIST alignment to avoid overlap of spectra and dead pixels and move position of ghost image
Apex Illuminator (white light)	Simultaneous illumination of three spectra to measure scattered light performance
Integrating sphere (uniform white light)	Simultaneous illumination of three spectra to measure scattered light performance
Halogen-Argon lamp and optical fibre	Used to measure spatial and spectral resolution of 1020 nm band
The Sun via external telescope and optical fibre	Used to record an example atmospheric spectrum in the 1020 nm channel

Table 4.2: PERSIST performance tests

4.3.1 Illumination with monochromatic light

The first set of tests conducted with the PERSIST instrument used a monochromatic source of light. The monochromator provides an input with a variable but accurately known wavelength which can be used to calibrate the PERSIST instrument. Initially I used an optical fibre to produce a small image on the detector which could be used to focus the instrument. Next I illuminated one of the channels with an Apex illuminator and monochromator. By gradually changing the wavelength of the monochromator input, a series of calibration images could be taken with PERSIST to calculate: the operational wavelength range of each of the three wavelength channels (bandwidth), the central wavelength of each channel, the dispersion, and the spectral slope. An advantage of using monochromatic light is that it also enables the identification of the wavelengths of any light leaks or stray light present in the instrument.

Figure 4.4 shows an example image taken at 1600 nm. The image on the left shows the full detector image prior to processing. Spatial and spectra information on the detector is shown from top to bottom and left to right respectively. The image of the monochromator output slit is the bright orange area in the top centre. The darker orange, semi-circular shape covering most of the detector is a result of thermal background light emitted within the instrument itself. The black patches, for example near to the centre of the detector image, are areas of dead pixels. It can be seen that the only light on the detector other than the background light is in the 1600 nm channel as expected. No light leaks of >0.1% were found in the instrument when testing any of the three channels indicating that the filters in the instrument only transmit the wavelengths corresponding to their band pass.

In the photo on the right, I focus in on the monochromator image in the 1600 nm channel. This is image was processed to remove the thermal background. In

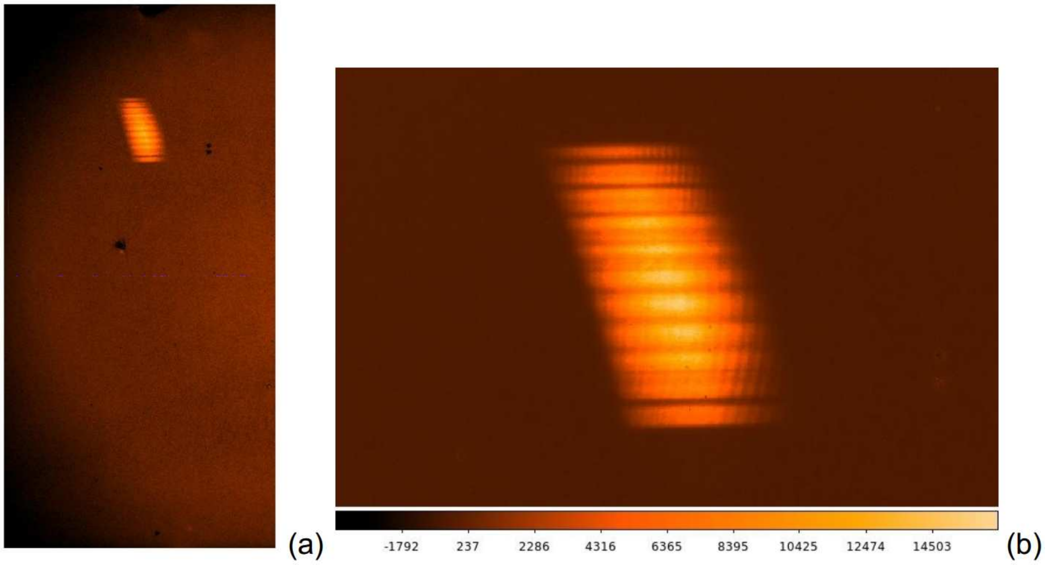

Figure 4.4: PERSIST images taken with monochromatic illumination. Image (a) shows the full detector image of 1024×2050 pixels while image (b) shows an enlarged view of the image of the monochromator slit.

order to remove the thermal background, I take the mean of 10 images taken with the monochromator switched off and subtract this from the image with the monochromator switched on, resulting in a much cleaner image with a stronger signal-to-noise ratio. The width of the monochromator image is determined from the band pass of the monochromator. It can be seen that the image is sloped. This is a result of a small shift in wavelength along the length of the monochromator slit, where the top of the slit emits light at a slightly shorter wavelength than the bottom of the slit. The striped structure in the image is spatial information carried through the instrument from the coils in the filament lamp light source. I repeated these tests for each channel where the results are summarised in Table 4.3.1. There are minor differences between the expected values and the values determined from the tests of central wavelength, dispersion and bandwidth. The difference in central wavelength and bandwidth as a result of the accuracy of the wavelength cut-off filter. The dispersion is different as a side effect of the diffraction grating being tilted to prevent ghost images from appearing on the detector.

Channel	**Parameter**	**Expected**	**Test Result**
1600 nm	Central Wavelength	1600 nm	1605.46 nm
	Dispersion	3.81 nm/mm	4.33 nm/mm
	Bandwidth	16 nm	16.29 nm
	Spectral Slope	NA	6.58 nm
	Length of slit image	333 pixels	322 pixels
	Light leaks	NA	<0.1%
1020 nm	Central Wavelength	1020 nm	1020.68 nm
	Dispersion	2.38 nm/mm	2.63 nm/mm
	Bandwidth	15 nm	13.81 nm
	Spectral Slope	NA	6.62 nm
	Length of slit image	333 pixels	335 pixels
	Light leaks	NA	<0.1%
2000 nm	Central Wavelength	2000 nm	2004.11 nm
	Dispersion	4.76 nm/mm	5.26 nm/mm
	Bandwidth	17 nm	16 nm
	Spectral Slope	NA	9.26 nm
	Length of slit image	333 pixels	321 pixels
	Light leaks	NA	<0.1%

Table 4.3: Monochromator test results.

4.3.2 Illumination with filament image

In the next test, the monochromator was removed and the Apex illuminator was used to illuminate the PERSIST input field of view directly. As the light source is no longer wavelength specific, all three slices in the IFU were simultaneously illuminated with white light that covers all the wavelengths to which the instrument detector is sensitive. In effect, this test is a simulation of illuminating PERSIST with an Earth Observation scene. Figure 4.5 shows the result of this test, where the left image has a linear scale and the the right image uses a logarithmic scale. In both cases the thermal background was removed using the method described in the previous section. The primary aim of this test was to show that the PERSIST instrument could simulateously record three spectra, one in each wavelength channel. This test is a clear success, although the Apex illuminator only illuminates a fraction of the full length of the slice. The right hand image in Figure 4.5 uses a logarithmic scale to emphasise the presence of scattered light between the spectra. This is primarily noticeable about the 1020 nm and 1600 nm spectra. The spectra on the detector are as follows: 1600 nm (top), 1020 nm (middle) and 2000 nm (bottom). It is clear that the 2000 nm spectrum has a significantly lower intensity than the 1600 nm and 1020 nm spectra. This is a result of the thermal blocking filter in the entrance to the thermostat which has a lower transmittance at 2000 nm.

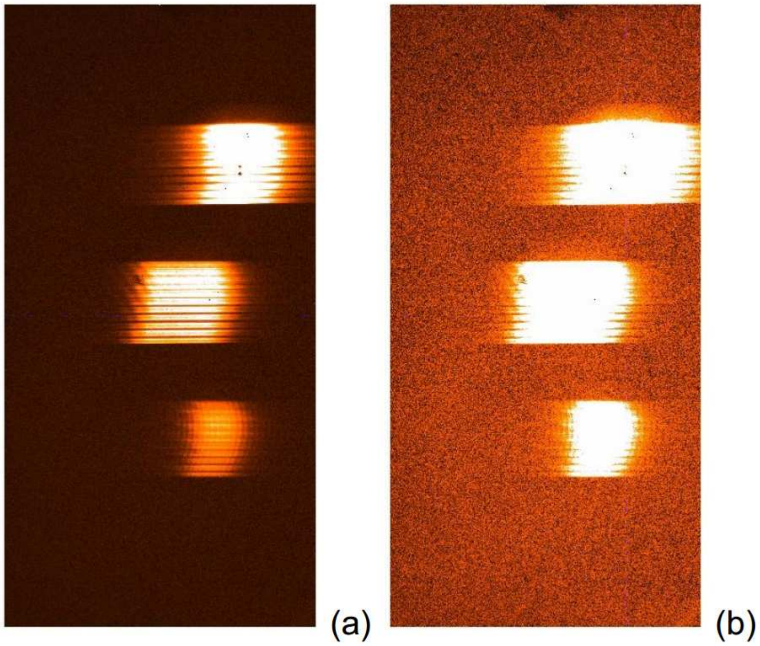

Figure 4.5: PERSIST image recorded with direct illumination of the input field of view using the Apex illuminator. Image (a) uses a linear scale of intensity showing the 1600 nm (top), 1020 nm (middle) and 2000 nm (bottom) channels on the detector while image (b) uses a logarithmic scale. The logarithmic scale highlights areas of scattered light between the spectra, for example the large area of scatter light above the 1600 nm spectra.

4.3.3 Uniform Illumination

I used two light sources to provide uniform illumination of the PERSIST field of view: illumination from the Apex illuminator and illumination with an integrating sphere. An integrating sphere is an optical component with a hollow spherical cavity covered with a diffuse, white, reflective coating. The Apex illuminator is directed into to the side part of the integrating sphere, with an output port illuminating the PERSIST field of view. The integrating sphere provides more uniform illuminating than the Apex illuminator as the spatial information in the light entering the sphere becomes very diffuse. For the next sets of tests, we changed the PERSIST alignment in order to move the position of the spectra on the detector, such that they did not overlap with the areas of dead pixels near to the centre of the detector. In doing so, a ghost image appeared on the detector to the right of the 1020 nm spectrum. We further adjusted the PERSIST alignment so that that I could also measure the intensity of the ghost image.

White light illumination

In order to create a more uniform illumination, the Apex illuminator was defocused, to partially remove the spatial information from the filament lamp, however some of the filament structure still remained. With the Apex illuminator defocused, it now illuminates the entirety of the available space on the image slicer in the IFU. The result of this test is shown in Figure 4.6. Note that the images in each channel are now significantly longer in the spatial direction on the detector. The left panel shows the image without the thermal background removed, while the middle and right hand images show the spectra with the thermal background removed for linear and logarithmic intensity scales respectively. The thin strip of light on the right hand side is the ghost image of the 1020 nm spectrum.

The ghost image is a side effect of using a diffraction grating with multiple orders propagating through the system. A series of internal reflections in the system result in the ghost image arriving on the detector. The 8th diffraction order is the most important for the 1020 nm channel, but several other orders propagate through the system with efficiencies of up to 20%. The intensity of the ghost image was ~6% of the peak intensity of the 1600 nm spectrum. This is not significant if there is substantial distance between the ghost image and the science spectra.

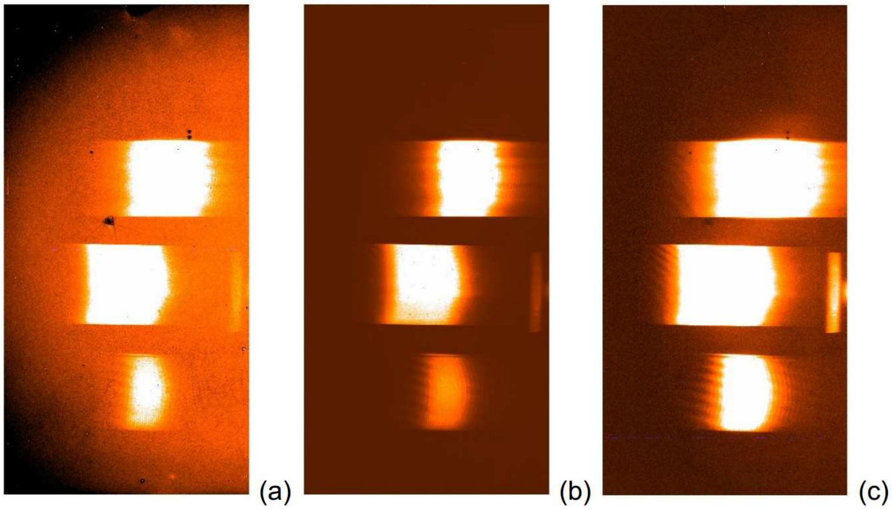

Figure 4.6: PERSIST image recorded with flat-field illumination from the Apex illuminator. Image (a) shows the unprocessed image with linear intensity scaling. Images (b) and (c) show the result having removed the thermal background using linear and logarithmic scaling respectively.

The intensity plot shown in Figure 4.7 shows the brightness of each spectrum and the relative brightness of the scattered light between them. Figure 4.8 is a schematic diagram showing each of the features on the detector image in Figure 4.6, where Table 4.3.3 shows the relative intensities of the features with respect to the 1600 nm spectrum. The differences in intensity between the left hand corner regions (A and C) and the right hand corner regions (B and D) are due to the thermal background.

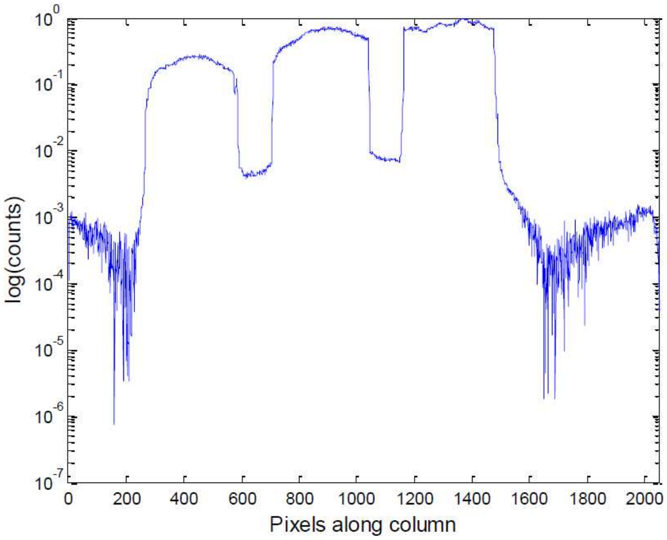

Figure 4.7: Plot of intensity vs. position (logarithmic scale) for a spatial cut through the white light image shown in Figure 4.6.

I find that the intensity of the scattered light between the spectra is in the region of ~1.5% or less. This result is consistent with the expected values given the components used in the PERSIST prototype. However, it is expected that this can be improved by at least a factor of ten by using higher specification optical components as would be the case in a funded space-based mission.

Even with a factor of ten improvement, the amount of scattered light between the spectra introduces the risk of cross-talk between spectra. Cross-talk is an overlap of the information contained within the individual spectra, and would result in significant degradation to the scientific quality of the image. Characterisation and reduction of scattered light within the system is therefore essential for reduction of potential XCO_2 errors resulting from cross-talk.

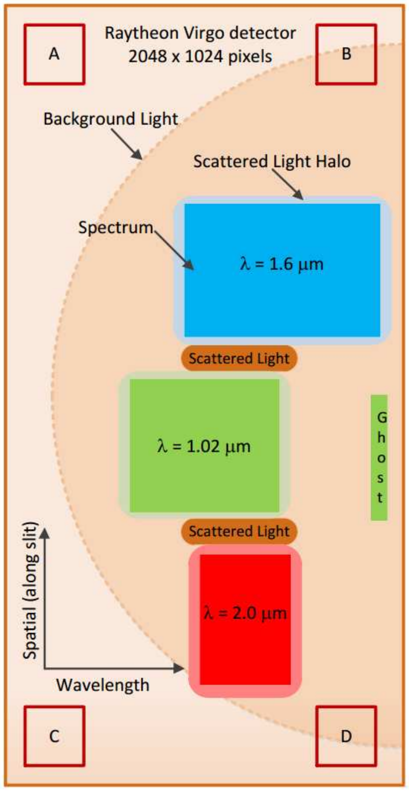

Figure 4.8: Schematic of the image as it is layed out on the PERSIST detector.

Area on detector	**Relative intensity**
1600 nm	1.0000
1020 nm	0.6527
2000 nm	0.1669
Ghost	0.0597
SL1	0.0139
SL1	0.0089
A	0.0000
B	0.0018
C	0.0000
D	0.0017

Table 4.4: Relative intensities of different regions on the detector defined in the schematic in Figure 4.8 and in reference to the detector image shown in Figure 4.6.

Integrating sphere

The integrating sphere provides a more uniform illumination of the PERSIST field of view when compared with the defocused Apex illuminator. The result of this test is shown in Figure 4.9 and shows spatially uniform spectra. The intensity of illumination through the integrating sphere is sufficient for the 1020 nm and 1600 nm channels, but the 2000 nm channel which already had low transmission through the instrument optics is very faint. This was a result of the low reflectivity of the coating inside the integrating sphere at this wavelength.

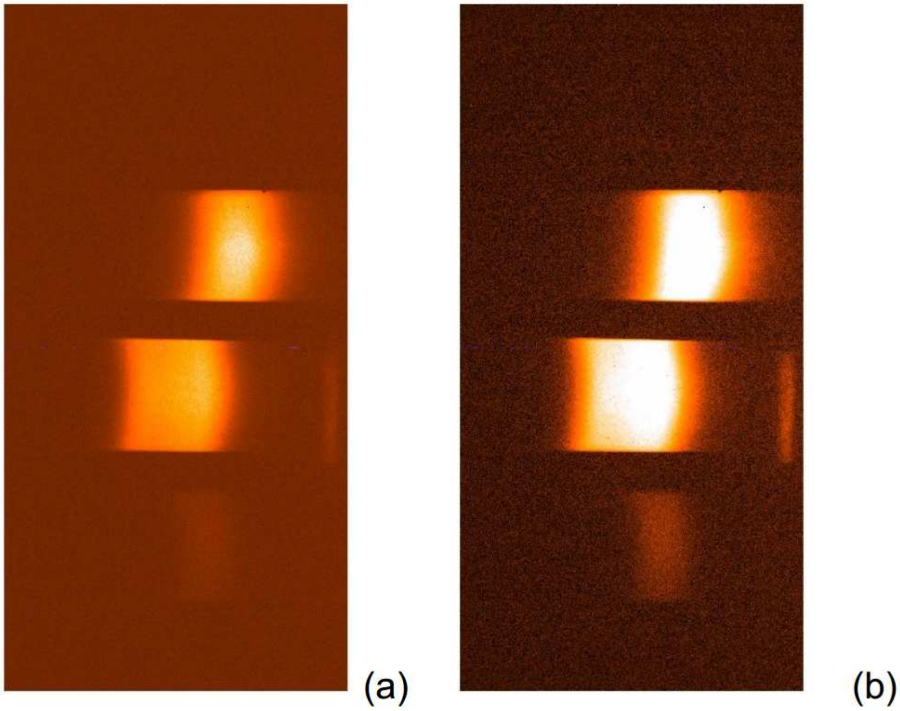

Figure 4.9: PERSIST image recorded with flat-field illumination from an integrating sphere. Image (a) shows the result following the removal of the thermal background with a linear intensity scale, while image (b) shows the same image with a logarithmic scale to show the 2μm channel more clearly.

4.3.4 Spectral Resolution

I determined the spatial and spectral resolution of the instrument in the 1020 nm channel. I used a Mercury-Argon gas discharge lamp with spectral emission lines at very specific wavelengths - this image is shown in Figure 4.10. The only emission line visible in the 1020 nm channel was at a wavelength of 1013.975 nm due to the bandwidth of the channel. The resolution of the instrument was determined by calculating the full-width half-maximum (FWHM) of the image in the spatial and spectral direction. The FWHM in the spectral dimension was approximately 7.3 pixels. I calculate the spectral resolution using $R=\lambda/\Delta\lambda$ where $\lambda=1013.975$ nm is the wavelength of the emission line and $\Delta\lambda$ is the FWHM in nm determined from the dispersion in the 1020 nm channel. The PERSIST spectral resolution was 2760. As the instrument was optimised for spatial resolution, the FWHM in the spatial direction of approximately 1.7 pixels. This indicates that significantly higher spectral resolution could be obtained given optimisation for spectral rather than spatial resolution. As expected, no emission lines were observed in the 1600 nm and 2000 nm channels.

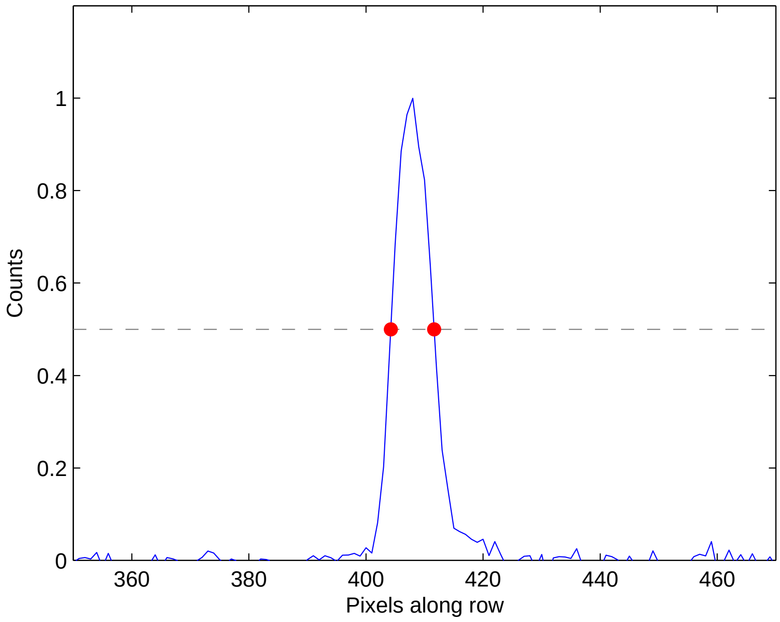

Figure 4.10: PERSIST image recorded with illumination from a Mercury-Argon gas discharge lamp at 1013.975 nm (linear intensity scale). Dashed line and red points show full width half maximum of intensity. Note I only show a small section of the detector.

4.3.5 Solar illumination

The final experiment performed with PERSIST was an attempt to measure an atmospheric spectrum using a small telescope set-up outside the laboratory. The telescope was directed towards the sun, and an optical fibre was used to illuminate the PERSIST field of view. The optical fibre used for the observations had a core diameter of 50μm, which should produce a corresponding image size of 1.4 pixels on the detector. However I measured the fibre image to have a FWHM of 3.5 pixels, a factor of 2.5 times larger than the expected size. This is a reflection of the end to end aberrations in the system optics. Figure 4.3.5 shows the most successful atmospheric measurement I was able to take in the time I had at the end of the project.

The top left image in the figure shows the appearance of the spectrum on the detector. The middle left panel shows the measured spectrum (blue line) having removed the thermal background, and the spectrum of a Tungsten-Halogen lamp (red line) used for calibration of the atmospheric spectrum. By removing the red curve I determine the atmospheric spectrum (middle right). The bottom left image is a simulated spectrum taken at the same time as the atmospheric spectrum, such that the solar zenith is equivalent. In order to make a better comparison with the observed spectrum, the high resolution simulated spectrum was convolved with a smooth gaussian curve to degrade it to the same spectral resolution as PERSIST. In general, the observed spectrum is quite poor, but there are certainly some recognisable lines when comparing with the simulated spectrum.

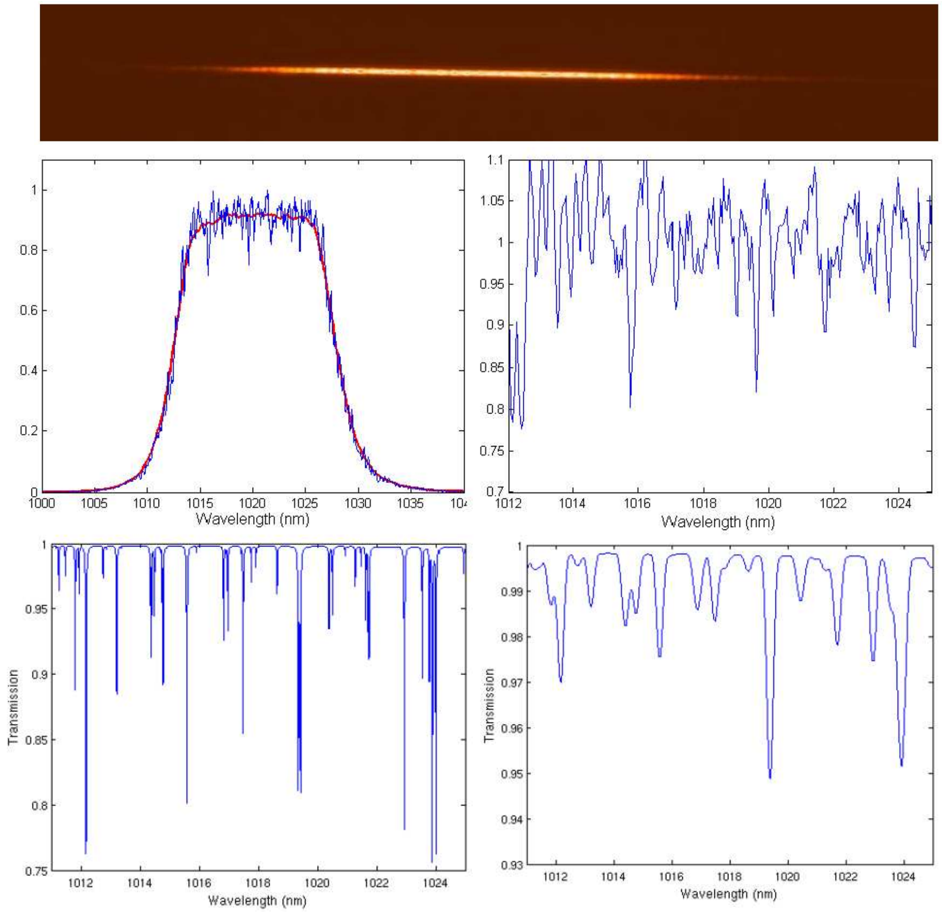

Figure 4.11: The top and middle left images show the atmospheric spectrum measured in the 1020 nm channel. The blue line in the middle left image shows the atmospheric spectrum, while the red line shows a spectrum of a Tungsten-Halogen lamp which was used for calibration of the atmospheric spectrum. The middle right image shows the extracted spectrum after calibration with the lamp spectrum. The bottom left image shows the simulated spectrum and the bottom left shows the simulated spectrum degraded to the spectral resolution of PERSIST.

4.3.6 Stray Light

Stray light represents a significant source of error for XCO_2 concentrations inferred using atmospheric spectra. I found stray light between spectra measuring up to ~1.5% of the peak intensity on the detector. Although it is expected that this can be reduced by at least a factor of ten by improving the optics in the system, it is important to characterise the error introduced by cross-talk. To do this, I performed some simple tests using simulated atmospheric spectra and a radiative transfer model (Natraj *et al.*, 2008). I simulated spectra measured from an instrument with equivalent performance characteristics to those shown in Table 4.1 (Lee *et al.*, 2011). Simulated stray light was then added to individual simulated spectra as a % of the peak intensity of the spectra, and simultaneously to all spectra.

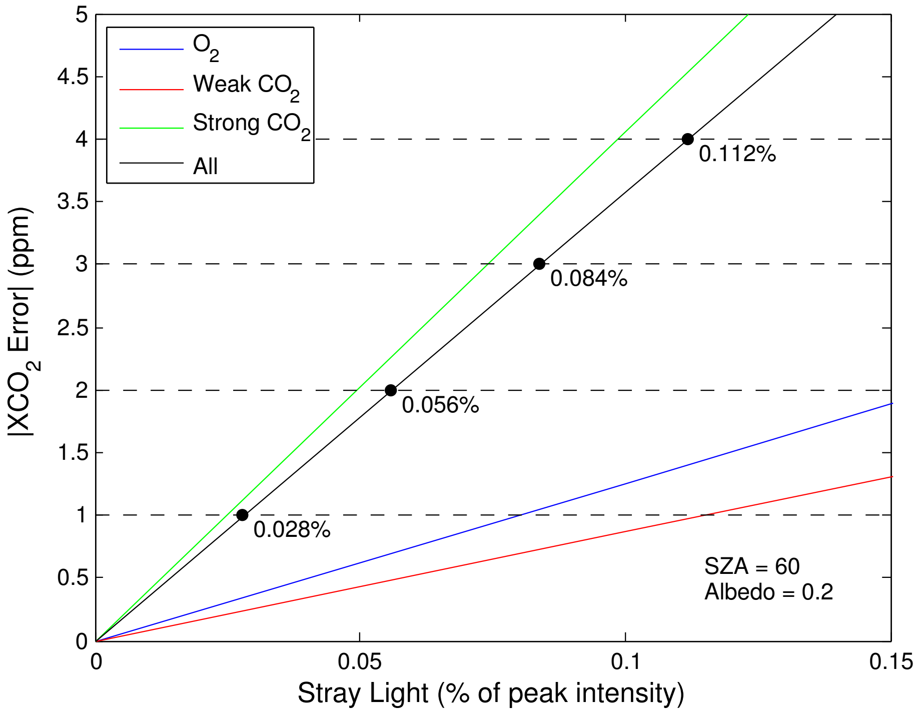

Figure 4.12: Absolute error in XCO_2 (ppm) as a function of stray light intensity in each wavelength channel where stray light is given as a % of the channels peak intensity.

Figure 4.12 shows the absolute XCO_2 error introduced by retrieving an XCO_2 concentration from atmospheric spectra simulated assuming a standard measurement scenario with a solar zenith angle (SZA) of 60° and a surface albedo of 0.2, with the addition of various levels of stray light. I also assumed that no aerosols or clouds were present. The largest XCO_2 error came from the Strong CO_2 band which was the most sensitive waveband to the addition of stray light. Stray light in the Strong and Weak CO_2 bands introduced a negative error, while stray light added to the O_2 band created a positive error. Assuming the presence of stray light in all spectra, this test indicated that cross-talk would need to be below 0.028% of peak intensity in order to retrieve an XCO_2 concentration with an error of <1ppm. The stray light performance of PERSIST would have to be improved by a factor of 50 in order to produce an acceptable level of XCO_2 error. It may also be necessary to increase the distance between spectra. This imposes stringent requirements on the optical design of the instrument. Substantially more detailed tests under a large range of conditions would be required to fully characterise XCO_2 errors from cross-talk.

4.4 Summary

The main goals of PERSIST were to demonstrate the ability of the instrument to simultaneously record three spectra in multiple wavelength ranges on the same detector. I performed a series of experiments using the bench spectrometer, working within its limitations.

I showed that the spectrometer could cleanly capture three spectra at the wavelengths of 1020 nm, 1600 nm and 2000 nm. The 1020 nm waveband replaced the nominal 765 nm waveband as the Virgo detector was not sensitive to this wavelength region. The level of scattered light between spectra was $\sim$1.5% introducing possible cross-talk. I simulated atmospheric spectra measurements and contaminated them with stray light to determine the sensitivity of XCO_2 retrievals to the presence of cross-talk. I found that stray light would have to be reduced by a factor of $\sim$50 relative to the stray light performance of the PERSIST prototype in order to reduce the XCO_2 error to $<$1ppm. However only a simple test was performed and range of measurement scenarios need to be considered. The stray light can be reduced by improving the optical components of the system. I tried to take an example measurement of atmospheric spectra, which I successfully did so for the 1020 nm channel. Although the measured spectra showed similar features to an equivalent simulated spectra, it was generally very poor due to the low spectral resolution of the prototype instrument. The spectral resolution can easily be improved by using higher end optical components and optimising the system for spectral rather than spatial resolution.

The primary benefits of PERSIST were that it could theoretically achieve similar performance targets to those of OCO, but in a more compact system, resulting in a significant saving in cost and weight. Theoretical designs by the ATC show using multiple IFUs in one CO_2 instrument would enable significant improvements in signal-to-noise and spectral resolution due to longer exposure times.

Chapter 5

Outlook

5.1 Discussion of Future Work

The two key objectives of this thesis are to: (1) improve understanding of recent variability in observed CO_2 and CH_4 concentrations in the high latitudes (2) develop a novel instrument capable of observing the atmospheric spectra necessary to infer XCO_2, where XCO_2 can be used to provide further constraints on the carbon cycle.

5.1.1 Chapter 2

In Chapter 2 I showed that there have been substantial changes in the high-latitude CO_2 seasonal cycle over the past 40 years. I characterised the errors propagating into the seasonal cycle trend analysis resulting from the effects of aliasing, a direct consequence of detrending the data. More complex statistical analyses could be done using this type of characterisation in order to improve our understanding of aliasing effects on observed seasonal cycle variability. An atmospheric transport model would be useful for this analysis. For example, it would account for changes in atmospheric transport, as this was neglected by the simple box model used in my study. A useful experiment would be to start with a model run with variable meteorology but prior CO_2 emissions that are constant from year-to-year. A subset of regions can be defined according to the dominant vegetation type (e.g. boreal, mid-latitude temperate). A trend could then be introduced to, for example, the spring-time onset of uptake by boreal vegetation. Time series of CO_2 would be sampled at the grid points nearest to existing surface monitoring sites to act as pseudo measurements. This would be done for a range of trend scenarios in order to test the detectability of trends and aliasing effects in the resulting time series.

For CO_2, there is a clear requirement to understand the recent changes at the edges of the carbon uptake period. In particular, increased autumn release of CO_2 in response to warmer autumn temperatures does not appear to be well understood in the literature. Process-based models, which produce estimates of NEE based on changes in photosynthesis and respiration driven by climate variables, do not appear to capture the observed variability on large scales. Determining the sensitivity of either edge of the growing season to rapidly warming temperatures is key to determining the future carbon balance of the northern hemisphere.

5.1.2 Chapter 3

In Chapter 3 I presented an analysis of high-latitude CH_4 surface concentrations to test my hypothesis that recent observed changes in the seasonal cycle amplitude measured at high-latitude CH_4 monitoring sites could be a result of a change in wetland emissions. A key result is that it was non-trivial to detect increases in wetland emissions in the high-latitude time series until the year-to-year trend in emissions became very large. Some components of the analysis are still not understood. For example, I showed that atmospheric transport resulted in a trend in the seasonal amplitude at ALT. To determine the fractional contribution of atmospheric transport to the amplitude trend at BRW, it is key to extend the TM5 model output to cover the full time span of BRW time series. Improved model priors will result in more accurate seasonal cycles in the control simulation which will improve the overall interpretation based on the study of the TM5 model output. A simultaneous analysis of growth rates and seasonal cycles could provide more clarity when interpreting the high-latitude data. For example, latitudinal gradients of the atmospheric CH_4 growth rate determined from the broad-scale surface network can provide information about the relative timing of increases in CH_4 concentration. It would aid source attribution if this was consistent with changes in amplitude at a site which is particularly sensitive to wetland changes, such as BRW. Further work could also be done to find locations for new monitoring sites in the Arctic which would be more sensitive to large-scale changes in CH_4 wetland emissions.

5.1.3 Chapter 4

In Chapter 4, I presented the results of laboratory tests of a prototype Earth observing instrument for CO_2. Although the initial study of PERSIST was a success, it is only at the proof of concept stage. The next stage would be to develop a more advanced prototype with higher specification optics and increased spectral resolution. This would allow the measurement of atmospheric spectra in order to show that the instrument can meet the science requirements for a space-based CO_2 mission. A key area of study for the PERSIST instrument is the further characterisation of stray light and cross-talk as this represents a significant source of error when retrieving XCO_2 concentrations. Cross-talk is a particular problem for PERSIST which captures multiple spectra on the same detector.

A significant disadvantage of passive instruments such as PERSIST, TANSO and OCO is that they cannot monitor high-latitude surface fluxes during the winter months. This is because they depend on the presence of reflected sunlight, which is not present during the night or at high latitudes during the winter months. It is quite clear from my work in chapters 2 and 3 that the ability to monitor the seasonal cycle of these gases can provide important information about carbon cycle processes. Active instruments represent a possible solution to this. An example of an active instrument is the DIfferential Absorption Lidar (DIAL). This instrument uses two lasers with different wavelengths, which are selected such that one of the wavelengths is absorbed by the molecule of interest while the other wavelength is not. The difference in intensity between the two signals is used to infer the atmospheric concentration of the gas. Active methods can determine XCO_2 and XCH_4, day or night, and throughout the entire year. For this reason, it would be highly beneficial to use observations from a DIAL instrument in conjunction with atmospheric inversion methods for the purpose of estimating high-latitude carbon fluxes. Active instruments have a lower spatial resolution than passive instruments, which means that they are less effective at locating point sources of greenhouse gases.

An example of a current proposed mission concept using an active system is the NASA Active Sensing of CO_2 Emissions over Nights, Days and Seasons (ASCENDS) mission. ASCENDS will provide extended CO_2 remote sensing capability during all seasons and times of day, and will be able to monitor high-latitude XCO_2 concentrations, including those over permafrost regions. Depending on the Earth orbit chosen for the mission, more emphasis can be placed on monitoring diurnal or seasonal cycles of vegetation to help understand underlying biological processes. Kawa *et al.* (2010) performed simulation studies using an instrument with the same performance criteria as ASCENDS. They showed that it was not only possible to meet these science requirements, but also that such a mission would provide significant insights into carbon cycle science. In conjunction with an improved distribution of ground-based measurement sites, active space-based missions such as ASCENDS will play a key role in constraining high-latitude surface fluxes of greenhouse gases such as XCO_2 and XCH_4. This will aid in understanding the high-latitude response to the carbon-climate feedback.

5.1.4 Final Comments

This thesis has laid the foundations that will help determine the scientific requirements for future greenhouse gas space-borne mission concepts. An important next step is to translate the surface variations in CO_2 and CH_4 that have been observed in the surface data to associated variations in atmospheric column observations. An atmospheric transport model in conjunction with an Observing System Simulation Experiment (OSSE) could be used for this analysis. An OSSE is used to simulate space-borne measurements of XCO_2 based on the characteristics of a specific instrument. This experiment follows my suggested model experiment in 5.1.1 where I suggested introducing trends to regional carbon fluxes in order to test the detectability of the trends using ground-based observations. In this case, I would try to detect the same variability using the simulated space-based instrument. It is anticipated that due to the low spatial and temporal variability in XCO_2 relative to surface concentrations of CO_2, an instrument would have to satisfy very high precision requirements in order to observe changes in the seasonal cycle.

References

Archer, D. (2007). Methane hydrate stability and anthropogenic climate change. *Biogeosciences*, **4**, 521–544.

Archer, D., Eby, M., Brovkin, V., Ridgwell, A., Cao, L., Mikolajewicz, U., Caldeira, K., Matsumoto, K., Munhoven, G., Montenegro, A. and Tokos, K. (2009). Atmospheric Lifetime of Fossil Fuel Carbon Dioxide. *Annu. Rev. Earth Planet. Sci.*, **37**, 117–134.

Bacastow, R.B., Keeling, C.D. and Whorf, T.P. (1985). Seasonal amplitude increase in atmospheric CO_2 concentration at Mauna Loa, Hawaii, 1959 - 1982. *J. Geophys. Res.*, **90**, 10529–10540.

Ballantyne, A.P., Alden, C.B., Miller, J.B., Tans, P.P. and White, J.W.C. (2012). Increase in observed net carbon dioxide uptake by land and oceans during the past 50 years. *Nature*, **488**, 70–72.

Barichivich, J., Briffa, K.R., Osborn, T.J., Melvin, T.M. and Caesar, J. (2012). Thermal growing season and timing of biospheric carbon uptake across the northern hemisphere. *Global Biogeochem. Cycles*, **26**.

Barichivich, J., Briffa, K.R., Myneni, T.J., R. B. Osborn, Melvin, T.M., Ciais, P., Piao, L. and Tucker, C. (2013). Large-scale variations in the vegetation growing season and annual cycle of atmospheric co_2 at high northern latitudes from 1950 to 2011. *Glob. Change Biol.*, **19**, 3167–3183.

Bergamaschi, P., Krol, M., Dentener, F., Vermeulen, A., Meinhardt, F., Graul, R., Ramonet, M., Peters, W. and Dlugokencky, E.J. (2005). Inverse modelling of national and European CH_4 emissions using the atmospheric zoom model TM5. *Atmos. Chem. Phys.*, **5**, 2431–2460.

Biastoch, A., Treude, T., Rüpke, L.H., Riebesell, U., Roth, C., Burwicz, E.B., Park, W., Latif, M., Böning, C.W., Madec, G. and Wallmann, K. (2011). Rising Arctic Ocean ttemperature cause gas hydrate destabalization and ocean acidification. *Geophys. Res. Lett.*, **38**.

Blake, D.R., Mayer, E.W., Tyler, S.C., Makide, Y., Montague, D.C. and Rowland, F.S. (1982). Global increase in atmospheric methane concentrations between 1978 and 1980. *Geophys. Res. Lett.*, **9**, 477–480.

Bloom, A., Palmer, P.I., Fraser, A., Reay, D.S. and Frankenberg, C. (2010). Large-Scale Controls of Methanogenesis Inferred from Methane and Gravity Spaceborne Data. *Science*, **327**, 322–325.

Bousquet, P., Ringeval, B., Pison, I., Dlugokencky, E.J., Brunke, E.G., Carouge, C., Chevallier, F., Fortems-Cheiney, A., Frankenberg, C., Hauglustaine, D.A., Krummel, P.B., Langenfelds, R.L., Ramonet, M., Schmidt, M., Steele, L.P., Szopa, S., Yver, C., Viovy, N. and Ciais, P. (2011). Source attribution of the changes in atmospheric methane for 2006–2008. *Atmos. Chem. Phys.*, **11**, 3689–3700.

Bruhwiler, L., Dlugokencky, E., Masarie, K., Ishizawa, M., Andrews, A., Miller, J., Sweeney, C., Tans, P. and Worthy, D. (2014). CarbonTracker-CH_4: an assimilation system for estimating emissions of atmospheric methane. *Atmos. Chem. Phys.*, **14**, 1–25.

Canadel, J.G., Le Quere, C., Raupach, M.R., Field, C.B., Buitenhuis, E.T., Ciais, P., Conway, T.J., Gillett, N.P., Houghton, R.A. and Marland, G. (2007). Contributions to accelerating atmospheric CO_2 growth from economic activity, carbon intesity, and efficiency of natural sinks. *PNAS*, **104**, 18866–18870.

Chevallier, F., Engelen, R.J. and Peylin, P. (2005). The contribution of airs data to the estimation of CO_2 sources and sinks. *Geophys. Res. Lett.*, **32**.

Connor, B.J., Böesch, H., Toon, G., Sen, B., Miller, C. and Crisp, D. (2008). Orbiting Carbon Observatory: Inverse method and prospective error analysis. *J. Geophys. Res.*, **113**.

Conny, J.M. and Currie, L.A. (1996). The isotopic characterization of methane, non-methane hydrocarbons and formaldehyde in the troposphere. *Atmos. Environ.*, **30**, 621–638.

Corell, R.W., Hassol, S.J., Melilo, J.M., Archer, D., Euskirchen, E., Chapin, F.S., McGuire, A.D., Christensen, T.R., Fichelet, V.P. and Walter, K. (2008). Methane from the Arctic: global warming wildcard. *UNEP Year Book 2008. Edited by Harrison, P. United Nations Environment Programme*, 37–48.

Cox, P.M., Pearson, D., Booth, B.B., Friedlingstein, P., Huntingford, C., Jones, C.D. and Luke, C.M. (2013). Sensitivity of tropical carbon to climate change constrained by carbon dioxide variability. *Nature*, **494**, 341–345.

Crisp, D., Atlas, R.M., Breon, F.M., Brown, L.R., Burrows, J.P., Ciais, P., Connor, B.J., Doney, S.C., Fung, I.Y., Jacob, D.J., Miller, C.E., O'Brien, D., Pawson, S., Randerson, J.T., Rayner, P., Salawitch, R.J., Sander, S.P., Sen, B., Stephens, G.L., Tans, P.P., Toon, G.C., Wennberg, P.O., Wofsy, S.C., Yung, Y.L., Kuang, Z., Chudasama, B., Sprague, G., Weiss, B., Pollock, R., Kenyon, D. and Schroll, S. (2004). The Orbiting Carbon Observatory (OCO) mission. *Adv. Space Res.*, **34**.

Dlugokencky, E., Lang, P.M., Crotwell, A.M., Masarie, K.A. and Crotwell, M.J.. (1983-2013). Atmospheric methane dry air mole fractions from the NOAA ESRL carbon cycle cooperative global air sampling network.

Dlugokencky, E.J., Steel, L.P., Lang, P.M. and Masarie, K.A. (1995). Atmospheric methane at Mauna Loa and Barrow observatories: Presentation and analysis of in situ measurements. *J. Geophys. Res.*, **100**, 23103–23113.

Dlugokencky, E.J., Masarie, K.A., Tans, P.P., Conway, T.J. and X., X. (1997). Is the amplitude of the methane seasonal cycle changing? *Atmos. Environ.*, **31**, 21–26.

Dlugokencky, E.J., Masarie, K.A., Lang, P.M. and Tans, P.P. (1998). Continuing decline in the growth rate of the atmospheric methane burden. *Nature*, **393**, 447–450.

Dlugokencky, E.J., Houweling, S., Bruhwiler, L., Masarie, K.A., Lang, P.M., Miller, J.B. and Tans, P.P. (2003). Atmospheric methane levels off: Temporary pause or a new steady-state? *Geophys. Res. Lett.*, **30**.

Dlugokencky, E.J., Myers, R.C., Lang, P.M., Masarie, K.A., Crotwell, A.M., Thoning, K.W., Hall, B.D., Elkins, J.W. and Steele, L.P. (2005). Conversion of NOAA atmospheric dry air CH_4 mole fractions to a gravimetrically prepared standard scale. *J. Geophys. Res.*, **110**.

Dlugokencky, E.J., Bruhwiler, L., White, J.W.C., Emmons, L.K., Novelli, P.C., Montzka, S.A., Masarie, K.A., Lang, P.M., Crotwell, A.M., Miller, J.B. and Gatti, L.V. (2009). Observational constraints on recent increases in the atmospheric CH_4 burden. *Geophys. Res. Lett.*, **36**.

Dlugokencky, E.J., Nisbet, E.G., Fisher, R. and Lowry, D. (2011). Global atmospheric methane: budget, changes and dangers. *Phil. Trans. R. Soc. A*, **369**, 2058–2072.

Ellwood, E.R., Temple, S.A., Primack, R.B., Bradley, N.L. and Davis, C.C. (2013). Record-Breaking Early Flowering in the Eastern United States. *PLoS ONE*, **8(1)**, e53788.

European Commission, J. (2009). Joint research centre (jrc)/netherlands environmental assessment agency (pbl). emission database for global atmospheric research (edgar), release version 4.0.

Feely, R., Doney, S. and Cooley, S. (2009). Ocean acidification: Present Conditions and Future Changes in a High-CO_2 World. *Oceanography*, **22**, 36–47.

Feng, L., Palmer, P.I., Yang, Y., Yantosca, R.M., Kawa, S.R., Paris, J.D., Matsueda, H. and Machida, T. (2011). Evaluating a 3-D transport model of atmospheric CO_2 using ground-based, aircraft, and space-borne data. *Atmos. Chem. Phys.*, **11**, 2789–2803.

Fisher, R.E., Sriskantharajah, S., Lowry, D., LanoisellÃČÂľ, M., Fowler, C.M.R., James, R.H., Hermansen, O., Lund Myhre, C., Stohl, A., Greinert, J., Nisbet-Jones, P.B.R., Mienert, J. and Nisbet, E.G. (2011). Arctic methane sources: Isotopic evidence for atmospheric inputs. *Geophys. Res. Lett.*, **38**, n/a–n/a.

Frankenberg, C., Aben, I., Bergamaschi, P., Dlugokencky, E.J., van Hees, R., Houweling, S., van der Meer, P., Snel, R. and Tol, P. (2011). Global column-averaged methane mixing ratios from 2003 to 2009 as derived from SCHIAMACHY : Trends and variability. *J. Geophys. Res.*, **116**.

Friedlingstein, P., Cox, P., Betts, R., Bopp, L., von Bloh, W., Brovkin, V., Cadule, P., Doney, S., Eby, M., Fung, I., Bala, G., John, J., Jones, C., Joos, F., Kato, T., Kawamiya, M., Knorr, W., Lindsay, K., Matthews, H.D., Raddatz, T., Rayner, P., Reick, C., Roeckner, E., K.-G., S., Schnur, R., Strassmann, K., Weaver, A.J., Yoshikawa, C. and Zeng, N. (2006). Climate-Carbon Cycle Feedback Analysis: Results from the C^4MIP Model Intercomparison. *J. Climate*, **19**, 3337–3353.

Frölicher, T., Joos, F., Raible, C.C. and Sarmiento, J.L. (2013). Atmospheric CO_2 response to volcanic eruptions: The role of ENSO, season variability. *Global Biogeochem. Cy.*, **27**, 239–251.

Gedney, N., Cox, P.M. and Huntingford, C. (2004). Climate feedback from wetland methane emissions. *Geophys. Res. Lett.*, **31**.

Gloor, M., Sarmiento, J.L. and Gruber, N. (2010). What can be learner about carbon cycle climate feedbacks from the CO_2 airborne fraction? *Atmos. Chem. Phys.*, **10**, 7739–7751.

Goode, P.R., Qiu, J., Yurchyshyn, V., Hickey, J., Chu, M.C., Kolbe, E., Brown, C.T. and Koonin, S.E. (2001). Earthshine observations of the earth's reflectance. *Geophys. Res. Lett.*, **28**, 1671–1674.

Graven, H.D., Keeling, R.F., Piper, S.C., Patra, P.K., Stephens, B.B., Wofsy, S.C., Welp, L.R., Sweeney, C., Tans, P.P., Kelley, J.J., Daube, B.C., Kort, E.A., Santoni, G.W. and Bent, J.D. (2013). Enhanced Seasonal Exchange of CO_2 by Northern Ecosystems Since 1960. *Science*, **341**, 1085–1089.

Gurney, K.R., Law, R.M., Denning, A.S., Rayner, P.J., Baker, D., Bousquet, P., Bruhwiler, L., Chen, Y.H., Ciasis, P., Fan, S., Yung, I.Y., Gloor, M., Heimann, N., Higuchi, K., John, J., Maki, T., Maksyutov, S., Masarie, K., Peylin, P., Prather, M., Pak, B.C., Randerson, J., Sarmiento, J., Taguchi, S., Takahashi, T. and Yuen, C.W. (2002). Towards robust regional estimates of CO_2 sources and sinks using atmospheric transport models. *Nature*, **415**, 626–630.

Harris, I., Jones, P.D., Osborn, T.J. and Lister, D.H. (2013). Updated high-resolution grids of monthly climatic observations - the CRU TS3.10 Dataset. *Int. J. Climatol.*, **34**, 623–642.

Held, I.M. and Soden, B.J. (2000). Water vapor feedback and global warming. *Annu. Rev. Energy Environ.*, **25**, 441–475.

Jiang, X., Chahine, M.T., Li, Q., Liang, M., Olsen, E.T., Chen, L.L., Wang, J. and Yung, Y.L. (2012). CO_2 semiannual oscillation in the middle troposphere and at the surface. *Global Biogeochem. Cycles*, **26**.

Jones, C.D., Collins, M., Cox, P.M. and Spall, S.A. (2001). The Carbon Cycle Response to ENSO: A Coupled Climate-Carbon Cycle Model Study. *J. Clim.*, **14**, 4113–4129.

Jouzel, J., Masson-Delmotte, V., Cattani, O., Dreyfus, S., Falourd, S., Hoffmann, G., Minster, B., Nouet, J., Barnola, J.M., Chappellaz, J., Fischer, H., Gallet, J.C., Johnsen, S., Leuenberger, M., Loulergue, L., Leuthi, D., Oerter, H., Parrenin, F., Raisbeck, G., Raynaud, D., Schilt, A., Schwander, J., Selmo, E., Souchez, R., Spahni, R., Stauffer, B., Steffensen, J.P., Stenni, B., Stocker, T.F., Tison, J.L., Werner, M. and Wolff, E.W. (2007). Orbital and millennial antarctic climate variability over the past 800,000 years. *Science*, **317**, 793–797.

Kaplan, J.O. (2002). Wetlands at the last glacial maximum: Distribution and methane emissions. *Geophys. Res. Lett.*, **29**.

Kawa, S.R., Mao, J., Abshire, J.B., Collatz, G.J., Sun, X. and Weaver, C.J. (2010). Simulation studies for a space-based CO_2 lidar mission. *Tellus*, **62B**, 759–769.

Keeling, C.D., Chin, J.F.S. and Whorf, T.P. (1996). Increased activity of northern vegetation inferred from atmospheric CO_2 measurements. *Nature*, **382**, 146–149.

Keeling, R.F. and Shertz, S.R. (1992). Seasonal and interannual variations in atmospheric oxygen and implications for the global carbon cycle. *Nature*, **358**, 723–727.

Kiehl, J.T. and Trenberth, K.E. (1997). Earth's annual global mean energy budget. *Bull. Am. Meteor. Soc.*, **78**, 197–208.

Kirschke, S. (2013). Three decades of global methane sources and sinks. *Nature Geoscience*, **6**, 813–823.

Knorr, W. (2009). Is the airborne fraction of anthropogenic CO_2 emissions increasing? *Geophys. Res. Lett.*, **36**.

Krol, M., Houweling, S., Bregman, B., van den Broek, M., Segers, A., van Velthoven, P., Peters, W., Dentener, F. and Bergamaschi, P. (2005). The two-way nested global chemistry-transport zoom model TM5: algorithm and applications. *Atmos. Chem. Phys.*, **5**, 417–432.

Le Quéré, C., Raupach, M.R., Canadell, J.G. and Marland, G. (2009). Trends in the sources and sinks of carbon dioxide. *Nat. Geosci.*, **2**, 831–836.

Le Quéré, C., Peters, G.P., Andres, R.J., Andrew, R.M., Bonden, T.A., Ciais, P., Friedlingstein, P., Houghton, R.A., Marland, G., Moriarty, R., Sitch, S., Tans, P., Arneth, A., Arvanitis, A., Bakker, D.C.E., Bopp, L., Canadel, J.G., Chini, L.P., Doney, S.C., Harper, A., Harris, L., House, J.I., Jain, A.K., Jones, S.D., Kato, E., Keeling, R.F., Klein Goldewijk, K., Körtzinger, A., Koven, C., Lefèvre, F., Maignan, Omar, A., Ono, T., Park, G.H., Pfeil, B., Poulter, B., Raupach, M.R., Regnier, P., Rödenbeck, C., Saito, S., Schwinger, J., Segschneider, J., Stocker, B.D., Takahashi, T., Tilbrook, B., van Heuven, S., Viovy, N., Wanninkhof, R., Wiltshire, A. and Zaehle, S. (2014). Global carbon project 2013. *Earth Syst. Sci. Data*, **6**, 235–263.

Lee, D., Vick, A.J.A. and Palmer, P.I. (2011). CEOI IFU Final Report. *report submitted to the Centre for Earth Observation Instrumentation.*

Lee, D., Barlow, J., Vick, A., Hastings, P., Atkinson, D., Black, M., Wilson, S. and Palmer, P. (2012). PERSIST - Prototype Earth observing System using Image Slicer Mirrors. *SPIE*, **8533**.

Levin, I. and Hesshaimer, V. (2000). Radiocarbon - a unique tracer of global carbon cycle dynamics. *Radiocarbon*, **42**, 69–80.

Linderholm, H.W. (2006). Growing season changes in the last century. *Agric. For. Meteorol.*, **137**, 1–14.

Loulergue, L., Schilt, A., Spahni, R., Masson-Delmotte, V., Blunier, T., Lemieux, B., Barnola, J.M., Raynaud, D., Stocker, T.F. and Chappellaz, J. (2008). Orbital and millennial-scale features of atmospheric CH_4 over the past 800,000 years. *Nature*, **453**, 383–386.

Lüthi, D., Floch, M.L., Bereiter, B., Blunier, T., Barnola, J.M., Siegenthaler, U., Raynaud, D., Jouzel, J., Fischer, H. and Kawamura, T.F., K. abd Stocker (2008). High-resolution carbon dioxide concentration record 650,000-800,000 years before present. *Nature*, **453**, 379–382.

MacFarling Meure, C., Etheridge, D., Trudinger, C., Steele, P., Langenfelds, R., van Ommen, T., Smith, A. and Elkins, J. (2006). Law Dome CO_2, CH_4 and N_2O ice core records extended to 2000 years BP. *Geophys. Res. Lett.*, **33**.

Masarie, K.A. and Tans, P.P. (1995). Extension and Integration of Atmospheric Carbon Dioxide Data into a Globally Consistent Measurement Record. *J. Geophys. Res.*, **100**, 11593–11610.

Masarie, K.A., Steele, L.P. and Lang, P.M. (1991). A rule-based expert system for evaluating the quality of long-term, in situ, gas chromatographic measurements of atmospheric methane. NOAA Tech. Memo. ERL CMDL-3, NOAA Environ. Res. Lab., Boulder, Colorado.

Mastepanov, M., Sigsgaard, C., Tagesson, T., Ström, L., Tamstorf, M.P., Lund, M. and Christensen, T.R. (2013). Revisiting factors controlling methane emissions from high-arctic tundra. *Biogeosciences*, **10**, 5139–5158.

Matthews, E. (1989). *Global Data Bases on Distribution, Characteristics and Methane Emission of Natural Wetlands: Documentation of Archived Data Tape*. NASA TM-4153, National Aeronautics and Space Administration.

McGuire, A.D., Anderson, L.G., Christensen, T.R., Dallimore, S., Guo, L., Hayes, D.J., Heimann, M., Lorenson, T.D., Macdonald, R.W. and Roulet, N. (2009). Sensitivity of the carbon cycle in the Arctic to climate change. *Ecol. Monogr.*, **79**, 523–555.

McGuire, A.D., Christensen, T.R., Hayes, D., Heroult, A., Euskirchen, E., Kimball, J.S., Koven, C., Lafleur, P., Miller, P.A., Oechel, W., Peylin, P., Williams, M. and Yi, Y. (2012). An assessment of the carbon balance of Arctic tundra: comparisons among observations, process models, and atmospheric inversions. *Biogeosciences*, **9**, 3185–3204.

Miller, S.M., Wofsy, S.C., Michalak, A.M., Kort, E.A., Andrews, A.E., Biraud, S.C., Dlugokencky, E.J., Eluskiewicz, J., Fischer, M.L., Janssens-Maenhout, G., Miller, B.R., Miller, J.B., Montzka, S.A., Nehrkorn, T. and Sweeney, C. (2013). Anthropogenic emissions of methane in the United States. *PNAS*, **110**.

Montzka, S.A., Krol, M., Dlugokencky, E., Hall, B., Jockel, P. and Lelieveld, J. (2011). Small Interannual Variability of Global Atmospheric Hydroxyl. *Science*, **331**, 67–69.

Myhre, G., Highwood, E.J., Shine, K.P. and Stordal, F. (1998). New estimates of radiative forcing due to well mixed greenhouse gases. *Geophysical Research Letters*, **25**, 2715–2718.

Natraj, V., Boesch, H., Spurr, R.J.D. and Yung, Y.L. (2008). Retrieval of XCO_2 from Simulated Orbiting Carbon Observatory Measurement using the Fast Linearized R-2OS Radiative Transfer Model. *J. Geophys. Res.*, **13**.

OECD (1996). Guideguide for aid agencies for improved conservation and sustainable use of tropical and sub-tropical wetlands. *Tech. rep, Organisation for Economic Co-operation and Development*.

Olsen, S.C. and Randerson, J.T. (2004). Differences between surface and column atmospheric CO_2 and implications for carbon cycle research. *J. Geophys. Res.*, **109**.

Overland, J.E., Wang, M. and Salo, S. (2008). The recent Arctic warm period. *Tellus*, **60A**, 589–597.

Pataki, D.E., Ehleringer, J.R., Flanagan, L.B., Yakir, D., Bowling, D.R., Still, C.J., Buchmann, N., Kaplan, J.O. and Berry, J.A. (2003). The application and interpretation of keeling plots in terrestrial carbon cycle research. *Global Biogeochem. Cycles*, **1**.

Piao, S., Ciais, P., Friedlingstein, P., Peylin, P., Reichstein, M., Luyssaert, S., Margolis, H., Fang, J., Barr, A., Chen, A., Grelle, A., Hollinger, D.Y., Laurila, T., Lindroth, A., Richardson, A.D. and Vesale, T. (2008). Net carbon dioxide losses of northern ecosystems in response to autumn warming. *Nature*, **451**, 49–52.

Ping, C.L., Michaelson, G.J., Jorgenson, M.T., Kimble, J.M., Epstein, H., Romanovsky, V.E. and Walker, D.A. (2008). High stocks of soil organic carbon in the North American Arctic region. *Nature Geoscience*, **1**, 615–619.

Quay, P.D., King, S.L., Stutsman, J., Wilbur, D.O., Steele, L.P., Fung, I., Gammon, R.H., Brown, T.A., Farwell, G.W., Grootes, P.M. and Schmidt, F.H. (1991). Carbon isotopic composition of atmospheric CH_4: Fossil and biomass burning source strengths. *Global Biogeochem. Cycles*, **11**, 535–560.

Randerson, J.T., Thompson, M.V., Conway, T.J., Fung, I.Y. and Field, C.B. (1997). The contribution of terrestrial sources and sinks to trends in the seasonal cycle of atmospheric carbon dioxide. *Global Biogeochem. Cycles*, **11**, 535–560.

Raupach, M.R. (2011). Pinning down the land carbon sink. *Nat. Clim. Change*, **1**, 148–149.

Raupach, M.R., Gloor, M., Sarmiento, J.L., Canadell, J.G., Frolicher, T.L., Gasser, T., Houghton, R.A., Le Quéré, C. and Trudinger, C.M. (2014). The declining uptake rate of atmospheric co_2 by land and ocean sinks. *Biogeosciences*, **11**, 3453–3475.

Raven, J.A. and Falkowski, P.G. (1999). Oceanic sinks for atmospheric CO_2. *Plant, Cell and Environment*, **22**, 741–755.

Rayner, P.J. and O'Brien, D.M. (2001). The utility of remotely sensed CO_2 concentration data in surface source inversions. *Geophys. Res. Lett.*, **28**, 175–178.

Rienecker, M.M., Suarez, M.J., Todling, R., Bacmeister, J., Liu, E., Bosilovich, M.G., Schubert, S.D., Takacs, L., Kim, G.K., Bloom, S., Chen, J., Collins, D., Conaty, A., da Silva, A. and et al. (2011). MERRA: NASA;s Modern-Era Retrospective Analysis for Research and Applications. *J. Climate.*, **24**, 2588–2606.

Rigby, M., Pring, R.G., Fraser, P.J., Simmonds, P.G., Langenfelds, R., Huang, J., Cunnold, D.M., Steele, L.P., Krummel, P.B., Weiss, R.F., O'Doherty, S., Salameh, P.K., Wang, H.J., Harth, C.M., Muhle, J. and Porter, L.W. (2008). Renewed growth of atmospheric methane. *Geophys. Res. Lett.*, **35**.

Romanovsky, V.E., Osterkamp, T.E., Sazonova, T.S., Shender, N.I. and Balovaev, V.T. (2001). Permafrost Temperature Dynamics Along the East Siberian Transect and an Alaskan Transect. *Tôhoku Geophys. Journ.*, **36**, 224–229.

Schwartz, M.D., Ahas, R. and Aasa, A. (2006). Onset of spring starting earlier across the northern hemisphere. *Global Change Biol.*, **12**, 343–351.

Screen, J.A. and Simmonds, I. (2010). The central role of diminishing sea ice in recent Arctic temperature amplification. *Nature*, **464**, 1334–1337.

Shakhova, N., Semiletov, I., Salyuk, A., Yusupov, V., Kosmach, D. and Gustavsson, O. (2010). Extensive Methane Venting to the Atmosphere from Sediments of the East Siberian Arctic Shelf. *Science*, **327**, 1246–1250.

Shakhova, N., Semiletov, I., Leifer, I., Sergienko, V., Salyuk, A., Kosmach, D., Chernykh, D., Stubbs, C., Nicolsky, D., Tumskoy, V. and Gustavsson, O. (2013). Ebullition and storm-induced methane release from the East Siberian Arctic Shelf. *Nat. Geosci.*, **7**, 64–70.

Shakun, J.D., Clark, P.U., Feng, H., Marcott, S.A., Mix, A.C., Liu, Z., Otto-Bliesner, B., Schmittner, A. and Bard, E. (2012). Global warming preceded by increasing carbon dioxide concentrations during the last deglaciation. *Nature*, **484**, 49–54.

Sirignano, C., Neubert, R.E.M., Rödenbeck, C. and Meijer, H.A.J. (2010). Atmospheric oxygen and carbon dioxide observations from two European coastal stations 2000-2005: continental influence, trend changes and APO climatology. *Atmos. Chem. Phys.*, **10**, 1599–1615.

Soden, B.J., Jackson, D.L., Ramaswamy, V., Schwarzkopf, M.D. and Huang, X. (2005). The radiative signiature of upper tropospheric moistening. *Science*, **310**, 841–844.

Song, C., Xu, X., Sun, X., Tian, H., Sun, L., Miao, Y., Wang, X. and Guo, Y. (2012). Large methane emissions upon spring thaw from natural wetlands in the northern permafrost region. *Environ. Res. Lett.*, **7**.

Stocker, T.F., Qin, D., Plattner, G.K., Tignor, M., Allen, S.K., Boschung, J., Nauels, A., Xia, Y., Bex, V. and Midgley, P.M. (2013). The physical science basis. contribution of working group i to the fifth assessment report of the intergovernmental panel on climate change (IPCC). *Cambridge University Press*.

Striskantharajah, S., Fisher, R.E., Lowry, D., Aalto, T., Hatakka, J., Aurela, M., Laurila, T., Lohila, A., Kuitunen, E. and Nisbet, E.G. (2012). Stable carbon isotope signatures of methane from a finnish subarctic wetland. *Tellus B*, **64**.

Sturtevant, C.S., Oechel, W.C., Zona, D., Kim, Y. and Emerson, C.E. (2012). Soil moisture control over autumn season methane flux, Arctic Coastal Plain of Alaska. *Biogeosciences*, **9**, 1423–1440.

Suntharalingam, P., Randerson, J.T., Krakauer, N., Logan, J.A. and Jacob, D.J. (2005). Influence of reduced carbon emissions and oxidation on the distribution of atmospheric CO_2: implications for inversion analysis. *Global Biogeochem. Cy.*, **19**.

Takahashi, T., Sutherland, S.C., Sweeney, C. and et al (2002). Global sea-air CO_2 flux based on climatological surface ocean pCO_2, and seasonal biological and temperature effects. *Deep Sea Res., Part II*, **49**, 1601–1622.

Tans, P.P., Conway, T.J. and Nakazawa, T. (1989). Latitudinal distribution of the sources and sinks of atmospheric carbon dioxide derived from surface observations and atmospheric transport model. *J. Geophys. Res.*, **94**, 5151–5172.

Tarnocai, C., Canadell, J.G., Schuur, E.A.G., Kuhry, P., Mazhitova, G. and Zimov, S. (2009). Soil organic carbon pools in the northern circumpolar permafrost region. *Global Biogeochem. Cycles*, **23**.

Taylor, G., Tallis, M.J., Giardina, C.P., Percy, K.E., Miglietta, F., Gupta, P.S., Gioli, B., Calfapietra, C., Gielen, B., Kubiske, M.E., Scarasciamugnozza, G.E., Kets, K., Long, S.P. and Karnosky, D.F. (2008). Future atmospheric CO_2 leads to delayed autumnal senescence. *Global Change Biol.*, **14**, 264–275.

Thompson, M.L., Enting, I.G., Pearman, G.I. and Hyson, P. (1986). Interannual variation of atmospheric CO_2 concentration. *J. Atmos. Chem.*, **4**, 125–155.

Thompson, R. (2011). The relationship of the phase and amplitude of the annual cycle of CO_2 to phenological events. *Plant Ecolog. Divers.*, **4**, 213–226.

Thompson, R. and Clark, R.M. (2008). Is spring starting earlier? *The Holocene*, **18**, 95–104.

Thoning, K.W. and Tans, P.P. (1989). Atmospheric Carbon Dioxide at Mauna Loa Observatory 2. Analysis of the NOAA GMCC Data, 1974-1985. *J. Geophys. Res.*, **94**, 8549–8565.

Torrence, C. and Compo, G.P. (1998). A practical guide to wavelet analysis. *Bull. Am. Meteorol. Soc.*, **79**, 61–78.

White, J.W.C. and Vaughn, B.H. (2011a). University of Colorado, Institute of Arctic and Alpine Research (INSTAAR), Stable Isotopic Composition of Atmospheric Carbon Dioxide (13C) from the NOAA ESRL Carbon Cycle Cooperative Global Air Sampling Network, 1990-2012, Version: 2013-04-05, Path: ftp://ftp.cmdl.noaa.gov/ccg/co2c13/flask/event/.

White, J.W.C. and Vaughn, B.H. (2011b). University of Colorado, Institute of Arctic and Alpine Research (INSTAAR), Stable Isotopic Composition of Atmospheric Methane (13C) from the NOAA ESRL Carbon Cycle Cooperative Global Air Sampling Network, 1998-2011, Version: 2013-04-05, Path: ftp://ftp.cmdl.noaa.gov/ccg/ch4c13/flask/event/.

Wolkovich, E.M., Cook, B.I., Allen, J.M., Crimmins, T.M., Betancourt, J.L., Travers, S.E., Pau, S., Regetz, J., Davies, T.J., Kraft, N.J.B., Ault, T.R., Bolmgren, K., Mazer, S.J., McCabe, G.J., McGill, B.J., Parmesan, C., Salamin, N., Schwartz, M.D. and Cleland, E.E. (2012). Warming experiments underpredict plant phenological responses to climate change. *Nature Letter*, **485**.

Zhao, C.L. and Tans, P.P. (2006). Estimating uncertainty of the WMO mole fraction scale for carbon dioxide in air. *J. Geophys. Res.*, **111**.

Zhuang, Q., Melillo, J.M., Sarofim, M.C., Kicklighter, D.W., McGuire, A.D., Felzer, B.S., Sokolov, A., Prinn, R.G., Steudler, P.A. and Hu, S. (2006). CO_2 and CH_4 exhanges between land ecosystems and the atmosphere in northern high latitudes over the 21st century. *Geophys. Res. Lett.*, **33**.

Zhuang, Q., Melillo, J.M., McGuire, A.D., Kicklighter, D.W., Prinn, R.G., Steudler, P.A., Felzer, B.S. and Hu, S. (2007). Net emissions of CH_4 and CO_2 in Alaska: Implications for the region's greenhouse gas budget. *Ecol. Appl.*, **17**, 203–212.

Zimov, S.A., Davydov, S.P., Zimov, G.M., Davydova, A.I., Schuur, E.A.G., Dutta, K. and Chapin III, F.S. (2006a). Permafrost carbon: Stock and decomposability of a glglobal significant carbon pool. *Geophys. Res. Lett.*, **33**.

Zimov, S.A., Schuur, E.A.G. and Chapin III, F.S. (2006b). Permafrost and the Global Carbon Budget. *Science*, **312**, 1612–1613.